NUCLEAR QUADRUPOLE INTERACTIONS OF ^{19}F IN GRAPHITE, SILICON, GERMANIUM AND GALLIUM ARSENIDE

by

DJOKO SURONO

B. Sc. Universitas Indonesia, Jakarta (1986)

M. Sc. The University of British Columbia (1991)

A THESIS SUBMITTED IN PARTIAL FULFILLMENT OF THE

REQUIREMENTS FOR THE DEGREE OF

DOCTOR OF PHILOSOPHY

in

THE FACULTY OF GRADUATE STUDIES

(Department of Physics)

We accept this thesis as conforming

to the required standard

The University of British Columbia, Vancouver, Cananda.

In presenting this thesis in partial fulfillment of the requirements for an advanced degree at the University of British Columbia, I agree that the Library shall make it freely available for reference and study. I further agree that permission for extensive copying of this thesis for scholarly purposes may be granted by the head of my department or by his or her representatives. It is understood that copying or publication of this thesis for financial gain shall not be allowed without my written permission.

(Signature)

Department of PHYSICS

The University of British Columbia
Vancouver, Canada

Date April 13, 1995

ABSTRACT

Measurements of nuclear quadrupole interactions of $^{19}F^*$ in graphite, silicon, germanium and gallium arsenide have been carried out; the electric field gradients (efgs) at F impurity sites have been compared with cluster model calculations using both Hartree-Fock (HF) and Density Functional Theory (DFT) formalisms. The technique of time-differential perturbed angular distributions of γ-rays (TDPAD) was employed using the $^{19}F(p,p')^{19}F^*$ reaction to derive the efg parameters following the implantation into the hosts of $^{19}F^*$ in its isomeric state at 197 keV ($I^\pi=5/2^+$, $T_{1/2}=85$ ns).

For the case of highly oriented pyrolytic graphite (HOPG) the principal components of the electric field gradient and its asymmetry parameter were found to be $|V_{zz}|=3.24(14)\times10^{22}$ V/m^2 and $\eta=0.16(3)$, respectively, in close agreement with the DFT predictions of $V_{zz}=-3.09\times10^{22}$ V/m^2 and $\eta=0.13$ obtained for ^{19}F at a site midway between the layers with point group symmetry C_{2h} and inter-layer spacing $d=3.70$ Å. As a test of shell model theories an attempt was made to detect the nuclear quadrupole moment Q of the first excited state of $^{22}Na^*$ (E=583 keV, $I^\pi=1^+$, $T_{1/2}=243$ ns). In this case the $^{19}F(\alpha,n)^{22}Na^*$ reaction was used to implant $^{22}Na^*$ nuclei into HOPG. However, no quadrupole interaction was detected, leading to the conclusion that $|QV_{zz}| < 8.7(8)\times10^{20}$ bV/m^2. Taking $Q=0.06$ barns as the best theoretical estimate for the 583 keV state, we find that $|V_{zz}|$ must be less than $8.7(8)\times10^{20}$ V/m^2.

In the ^{19}F implantation in silicon three sites were found corresponding to quadrupole frequencies 23.2(3) MHz, 35.2(3) MHz and 37.1(5) MHz. Both HF and DFT calculations are consistent with the assignment of interstitial antibonding and bond-centre sites for the first two interactions, with HF predictions of 23.4 MHz and 35.0 MHz, respectively. In the former case the F atom is located 1.81 Å along a $\langle111\rangle$ direction from a silicon atom; in the latter situation the Si–Si bond length is found to expand by 1.02 Å from

its normal lattice value. It is speculated that the third interaction, which occurs at only the 10% level, possibly arises from sites associated with a defect or other impurity.

In germanium two quadrupole frequencies were detected, with ν_{Q1}=27.5(3) MHz and ν_{Q2}=33.0(4) MHz, while in gallium arsenide only a single interaction was observed, with ν_Q=27.7(3) MHz. In all cases the asymmetry parameter η was close to or equal to zero. In the case of germanium ν_{Q1} and ν_{Q2} are tentatively ascribed to antibonding and bond-centre sites, respectively. In the antibonding configuration the fluorine is situated at 1.88 Å along a $\langle 111 \rangle$ direction from a germanium atom. For F at the bond-centre site the Ge–Ge bond length was found to increase by about 1 Å from its normal lattice value. In gallium arsenide the single frequency ν_Q is consistent with DFT calculations yielding ν_Q=28.0 MHz for F at an intrabond site with the fluorine situated at 1.37 Å from the Ga and 2.40 Å from the As atom. In most cases the DFT predictions are in better agreement with experiment than those of HF.

To achieve a reduction in cluster size, the completion of dangling bonds with atoms other than hydrogen was investigated for different silicon clusters. The results were found to be comparable with those obtained for larger clusters terminated by H atoms.

Table of Contents

List of Figures

List of Tables

Table of abbreviations and symbols.

$A_{k_1 k_2}$	:	nuclear parameters in the perturbed angular distribution function
AB	:	antibonding
A–B–A	:	a layered structure
BC	:	bond-centre
DFT	:	Density Functional Theory
efg	:	electric field gradient
FWHM	:	Full Width at Half Maximum
$G_{k_1 k_2}^{N_1 N_2}(t)$	:	the perturbation factors in the perturbed angular distribution function
HF	:	Hartree-Fock
HOPG	:	Highly Oriented Pyrolytic Graphite
I	:	neclear level spin
IRMM	:	Institute for Reference Materials and Measurements, Geel, Belgium.
i_1, i_2, b_1 and b_2	:	cluster sites used in HOPG calculations.
NMR	:	Nuclear Magnetic Resonance
NQI	:	Nuclear Quadrupole Interaction
Q	:	the quadrupole moment of a nucleus
RHF	:	Restricted Hartree-Fock
ROHF	:	Restricted Open Shell Hartree-Fock
SCF	:	Self Consistent Field
STO	:	Slater Type Orbitals
STO–nG	:	minimal basis sets

TDPAC	:	Time Differential Perturbed Angular Correlations
TDPAD	:	Time Differential Perturbed Angular Distributions
UHF	:	Unrestricted Hartree-Fock
$\|V_{zz}\|$	:	the largest component of the electric field gradient
VC	:	Vitreous Carbon
$W(\Theta, t)$	:	the perturbed angular distribution function
α, β, θ, Θ and ϕ	:	symbols to indicate angles
δ	:	the width of an efg interaction
η	:	the asymmetry parameter of an electric field gradient
ν_Q	:	quadrupole frequency
ν_{Qi}	:	the quadrupole frequency of the i^{th} interaction
ω	:	angular frequency
σ	:	the gaussian width of the time resolution of the detectors
Ψ	:	n-electron wave function
ψ	:	one-electron orbital wave function
χ	:	one-electron spin-orbital wave function

Acknowledgements.

I would like to thank my supervisor, Professor Peter W. Martin, for his advice, guidance and discussion regarding this thesis and during my study at the department of physics, UBC. I am extremely grateful to the Van de Graaff group at the Institute for Reference Materials and Measurements, Geel, Belgium, especially Drs. Crametz, Hambsch and the accelerator operators P. Falque, J. Leonard and W. Schubert for their support during the experiments. I express my thanks to P. Rietveld for performing the sample evaporations, to Dr. J. W. Bichard and Professor D. P. Chong regarding the cluster model calculations, and to computer staff in both physics and chemistry departments.

I am also indebted to many friends and families who encouraged me in my rough times and laughed with me in my happier days.

Finally, I should like to thank the Government of Indonesia (BATAN and BPPT) for a scholarship and express my gratitude to the World University Service of Canada for their helpful assistance.

Chapter 1

General introduction.

1.1 Prologue.

This thesis describes work performed in the field of hyperfine interactions, specifically an application of the Time Differential Perturbed Angular Distribution (TDPAD) method in the field of materials science. The experiments were carried out during 1991–92 at the Institute for Reference Materials and Measurements (IRMM), previously known as the Central Bureau for Nuclear Measurements, Geel, Belgium. All of the analysis of the data was completed in the department of Physics, UBC, over the period 1992–93. The second part of the work, theoretical calculations of electric field gradients, was performed during the course of 1994 using computer facilities at both the physics and chemistry departments of the University of British Columbia.

1.2 Perturbed angular distributions: a novel tool for condensed matter.

For many years the technique known as time-dependent perturbed angular correlations of γ-rays (TDPAC) has played a valuable role in the investigation of hyperfine interactions between probe nuclei and their electromagnetic environment in a host material [1,2]. In this method γ–γ coincidences are required, both for the preparation (via the detection of γ_1) of the nuclear state under study and for the observation of its decay (by detection of γ_2) . The technique is limited by the number (~ 20) and availability of suitable radioisotopes, as well as by their cost of preparation.

nuclear state and V_{zz} is the principal component of the efg. The symmetry properties of the efg are expressed through the asymmetry parameter $\eta=(V_{xx}-V_{yy})/V_{zz}$.

Since the efg is highly sensitive to the local electronic structure in the host material, the nature of the site occupied by the probe can then in principle be inferred from theoretical calculations of V_{zz} and η. Until relatively recently, such calculations were regarded as unreliable owing to the complexity imposed by a quantum mechanical system of many electrons. In recent years, however, the enormous expansion of computing power, together with the development of superior calculational techniques for handling atomic basis set representations, have made it possible to take into account the hybridization of all electronic orbitals, even in fairly large systems. How successful these developments have been can be judged from the results of experiments described in Chapters 4, 5 and 6 of this thesis and their comparison to the predictions of Hartree-Fock and Density Functional Theory calculations.

1.3 Rationale and objectives.

While angular correlation and distribution methods have been in use for more than 50 years, their application to materials science lies far behind other analytical methods such as Nuclear Magnetic Resonance (NMR) or Mössbauer spectroscopy. For many years angular correlation experiments were confined exclusively to the domain of the nuclear physicist, remaining virtually unknown to researchers in other areas. One of the reasons for the unpopularity of the method was probably the requirement of radioactive material (TDPAC), or for an accelerator to produce particle beams (TDPAD). However, in recent years applications of TDPAC/TDPAD have been extended to broad areas of research in such diverse fields as materials science, chemistry, condensed matter, biochemistry and biophysics [5].

In this thesis we exploit the on-line accelerator technique of time-differential perturbed angular distributions of γ-rays (TDPAD), in which a nuclear reaction is used to implant isomeric probe nuclei into the host material. Since the isomeric state can be produced with some degree of alignment, the emitted γ-radiation has in general an anisotropic distribution [3,4]. As a knowledge of the angular distribution can lead to information on the level spins, lifetimes and multipolarities of transitions in the decaying nucleus, such measurements have played a major role for many years in elucidating nuclear decay scheme parameters. Ironically, what was a major disadvantage for the nuclear physicist, namely the interaction of the nucleus with its environment, has now become a significant tool in the armamentarium of the solid state physicist.

If the intermediate nuclear state has a finite lifetime τ_N, it can couple during this time to its environment via the interaction of its magnetic or electric moments with the local magnetic field or electric field gradient. For example, the magnetic dipole interaction can be considered classically as the Larmor precession with frequency ν_L of the magnetic moment about the direction of the local **B** field. If $\tau_N \gg 1/\nu_L$, the angular distribution of the subsequent γ-emission will be appreciably perturbed, and if the resolving time of the measuring apparatus is significantly less than $1/\nu_L$, time-differential measurements can then follow the precession of the nuclear spins.

In the work described here (on non-magnetic materials) we are interested primarily in static electric quadrupole interactions. In this case one can view the interaction classically as the bi-directional precession of the nuclear quadrupole moment about the axis of the local electric field gradient (efg), resulting again in a perturbation of the γ-ray angular distribution. As will be shown in Chapters 2 and 3, TDPAD measurements can yield information on the parameters describing the quadrupole interaction, in particular its strength and symmetry properties. The former is usually expressed in terms of the quadrupole frequency $\nu_Q = eQV_{zz}/h$, where Q is the (known) quadrupole moment of the

The objectives of the work described in this thesis are twofold:

(i) To further the application of TDPAD in the field of materials science.

(ii) To test the efficacy of current theoretical formalisms for calculations of the efg in matter.

The two aspects are, of course, intimately coupled. The usefulness of TDPAD as a diagnostic technique for materials would be heavily circumscribed without a firm theoretical framework as a basis for connecting the measurements to the electronic structure of the material under study.

Specifically, in (i) our goal was to establish the nature of the residence sites of fluorine in semiconductors. For several years it has been known in the semiconductor industry that the addition of small amounts of fluorine during device fabrication can significantly improve performance characteristics [see section 5.1]. Nevertheless, details of the specific role played by fluorine are still lacking. A *sine qua non* for such an understanding is the determination of the residence sites. We therefore embarked on a series of investigations of nuclear quadrupole interactions of ^{19}F in silicon, germanium and gallium arsenide.

In the second of our main objectives, our interest focused on the predictions of Hartree-Fock (HF) and Density Functional Theory (DFT) formalisms for the calculation of electric field gradients. Since the ground state spin of ^{19}F is I=1/2, it is not amenable to investigation by nuclear quadrupole resonance. Hence TDPAD offers a novel way to investigate quadrupole interactions in this case using the isomeric level ($I=5/2^+$) at 197 keV excitation. The need to compare the predictions of HF and DFT calculations has been stressed many times in the literature [6,7]. Since the relative success of the theoretical models may depend to some extent upon which property is being measured [8], the extension to quadrupole interactions gains further importance.

As a first test, both of the experimental technique and theoretical formalisms, we investigated the nuclear quadrupole interactions of ^{19}F in highly oriented pyrolytic graphite. The Gaussian 92 (G–92) system of programs was used to perform the HF and DFT calculations [Chapter 4]. These results gave us confidence to press ahead with the investigations in semiconductors.

The extent to which these objectives have been attained is readily assessed by referring to the summary of results outlined in Chapter 7 of this thesis.

1.4 Outline.

This thesis consists of 7 chapters. Following this introduction the theoretical foundation of TDPAD is presented briefly in Chapter 2. Since we are mainly concerned with nuclear quadrupole interactions (NQI) in various materials, first we introduce a discussion of this interaction and its relation to TDPAD. We focus on the NQI of nuclei with spin angular momentum I=5/2 in an electric field gradient (efg) V_{ij}. A summary of angular correlation theory is given to describe the necessary equations used in later analysis. The last part of Chapter 2 contains a discussion of the HF and DFT formalisms used for the efg calculations.

General information on the experimental apparatus is provided in Chapter 3. Since in TDPAD alignment of the probe nuclei is crucial, we review briefly some methods to achieve nuclear alignment by other techniques before describing the apparatus and experiments. The main component of the TDPAD experiment, the 7MV Van de Graaff accelerator used to produce the particle beam, is described in section 3.2. A description of the detectors and system of electronics used in this work appears in section 3.3. In this chapter we also discuss the possible implantation damage in the samples due to the primary proton beam and the implanted nuclei.

The core of this thesis is presented in the next three chapters. In Chapter 4 we report the TDPAD measurements for ^{19}F implantation in graphite. In this experiment we basically test our system using a pseudo-single crystal material (Highly Oriented Pyrolytic Graphite) before performing the measurements on semiconductor materials. As a test of nuclear shell model theories we also performed measurements on the quadrupole moment of the first excited state of ^{22}Na by implanting ^{22}Na* nuclei into HOPG as the host. The measurements of NQI in semiconductor materials (Si, Ge and GaAs) are reported in Chapters 5 and 6. For each experimental situation we also perform theoretical

calculations of the efgs and the asymmetry parameters (η) in various possible sites in the crystalline matrices of the samples.

General conclusions are presented in Chapter 7.

The results contained in this thesis have been published, or await publication, in the journals Hyperfine Interactions [9,10] and The Journal of Chemical Physics [11].

Chapter 2

Theoretical.

2.1 Introduction.

In this chapter we give a review of the theory of perturbed angular correlations (PAC) and a description of the electric field gradient (efg) calculations involved in the Hartree-Fock (HF) and Density Functional Theory (DFT) formalisms. In the former case, PAC theory underlies the analysis of the experimental data, where theoretical fits are used to generate the parameters describing the quadrupole interactions. The HF and DFT procedures provide a framework which allows comparison of the measured efgs with theoretical predictions for the probe at specific sites in the host lattice.

Before going on to describe the theory of perturbed angular distributions we review the subject of electric quadrupole interactions.

2.2 Nuclear quadrupole interactions (NQI).

The electrostatic interaction of a nucleus with charge density $\rho_N(\vec{r})$ in a potential $V(\vec{r})$ can be expressed by the Hamiltonian:

$$H = \int \rho_N(\vec{r}) V(\vec{r}) d^3r. \tag{2.1}$$

The potential $V(\vec{r})$ can be written as a Taylor expansion around the nuclear centre,

$$V(\vec{r}) = V_0 + \sum_i x_i \left(\frac{\partial V(\vec{r})}{\partial x_i}\right) + \frac{1}{6}\sum_{ij}(3x_i x_j - r^2\delta_{ij})\left(\frac{\partial^2 V(\vec{r})}{\partial x_i \partial x_j}\right) + \cdots. \tag{2.2}$$

By substituting eqn. (2.2) into (2.1) one can write the Hamiltonian as

$$\begin{aligned} H &= ZeV_0 + \sum_i \int \rho_N(\vec{r}) x_i d^3r \times \left(\frac{\partial V(\vec{r})}{\partial x_i}\right) + \\ &\quad \frac{1}{6}\sum_{ij} \int \rho_N(\vec{r})(3x_i x_j - r^2\delta_{ij}) d^3r \times \left(\frac{\partial^2 V(\vec{r})}{\partial x_i \partial x_j}\right) + \cdots, \end{aligned} \tag{2.3}$$

where $Ze=\int \rho_N(\vec{r})d^3r$ is the nuclear charge. The integrands in the second and third terms are known as the components of the nuclear electric dipole moment p_j and the elements of the nuclear quadrupole tensor Q_{ij}, respectively. The first term of eqn. (2.3) can be eliminated because it does not produce any splitting of the magnetic substates and is not observable in an angular distribution measurement; the second term vanishes because the electric dipole moment is necessarily zero for any quantum mechanical system in a stationary state [12]. Neglecting the higher order terms which are very small, the Hamiltonian of eqn. (2.3) thus contains only the interaction of interest, the nuclear electric quadrupole interaction.

Since the electric field gradient tensor, $V_{ij}=\partial^2 V/\partial x_i \partial x_j$, is symmetric it can always be transformed into a principal axis system in which $V_{ij}=V_{ii}\delta_{ij}$. Furthermore, since the potential $V(\vec{r})$ originates from a charge distribution outside the nucleus, it follows that Laplace's equation holds, $\nabla^2 V(\vec{r})=V_{xx}+V_{yy}+V_{zz}=0$. In the principal axis system the efg can be completely described by two quantities: the largest component, V_{zz}, and the asymmetry parameter

$$\eta = \frac{(V_{xx} - V_{yy})}{V_{zz}}. \tag{2.4}$$

Since by definition $|V_{zz}| \geq |V_{yy}| \geq |V_{xx}|$, the asymmetry parameter is in the range $0 \geq \eta \geq 1$.

The quadrupole moment of a nucleus in the state $|\Psi\rangle$ is defined by [12]

$$Q = \sum_{i=1}^{Z} \int e(3z_i^2 - r_i^2)|\Psi(\vec{r}_1, \cdots, \vec{r}_A)|^2 d\tau \tag{2.5}$$

where the sum goes over all the protons.

By using the Wigner-Eckart theorem the Hamiltonian of eqn. (2.3) in the principal axis system can be written in terms of spin operators I_z, I_+=(I_x+iI_y) and I_-=(I_x-iI_y):

$$H = \frac{3eQV_{zz}}{4I(2I-1)}\left\{I_z^2 - \frac{1}{3}I(I+1) + \frac{1}{6}\eta(I_+^2 + I_-^2)\right\} \tag{2.6}$$

In terms of the magnetic quantum numbers m, this Hamiltonian has the following matrix elements [13]:

$$\begin{aligned} H_{m,m} &= \hbar\omega_E[3m^2 - I(I+1)] \\ H_{m,m\pm2} &= \frac{1}{2}\hbar\omega_E\,\eta\,[(I\mp m)(I\mp m-1)(I\pm m+1)(I\pm m+2)]^{1/2} \end{aligned} \tag{2.7}$$

where $\hbar\omega_E$=$eQV_{zz}/4I(2I-1)$.

The Hamiltonian of eqn. (2.6) has two important symmetry properties:

$$H_{m,m'} = H_{-m,-m'} \tag{2.8}$$

and

$$H_{m,m'} = H_{m',m}. \tag{2.9}$$

To see how the eqn. (2.8) follows we note that the diagonal terms contain m^2 only and hence are unaffected when m is replaced by $-m$.

For the off-diagonal elements eqn. (2.8) yields $H_{m,m\pm2}$=$H_{-m,-m\mp2}$. This can be seen to follow by noting that the substitution of m by $-m$ and $\pm$ by $\mp$ in eqn. (2.7) has no effect, since the $\pm$ sign appears throughout only in front of m.

The symmetry given by eqn. (2.9) affects only the off-diagonal terms. Substitution in eqn. (2.7) of m by $-(m\pm2)$ shows that the terms in square brackets are invariant, thus $H_{m,m\pm2}$=$H_{-m\mp2,-m}$. Applying symmetry relation (2.8) then gives the desired result, $H_{m,m\pm2} = H_{m\pm2,m}$.

For the measurements involved in this work the spin of the isomeric state is I=5/2. In this case the explicit form of the Hamiltonian is, in units of $\hbar\omega_E$:

$$H = \begin{pmatrix} 10 & 0 & \eta\sqrt{10} & 0 & 0 & 0 \\ 0 & -2 & 0 & \eta\sqrt{18} & 0 & 0 \\ \eta\sqrt{10} & 0 & -8 & 0 & \eta\sqrt{18} & 0 \\ 0 & \eta\sqrt{18} & 0 & -8 & 0 & \eta\sqrt{10} \\ 0 & 0 & \eta\sqrt{18} & 0 & -2 & 0 \\ 0 & 0 & 0 & \eta\sqrt{10} & 0 & 10 \end{pmatrix} \tag{2.10}$$

The diagonalization of this matrix gives the following Cardano-type equation for the eigenvalues E,

$$E^3 - aE - b = 0 \tag{2.11}$$

with a=28(η^2+3) and b=160(1-η^2). The solutions (degenerate with respect to $\pm m$) are:

$$\begin{aligned} E_1 &= A\cos(\phi/3), \\ E_2 &= A\cos(\phi/3 + 2\pi/3), \\ E_3 &= A\cos(\phi/3 + 4\pi/3), \end{aligned} \tag{2.12}$$

where A=$2\sqrt{a/3}$ and $\cos\phi$=(b/2)/$\sqrt{a^3/27}$. The three quadrupole frequencies $\omega_{nn'}$=$(E_n - E_{n'})/\hbar$, shown in the accompanying fig. (2.1), are :

$$\begin{aligned} \omega_1 &= (E_2 - E_3)\omega_E, \\ \omega_2 &= (E_1 - E_2)\omega_E, \\ \omega_3 &= (E_1 - E_3)\omega_E. \end{aligned} \tag{2.13}$$

These frequencies, comprising a triplet for each single electric quadrupole interaction, are the observables in our TDPAD measurements. Damping effects (see eqn. 2.25)

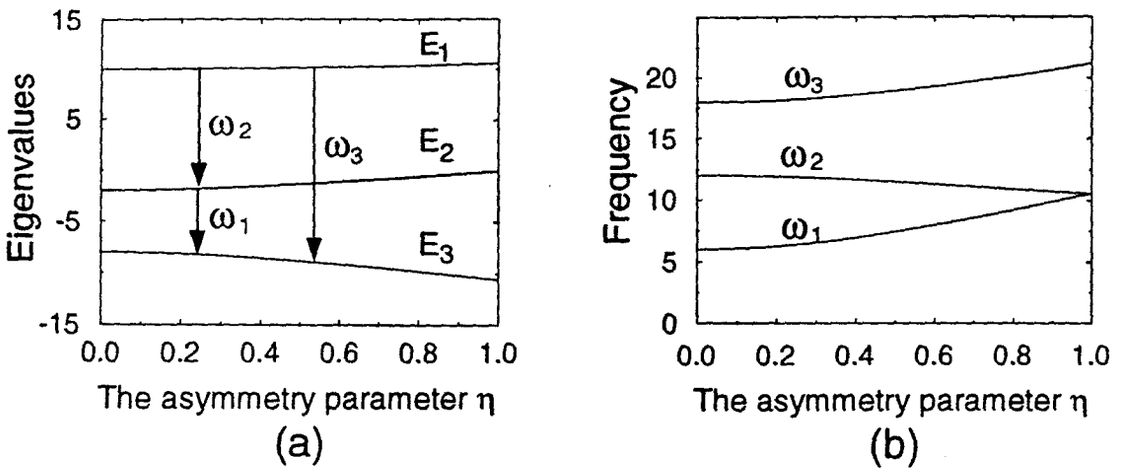

Figure 2.1: (a) Schematic diagram of the eigenvalues E_n and (b) frequencies ω_n vs. the asymmetry parameter η for an electric quadrupole interaction of a nucleus with spin I=5/2.

usually cause severe attenuation of ω_3 in the Fourier power transform. Nevertheless, the ratio ω_2/ω_1 is sufficient to determine η from the relationship

$$\frac{\omega_2}{\omega_1} = \frac{1}{2}\left\{\sqrt{3}\cot(\phi/3) - 1\right\}, \tag{2.14}$$

where $1 \leq \omega_2/\omega_1 \leq 2$ for $1 \geq \eta \geq 0$.

2.3 TDPAC/TDPAD

There is no significant difference in the theoretical treatment of Time-Differential Perturbed Angular Correlations (TDPAC) and Distributions (TDPAD); the only difference is the way in which one selects the isomeric state. In TDPAC one selects the aligned sub-ensemble by detecting the first γ-ray in a particular but arbitrary direction $\vec{k}_1$, then measures the directional correlation of γ_2 with respect to $\vec{k}_1$. The angular distribution method uses nuclear bombardment to produce an aligned ensemble of excited nuclei in

the isomeric state. The emitted γ-radiation is then measured relative to the beam direction as the quantization axis. The theory of TDPAC works for TDPAD if one considers the direction of the beam as equivalent to $\vec{k}_1$ in the TDPAC case, i.e. the γ-ray angular distribution in TDPAD can be expressed in terms of the correlation function for a hypothetical γ-γ cascade in which the first transition is a pure 2^l-pole [14,15].

2.3.1 Two successive dipole transitions.

The principle by which alignment is obtained in the isomeric state can be demonstrated by the following example. Consider two successive dipole transitions in a $0 \xrightarrow{\gamma 1} 1 \xrightarrow{\gamma 2} 0$ cascade (fig. 2.2). From electrodynamics the multipole transition probabilities $W_L^{\Delta m}(\Theta)$ are

$$W_1^{\pm 1}(\Theta) = \frac{3}{2}(1 + \cos^2\Theta); \quad W_1^0(\Theta) = 3\sin^2\Theta$$

where the magnetic quantum number selection rules are $\Delta m = 0, \pm 1$. In a randomly oriented ensemble, the populations p_m of the substates are equal, so that the angular distribution, say for the single transition γ_2, is as expected, isotropic:

$$\begin{aligned} W(\Theta) &= \sum p_m W_L^{\Delta m}(\Theta) \\ &= \frac{1}{3}W_1^{+1}(\Theta) + \frac{1}{3}W_1^0(\Theta) + \frac{1}{3}W_1^{-1}(\Theta) = \text{constant.} \end{aligned}$$

If now γ_2 is detected *in coincidence* with γ_1, the transverse nature of EM radiation gives zero probability for detection of Δm=0 transitions along the (γ_1) quantization axis (i.e. Θ=0), allowing only transitions with Δm=$\pm$1 followed by Δm=$\mp$1. Thus the angular correlation of γ_2 with respect to γ_1 is now non-isotropic, with

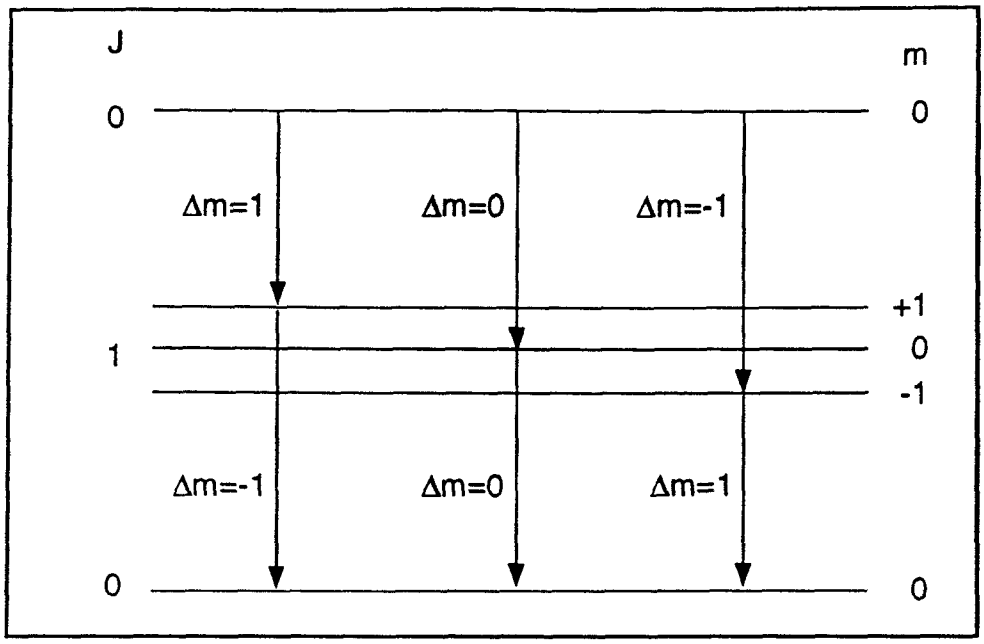

Figure 2.2: Two successive dipole transitions.

$$\begin{aligned} W(\Theta) &= \frac{1}{2}W_1^{+1}(\Theta) + \frac{1}{2}W_1^{-1}(\Theta) \\ &= \frac{3}{2}(1+\cos^2\Theta) \\ &= 2(1+\frac{1}{2}P_2) \end{aligned}$$

where $P_2=\frac{1}{2}(3\cos^2\Theta - 1)$ is the Legendre polynomial.

Thus in the TDPAC coincidence measurement the detection of γ_1 acts as a quantum state selector to produce alignment in the intermediate state. Similarly, the detection of the particle beam in TDPAD selects certain m-states preferentially in the nuclear reaction.

2.3.2 The perturbed angular distribution function.

A comprehensive review of the theory of perturbed angular correlations is presented in the classic article of Frauenfelder and Steffen [16]. Here we give a brief summary of the theory for non-axially symmetric interactions, with particular reference to the case of spin I=5/2. For an incident particle beam along $\vec{k}_1$, the perturbed angular distribution function for the γ-ray emitted in direction $\vec{k}_2$ is

$$\begin{aligned} W(\vec{k}_1,\vec{k}_2;t) &= \sum_{k_1 k_2} A_{k_1}(1)A_{k_2}(2)\{(2k_1+1)(2k_2+1)\}^{-1/2} \times \\ &\quad \sum_{N_1 N_2} G^{N_1 N_2}_{k_1 k_2}(t) Y^{N_1 *}_{k_1}(\theta_1,\phi_1) Y^{N_2}_{k_2}(\theta_2,\phi_2). \end{aligned} \tag{2.15}$$

where $A_{k_1}(1)$ and $A_{k_2}(2)$ are amplitude parameters determined by the nuclear reaction and subsequent γ-decay, respectively. The perturbation factor in eqn. (2.15) is defined as [16]

$$\begin{aligned} G^{N_1 N_2}_{k_1 k_2}(t) &= \sum_{m_a m_b} (-1)^{2I+m_a+m_b}\{(2k_1+1)(2k_2+1)\}^{1/2} \\ &\quad \times \begin{pmatrix} I & I & k_1 \\ m'_a & -m_a & N_1 \end{pmatrix} \begin{pmatrix} I & I & k_2 \\ m'_b & -m_b & N_2 \end{pmatrix} \\ &\quad \times \langle m_b|\Lambda(t)|m_a\rangle \langle m'_b|\Lambda(t)|m'_a\rangle , \end{aligned} \tag{2.16}$$

where $\Lambda(t)=\exp(-iHt/\hbar)$ is a unitary operator describing the time evolution of substates $|m_a\rangle$ into different states $|m_b\rangle$ as a result of the extranuclear perturbation by the Hamiltonian H. These intraband transitions correspond to the classical Larmor precession frequencies mentioned in Chapter 1. Since the initial alignment of the excited state is not exactly known, the product $A_{k_1}(1)A_{k_2}(2) \equiv A_{k_1 k_2}$ is sometimes treated as a free parameter.

In terms of the intraband frequencies the perturbation function can be expressed as

$$G^{N_1 N_2}_{k_1 k_2}(t) = \sum_{m_a m_b} (-1)^{2I+m_a+m_b}\{(2k_1+1)(2k_2+1)\}^{1/2}$$

$$\times \begin{pmatrix} I & I & k_1 \\ m'_a & -m_a & N_1 \end{pmatrix} \begin{pmatrix} I & I & k_2 \\ m'_b & -m_b & N_2 \end{pmatrix}$$
$$\times \langle n|m_b\rangle^* \langle n|m_a\rangle \langle n'|m'_b\rangle \langle n'|m'_a\rangle^* \cos(\omega_{nn'}t). \tag{2.17}$$

As mentioned earlier in section 2.2, the degeneracy with respect to $\pm m$ in the case of electric quadrupole interactions gives rise to three intraband frequencies for spin I=5/2, and we can write

$$G^{N_1N_2}_{k_1k_2}(t) = \sum_{p=0}^{3} S^{N_1N_2}_{k_1k_2p} \cos(g_p\omega_0 t) \tag{2.18}$$

where

$$\begin{aligned} S^{N_1N_2}_{k_1k_2}(t) &= \sum_{m_am_b} (-1)^{2I+m_a+m_b}\{(2k_1+1)(2k_2+1)\}^{1/2} \\ &\times \begin{pmatrix} I & I & k_1 \\ m'_a & -m_a & N_1 \end{pmatrix} \begin{pmatrix} I & I & k_2 \\ m'_b & -m_b & N_2 \end{pmatrix} \\ &\times \langle n|m_b\rangle^* \langle n|m_a\rangle \langle n'|m'_b\rangle \langle n'|m'_a\rangle^* \end{aligned} \tag{2.19}$$

and g_p is defined implicitly by

$$\omega_{nn'} = (E_n - E_{n'})/\hbar = g_p\omega_0 \tag{2.20}$$

with ω_0=$6\omega_E$ and g_0=0. The frequency ω_0 is a convenient parameter as it corresponds to the smallest non-vanishing energy difference in the quadrupole splitting for η=0.

The quadrupole frequency, or coupling constant, is defined as

$$\nu_Q = eQV_{zz}/h = \frac{20}{\pi}\omega_E = \frac{10}{3\pi}\omega_0. \tag{2.21}$$

For the case of axial symmetry (η=0), the g_p take on integral values, giving intraband frequencies of ω_0, $2\omega_0$ and $3\omega_0$. Otherwise, g_p is a function of η.

The above equations can be simplified by imposing restrictions based on angular momentum conservation and the physical conditions of the sample. In the 3-j symbols

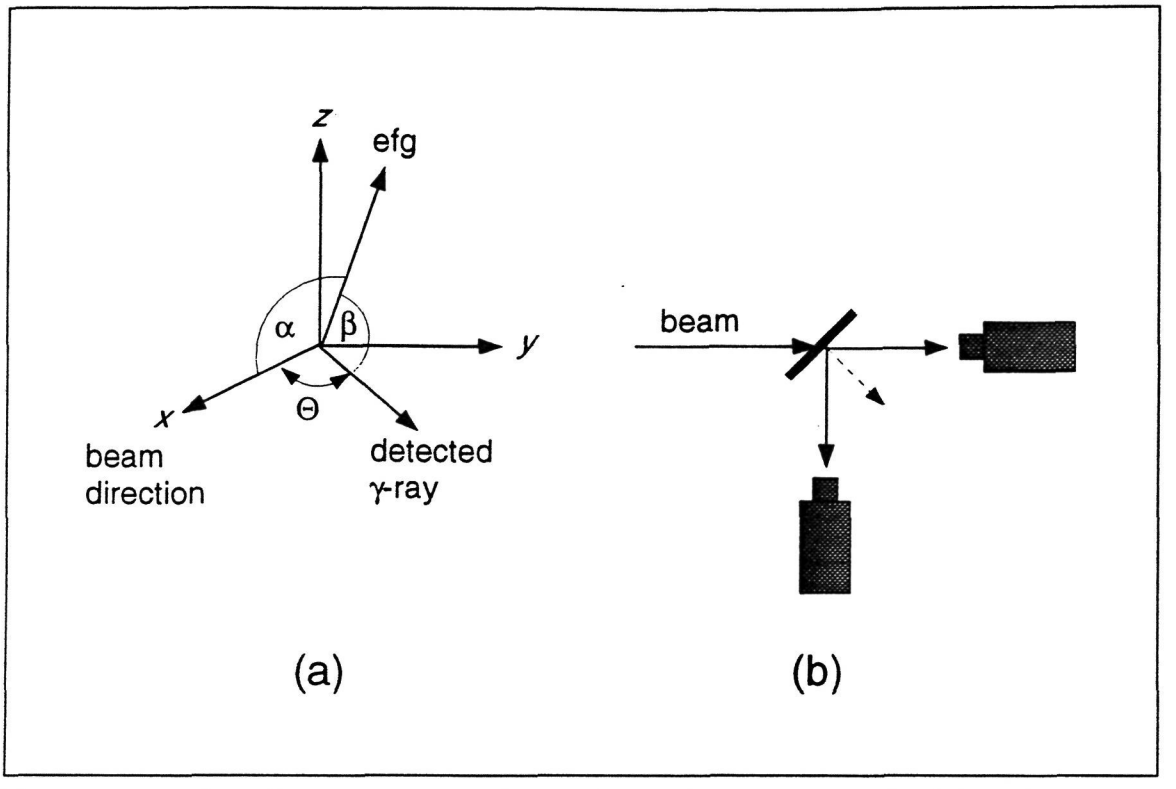

Figure 2.3 : Coordinate system and experimental arrangement for TDPAD measurements.

of eqn. (2.19) the indices k_i and N_i are treated like vector angular momenta, and thus their values are restricted by the triangular condition $0 \leq k \leq \text{Min } (2I, 2k_1, 2k_2)$ and $-k_i \leq N_i \leq k_i$. Also parity conservation requires that the values of k_i run only over even values.

In the case of a partially oriented sample such as highly oriented pyrolytic graphite (HOPG), where the c-axes of the compressed microcrystallites lie within a 1° cone, with the *a*- and *b*-axes oriented randomly, further simplifications occur when averages are taken over the azimuthal angles ϕ_1 and ϕ_2, imposing the additional restriction $N_1 = N_2 \equiv N$. Referring to fig. 2.3, the angular distribution becomes [17]

$$W(\alpha,\beta,\Theta;t) = \sum_{\substack{k_1 k_2 \\ N>0}} A_{k_1 k_2} G^N_{k_1 k_2} f^{k_1 k_2}_{N\Theta}$$
$$= \sum_{k_1 k_2} A_{k_1 k_2} G^{\text{eff}}_{k_1 k_2}(\alpha,\beta,\Theta) \qquad (2.22)$$

where

$$f^{k_1 k_2}_{N\Theta} = \sqrt{\frac{(k_1-N)!(k_2-N)!}{(k_1+N)!(k_2+N)!}} P^N_{k_1}(\cos\alpha) P^N_{k_2}(\cos\beta)(2-\delta_{N0})$$

and $G^{\text{eff}}_{k_1 k_2}$ has been defined to include the angular functions $f^{k_1 k_2}_{N\Theta}$, where the Θ dependence is implicit by virtue of its relationship with β [17]. Here Θ is the angle of emission of the γ-ray relative to the beam axis, and the angles α, β define the orientation of the efg axis with respect to the incident beam and γ-ray direction, respectively.

In the case of a sample containing an ensemble of randomly oriented microcrystallites the angular distribution reduces to

$$W(\Theta,t) = \sum_{k}^{k_{max}} A_{kk} G_{kk}(t) P_k(\cos\Theta). \qquad (2.23)$$

When applied to the fitting of experimental data, the expressions derived above are subject to several corrections. In the γ–γ case the effects of finite solid angle entail the factors Q_{ki}, with

$$A^{\text{eff}}_{k_1 k_2} = A_{k_1}(1) Q_{k_1} A_{k_2}(2) Q_{k_2}. \qquad (2.24)$$

If σ, δ are the gausssian widths accounting for finite time resolution and spread in the efg interaction, respectively, the perturbation factor can be written as

$$G^{N_1 N_2}_{k_1 k_2}(t) = \sum_{p=0}^{3} S^{N_1 N_2}_{k_1 k_2 p} \cos(g_p \omega_0 t) \exp(-\frac{1}{2} g_p^2 \omega_0^2 \sigma^2) \exp(-\frac{1}{2} g_p^2 \omega_0^2 \delta t^2). \qquad (2.25)$$

In most experimental situations the measurements are usually reduced to the spin-rotation function (also called 'ratio function')

$$R(t) = \frac{N(0°,t) - N(90°,t)}{0.5N(0°,t) + N(90°,t)} \qquad (2.26)$$

where $N(\Theta, t)$ are the measured yields at each angle. In terms of $G^{\text{eff}}_{k_1 k_2}$ it can be shown that [18]

$$R_{\text{theor}}(t) \approx \frac{2}{3} \sum_{k_1 k_2} A^{\text{eff}}_{k_1 k_2} \hat{G}^{\text{eff}}_{k_1 k_2}(\alpha, \beta, \Theta) \tag{2.27}$$

where

$$\hat{G}^{\text{eff}}_{k_1 k_2}(\alpha, \beta, \Theta) = G^{\text{eff}}_{k_1 k_2}(\alpha, \beta, 0°) - G^{\text{eff}}_{k_1 k_2}(\alpha, \beta, 90°) \tag{2.28}$$

and the approximation has a relative error [19]

$$\begin{aligned} \frac{\Delta R}{R} &= \frac{1}{3} \sum_{k_1 k_2} A_{k_1 k_2} \text{eff} \left\{ G^{\text{eff}}_{k_1 k_2}(\alpha, \beta, 0°) + 2 G^{\text{eff}}_{k_1 k_2}(\alpha, \beta, 90°) \right\} \\ &< 1\%. \end{aligned}$$

In a situation where the probe nuclei occupy different sites, each exposed to a static quadrupole interaction with fractional occupation f_i, we write

$$R_{\text{theor}}(t) = \frac{2}{3} \sum_i f_i \left\{ \sum_{k_1 k_2} A^{\text{eff}}_{k_1 k_2} \hat{G}^{\text{eff}}_{k_1 k_2 i} \right\}. \tag{2.29}$$

2.4 Calculation of Electric Field Gradients.

A non-spherical electric charge distribution surrounding a nucleus generates electric field gradients V_{ij} at the site of the nucleus. There are various factors that influence the magnitude of V_{ij}. For free atoms, the unpaired valence electron is the main source of the efg [20,21]. Electrons in fully occupied orbitals give very little or zero contribution. The core electrons may reduce the strength of the field gradient through a process called Sternheimer screening, $V_{zz} = V^0_{zz}\{1 - \gamma(r)\}$ [22]. In molecules or solid materials, the neighbouring atoms also contribute an efg to the site of the probe nuclei. The existence of other atoms may cause polarization of the core electrons of the probe nuclei and, instead of screening, the core electrons enhance the efg through a process called antiscreening.

The electric field gradient at the probe nucleus can be expressed as [3]

$$V_{ij} = \int \rho(\vec{r})(3x_i x_j - \delta_{ij} r^2) r^{-5} d^3r - \sum_l Z_l (3X_i^l X_j^l - \delta_{ij} R_l^2) R_l^{-5}, \qquad (2.30)$$

where the nuclear probe is at the origin surrounded by an electron density $\rho(\vec{r})$. The symbols Z_l and X_i^l indicate the charges and positions of the l^{th} neighbouring nuclei, respectively, and $R^2 = X_1^2 + X_2^2 + X_3^2$.

The total charge density and the charge distribution of the l^{th} ions can be calculated if one knows the exact n-electron wave function $|\Psi\rangle$. The procedure by which the total charge is partitioned among the atoms is designated as Mulliken population analysis [23]. Theoretically $|\Psi\rangle$ can be calculated by solving the Schrödinger equation of the system, $H|\Psi\rangle = E|\Psi\rangle$. Unfortunately, in most cases the Schrödinger equation involving many electrons is not solvable, but has to be approximated. However, there are various methods that can be used to approximate the solution to many body problems. The most well known is probably the Hartree-Fock approximation. In the past few years density functional theory has been widely used for various systems [6,7]. In this work we use both methods to estimate electric field gradients at various sites in the material under study.

The Hamiltonian of a system that consists of n electrons and N nuclei with positions $\vec{r}_i$ and $\vec{R}_I$, respectively, can be written as [21,23]

$$H = T_N + V_{NN} + T_e + V_{eN} + V_{ee} \qquad (2.31)$$

where the individual operators correspond to:

- Kinetic energy of the nuclei, M_I is the mass of nucleus I,

$$T_N = -\frac{\hbar^2}{2} \sum_{I=1}^{N} \frac{1}{M_I} \nabla_I^2$$

- Electrostatic interactions between nuclei,

$$V_{NN} = \sum_{I<J}^{N} \frac{Z_I Z_J e^2}{|\vec{R}_I - \vec{R}_J|}$$

- Kinetic energy of electrons,

$$T_e = -\frac{\hbar^2}{2m_e} \sum_{i=1}^{n} \nabla_i^2$$

- Potential energy between electrons and nuclei,

$$V_{eN} = -\sum_{i=1}^{n} \sum_{I=1}^{N} \frac{Z_I e^2}{|\vec{r}_i - \vec{R}_I|}$$

- Electrostatic interactions between electrons,

$$V_{ee} = \sum_{i<j}^{n} \frac{e^2}{|\vec{r}_i - \vec{r}_j|}.$$

In the Born-Oppenheimer approximation the nuclei are considered to stay in fixed positions since the mass of a nucleus is much greater than that of an electron, and thus the first term is zero. The second term, representing the nuclear-nuclear electrostatic interactions, contributes a constant factor to the total energy and has no effect on the operator eigenfunctions. The Hamiltonian of the system can then be simplified by ignoring the first two terms of equation (2.31), thus

$$H = T_e + V_{eN} + V_{ee}. \tag{2.32}$$

It is also convenient to separate H into one-electron and two-electron contributions:

$$H = \sum_{i=1}^{n} h(i) + \sum_{i<J}^{n} g(i,j), \tag{2.33}$$

where

$$h(i) = -\frac{\hbar^2}{2m} \nabla_i^2 - \sum_{I=1}^{N} \frac{Z_I e^2}{|\vec{r}_i - \vec{R}_I|} \tag{2.34}$$

and

$$g(i,j) = \frac{e^2}{|\vec{r}_i - \vec{r}_j|} \tag{2.35}$$

Since they describe each electron's kinetic and potential energy in the field of the nuclei (the 'core'), the one-electron operators $h(i)$ are called the core Hamiltonians. As mentioned above, the exact solution of the Schrödinger equation $H|\Psi\rangle = E|\Psi\rangle$ with a many electron Hamiltonian is very difficult; usually one handles the problem by using various approximations.

2.4.1 Hartree-Fock Approximation.

If one neglects electron-electron interactions ($1/(|\vec{r}_i - \vec{r}_j|)$, the Hamiltonian of the system is just the sum of the core Hamiltonians,

$$H = \sum_i^n h(i). \tag{2.36}$$

The eigenfunction of the corresponding Schrödinger equation is a product of the individual spin orbital wave functions $\chi_i = \psi_i \times \alpha_i$, where ψ_i is the orbital wave function and α_i is the spin of the i^{th} electron. Taking the Pauli principle into consideration, one can write the antisymmetric n-electron wave function as a Slater determinant,

$$\Psi(x_1, x_2, \cdots, x_n) = (N!)^{1/2} \begin{vmatrix} \chi_i(x_1) & \chi_j(x_1) & \cdots & \chi_k(x_1) \\ \chi_i(x_2) & \chi_j(x_2) & \cdots & \chi_k(x_2) \\ \vdots & \vdots & \ddots & \vdots \\ \chi_i(x_n) & \chi_j(x_n) & \cdots & \chi_k(x_n) \end{vmatrix}, \tag{2.37}$$

where the factor $(N!)^{1/2}$ is the normalization factor. The above notation can be simplified by writing the diagonal elements only,

$$\Psi(x_1, x_2, \cdots, x_n) = (N!)^{1/2} |\chi_i(x_1), \chi_j(x_2) \cdots \chi_k(x_n)\rangle . \tag{2.38}$$

In this approximation, only the movement of electrons with parallel spin is correlated. Those with spins antiparallel are not correlated and may have the same orbital wave function.

Using a single Slater determinant as the ground state function, $\langle\Psi_0|H|\Psi_0\rangle = E_0$, and the variational principle, one can derive one-electron differential equations in which their eigenfunctions resemble the spin orbital wave functions χ_i [25]

$$f(i)\chi_i(x_i) = \varepsilon_i\chi_i(x_i). \tag{2.39}$$

This equation is called the Hartree-Fock equation. The Fock operator $f(i)$ has the form

$$f(i) = h(i) + v^{HF}(i), \tag{2.40}$$

where the potential $v^{HF}(i)$ is the average potential from other electrons. As a consequence of taking the Pauli principle into consideration, i.e. using antisymmetric wave functions, the potential $v^{HF}(i)$ does not only depend on the classical Coulomb interaction, but also on the exchange interaction which has no classical analogue.

Since the Hartree-Fock potential $v^{HF}(i)$ depends on the eigenfunctions of other electrons, the equation has to be solved iteratively. Firstly, one has to guess the initial wave functions used to calculate the potential; secondly, after solving the n-equations and generating new eigenfunctions, the potential can be recalculated. The iteration stops if the last calculation gives results consistent with the previous step. The procedure is called the Self Consistent Field (SCF) method.

Self Consistent Field Calculations.

An SCF calculation is performed by introducing a set of basis functions, $\{\phi_\mu(\vec{r})\}$. The spatial part of the spin orbital wave functions can be expanded in terms of the basis,

$$\psi_i = \sum_{\mu=1}^{k} C_{\mu i}\phi_\mu \qquad i = 1, 2, \cdots, k. \tag{2.41}$$

The number of basis functions is ideally infinite, so that any function can be expanded without losing information. However, for computational reasons one has to limit the number in the basis set. The simplest set is called the minimal basis set, in which every subshell of the atomic orbitals is expressed in terms of the minimal set. For example: an $s-$function is represented by 1 basis function, $p-$functions (p_x, p_y, p_z) are represented by 3 basis functions, etc.

Expressing the orbital functions ψ_i in the basis set $\{\phi_\mu\}$, the Hartree-Fock equation of an arbitrary electron in an orbital ψ_i can be written as

$$f(i)\sum_\nu C_{\nu i}\phi_\nu(i) = \varepsilon_i \sum_\nu C_{\nu i}\phi_\nu(i). \tag{2.42}$$

To calculate the energy ε_i one multiplies the above equation on the left and integrates the equation. The results can be expressed in a matrix equation

$$\sum_\nu^k F_{\mu\nu}C_{\nu i} = \varepsilon_i \sum_\nu^k S_{\mu\nu}C_{\nu i} \qquad i = 1, 2, \cdots, k. \tag{2.43}$$

where $F_{\mu\nu}$ is the Fock integral $\langle\phi_\mu|f(1)|\phi_\nu\rangle$ and $S_{\mu\nu}$ is the overlap integral $\langle\phi_\mu|\phi_\nu\rangle$. The matrix equation is called the Roothaan equation and can be written in a simple form, $FC{=}SC\varepsilon$.

The Roothaan equation is simpler if one uses an orthonormal basis set. The basis set $\{|\phi_\mu\rangle\}$ can be orthogonalized by transforming $|\phi_\mu\rangle$ into new functions $\left|\phi'_\mu\right\rangle$ by an operator X, such that $\left\langle\phi'_\mu|\phi'_\nu\right\rangle = \delta_{\mu\nu}$. The matrix X is related to the overlap matrix S by the relation $X^\dagger SX{=}1$. By diagonalizing S we can write $X{=}Us^{1/2}$, where U is the unitary matrix that diagonalized S into s. The Roothaan equation now can be written as

$$F'C' = C'\varepsilon, \tag{2.44}$$

where $F'{=}X^\dagger FX$ and $C'{=}X^{-1}C$.

A flow chart of the Hartree-Fock calculation is shown in fig. 2.4. The program calculates the consistency of the expansion coefficients $C_{\nu i}$ of eqn. (2.43) during the iteration. The iteration stops if their values do not change in two consecutive steps. Once the elements of $C_{\nu i}$ are found, other properties of the system can be calculated.

Basis Functions

The one-electron orbital functions ψ_i are best represented by Slater type orbital functions [26]. These functions are the natural solution of the central force problem and are linear in r in their exponential term. For example, a $1s$ Slater function is written as

$$\phi_{STO}^{1s} = (\zeta^3/\pi)^{1/2} \exp(-\zeta r). \tag{2.45}$$

However, for computational reasons, Gaussian type functions are simpler to handle mathematically in the numerical calculations. The Gaussian type orbital functions have quadratic r in their exponential term; e.g. a $1s$ function takes the form

$$\phi_{GTO}^{1s} = (2\alpha/\pi)^{3/4} \exp(-\alpha r^2). \tag{2.46}$$

As a compromise one uses the combination of the two to get the minimal basis STO-nG functions. In this notation, a one-electron orbital function ψ_i is expressed as a Slater type function, but the latter is expanded into n primitive Gaussian functions. For example, $1s$ and $2p$ Slater type orbitals are written as

$$\begin{aligned} \phi_{STO}^{1s}(\zeta = 1) &= \sum_{i=1}^{n} d_{i,1s} \phi_{GTO}^{1s}(\alpha_{i,1s}) \\ \phi_{STO}^{2p}(\zeta = 1) &= \sum_{i=1}^{n} d_{i,2p} \phi_{GTO}^{2p}(\alpha_{i,2sp}). \end{aligned}$$

The expansion coefficients d_i and the exponential parameters α_i are determined by a least squares fit to the corresponding Slater functions with ζ=1. The parameters α can be scaled for different values of ζ by the relation α'=$\alpha_1\zeta^2$, where α_1 is the value of α for

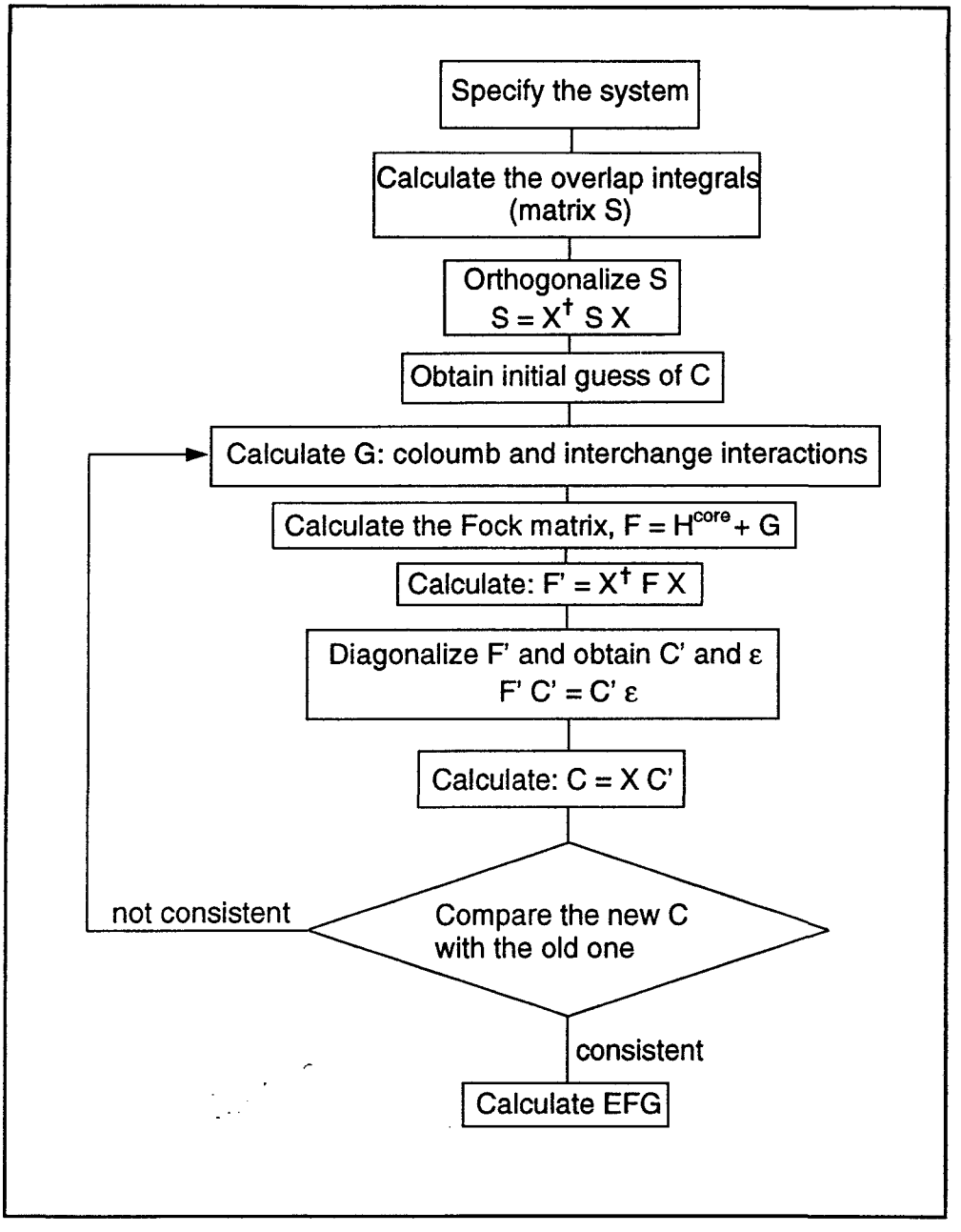

Figure 2.4: A flow chart for the SCF Hartree-Fock calculation.

ζ=1 (the fit value). The values of ζ for particular atoms are given by Huzinaga's table [27]. For computational efficiency the exponents of the Gaussian functions take the same values for s and p wave functions, for example the exponents $\alpha_{i,2sp}$ are used for both $2s$ and $2p$ orbitals.

Theoretically a Slater function can be expanded in a complete set of Gaussian orbitals without losing information. However, one has to limit the number in the expansion for obvious reasons. Usually one uses STO-nG with n$\leq$6, since beyond this point the advantages of using Gaussian functions is diminished because most of the computing time is spent for integral calculations. The most common minimal basis used is STO-3G. To get a better representation of the orbital functions for a system of atoms, one may add higher functions to the basis set; e.g. by adding d Slater orbitals to heavy atoms (STO-nG*) and p orbitals to Hydrogen atoms (STO-nG**). These are called polarized basis sets.

There are many types of basis functions available in the G–92 program [28]. One of the most used is the double zeta basis set, l-mnG, e.g. 3-21G, 4-31G, 6-31G, etc. These basis sets are also called the split valence band basis sets because the valence electrons are expressed in two Slater functions STO-mG and STO-nG with different ζ. The core electrons are still represented by STO-lG functions. For example, the 3-21G basis functions for the second row atoms ($Li - Ne$) are:

– for the core electrons

$$\phi_{1s}(\zeta') = \sum_{i=1}^{3} d_{i,1s}\phi_{GTO}^{1s}(\alpha_{i,1s}),$$

– for valence electrons

$$\begin{aligned} \phi'_{2s}(\zeta') &= \sum_{i=1}^{2} d_{i,2s}\phi_{GTO}^{1s}(\alpha'_{i,2sp}) \\ \phi''_{2s}(\zeta'') &= \phi_{GTO}^{1s}(\alpha''_{i,2sp}) \end{aligned}$$

$$\begin{aligned}\phi'_{2p}(\zeta') &= \sum_{i=1} 2d_{i,2p}\phi^{2p}_{GTO}(\alpha'_{i,2sp}) \\ \phi''_{2p}(\zeta'') &= \phi^{1p}_{GTO}(\alpha''_{2sp}).\end{aligned}$$

2.4.2 Density Functional Theory

Density functional theory (DFT) is a method of handling the many-electron system without calculating the n-electron wave function $|\Psi_0\rangle$ [6,7,29–31]. The electronic properties of the system are expressed in terms of the electron density $\rho(\vec{r})$ and spin density ρ_σ. For example, in the Thomas-Fermi model, the ground state energy can be written as [31]

$$E[\rho] = \int V(\vec{r})\rho(\vec{r})d^3r + \frac{e^2}{2}\int \frac{\rho(\vec{r})\rho(\vec{r}')}{|\vec{r}-\vec{r}'|}d^3r d^3r' + \frac{3}{10}(2\pi^2)^{3/2}\int \rho(\vec{r})^{5/2}d^3r. \qquad (2.47)$$

The first two terms in the above equation are the energy of the electron charge density $\rho(\vec{r})$ in an external potential $V(\vec{r})$ and the Coulomb repulsion energy of a classical charge distribution $\rho(\vec{r})$, respectively. The third term is the kinetic energy of a homogeneous electron gas. The charge density $\rho(\vec{r})$ is not calculated from the wave function $|\Psi_0\rangle$, but it can be derived directly from the above equation. By introducing a Lagrange parameter μ, it can be shown [31] that

$$\rho(\vec{r}) = \frac{(2m)^{3/2}}{3\pi^2}\left\{\mu - V(\vec{r}) - e^2\int \frac{\rho(\vec{r}')}{|\vec{r}-\vec{r}'|}d^3r'\right\}. \qquad (2.48)$$

The Hohenberg-Kohn-Sham theory states that ground state energy of an n-electron system is a functional of the electronic density $\rho(\vec{r})$,

$$E[\rho] = \int V(\vec{r})\rho(\vec{r})d^3r + F[\rho] \qquad (2.49)$$

The functional $F[\rho]$ does not depend on the external potential $V(\vec{r})$ but is determined solely by the charge density $\rho(\vec{r})$. By calculating the charge density one can determine other electronic properties.

Exchange and correlation functional.

The Thomas-Fermi model (eqn. 2.47) is inaccurate for two reasons. Firstly the kinetic energy is calculated from a homogeneous electron gas; secondly it neglects exchange and correlation effects. The latter are introduced in the unknown functional $F[\rho]$ of the Hohenberg-Kohn-Sham theory,

$$F(\rho) = \frac{e^2}{2}\int \frac{\rho(\vec{r})\rho(\vec{r}')}{|\vec{r}-\vec{r}'|}d^3r d^3r' + T_0[\rho] + E_{xc}[\rho], \tag{2.50}$$

where $T_0[\rho]$ is the kinetic energy of noninteracting electrons and $E_{xc}[\rho]$ is the exchange and correlation energy.

By substituting eqn. (2.50) into (2.49) one can write the ground state energy as

$$E[\rho] = \int V(\vec{r})\rho(\vec{r})d^3r + \frac{e^2}{2}\int \frac{\rho(\vec{r})\rho(\vec{r}')}{|\vec{r}-\vec{r}'|}d^3r d^3r' + T_0[\rho] + E_{xc}[\rho]. \tag{2.51}$$

This equation is minimized by a variational principle:

$$\int \delta\rho(\vec{r})\left\{V(\vec{r}) + e^2\int \frac{\rho(\vec{r}')}{|\vec{r}-\vec{r}'|}d^3r' + \frac{\delta T_0[\rho(\vec{r})]}{\delta\rho(\vec{r})} + \frac{\delta E_{xc}[\rho(\vec{r})]}{\delta\rho(\vec{r})}\right\}d^3r = 0. \tag{2.52}$$

From eqn. (2.52) one may imagine the system as a non-interacting electron with effective potential

$$V_{\text{eff}}(\vec{r}) = V(\vec{r}) + e^2\int \frac{\rho(\vec{r}')}{|\vec{r}-\vec{r}'|}d^3r' + v_{xc}(\vec{r}), \tag{2.53}$$

where an exchange-correlation potential has been defined as

$$v_{xc}(\vec{r}) = \frac{\delta E_{xc}[\rho]}{\delta\rho(\vec{r})}. \tag{2.54}$$

To get the charge density $\rho(\vec{r})$ one first has to solve the Schrödinger equation

$$\left\{-\frac{1}{2m}\nabla^2 + V_{\text{eff}}(\vec{r})\right\}\chi_\mu(\vec{r}) = \varepsilon_\mu\chi_\mu(\vec{r}) \tag{2.55}$$

to get χ_μ, then the charge density $\rho(\vec{r})$ can be calculated using equation

$$\rho(\vec{r}) = 2\sum_{\mu}^{N/2}|\chi_\mu(\vec{r})|^2, \tag{2.56}$$

where the summation index μ runs over the lowest eigenvalues ε_μ. Because the V_{eff} in the Schrödinger equation depends on $\rho(\vec{r})$, eqs. (2.53) and (2.56) have to be solved iteratively using the SCF method.

Local density approximation.

In this method the exchange-correlation energy is approximated by

$$E_{xc}[\rho] = \int \rho(\vec{r})\varepsilon_{xc}[\rho]d^3r, \tag{2.57}$$

where $\varepsilon_{xc}[\rho]$ is the exchange-correlation energy per electron of a homogeneous electron gas of density $\rho(\vec{r})$. The exchange-correlation potential now can be written as

$$v_{xc}(\vec{r}) = \frac{d\{\rho(\vec{r})\varepsilon[\rho]\}}{d\rho(\vec{r})} \tag{2.58}$$

The Schrödinger equation (2.55) now takes a simple form since V_{eff} depends only on the charge density $\rho(\vec{r})$.

In a system where electrons are not correlated, the exchange energy per electron $\varepsilon_x[\rho]$ is given by [31]

$$\varepsilon_x[\rho] = -\frac{3e^2}{4\pi}(3\pi^2\rho)^{1/3}, \tag{2.59}$$

and the corresponding exchange potential according to eqn (2.58) is

$$v_x(\rho) = -\frac{e^2}{\pi}(3\pi^2\rho)^{1/3}. \tag{2.60}$$

The Schrödinger equation (2.55) can be solved easily for V_{eff} depends only on the charge density $\rho(\vec{r})$.

The local density approximation can be improved by incorporating several corrections to the exchange-correlation energy (E_{xc}), e.g. by including gradient corrections and considering the nonuniformity of the charge density. In a series of papers [32–35] Becke

reported the evolution of improvement in DFT theory from gradient-corrected exchange-correlation to exact exchange functional. A detailed discussion of the matter can be found in the references cited.

2.5 Gaussian-92 (G–92).

The G–92 code [28] comprises a system of programs released by the Carnegie Mellon University in Pittsburgh, USA, for the use of physicists and chemists concerned with theoretical calculations of electronic properties of solids. In particular, the application here has focused on the calculation of electric field gradients in matter using cluster model theory.

The user can exercise a wide degree of flexibility; for example it is possible to modify the atomic basis sets, which are based on the tables of Huzinaga [27].

A typical input file might look as follows:

1. a command line, for example: **# HF 3-21G PROP SCF=direct SCFCYC=100**

#	:	a symbol indicates the command line
HF	:	the calculation will be performed using the Hartree-Fock method
3-21G	:	the 3-21g double-zeta basis functions will be used
PROP	:	a command to calculate the electronic properties
SCF=direct	:	the iteration will be performed in a *direct* way (the two-electron integrals will not be saved in the memory and have to be calculated every time they are needed; it is slow, but needs little disk space)
SCFCYC=100	:	the maximum number of cycles in the iteration is 100

2. a blank line

3. title job
4. a blank line
5. charge and multiplicity of the molecule or cluster (multiplicity M=2J+1, where J is the total spin of the electrons)
6. a list of the atoms in the cluster and their coordinates
7. a blank line
8. the initial values of the parameter to be optimized (if optimization is requested).

Chapter 3

Experimental

3.1 Methods for producing nuclear alignment.

It will be recalled from the discussion in Chapter 2 that a fundamental requirement for perturbed angular correlation measurements was the production of alignment in the isomeric nuclear state. Before describing the experimental aspects of TDPAD, we review briefly here other methods for producing alignment.

3.1.1 Low temperature nuclear alignment.

In the presence of a magnetic field the nuclear m-substates are split into m levels with energies $E_m = \mu_N g B m$. According to the Boltzmann distribution, in thermal equilibrium at temperature T, each m-sublevel has population probability

$$P_m = \frac{\exp -E_m/kT}{\sum_m \exp -E_m/kT}.$$

The ratio of populations in state m and $m+1$ depend on the energy splitting $E_{(m+1)} - E_m$. To achieve considerable population difference, this energy splitting must be comparable to the thermal energy kT [36–38]. Since the nuclear moment μ_N is extremely small, very low temperatures and large fields are required to achieve considerable population difference in the m-sublevels. For instance, using superconducting magnets fields in the region of 10 Teslas (10^5 Gauss) can be produced; the required temperature to achieve an appreciable population difference is then of the order of 10^{-3} °K. Some materials such as iron groups, lanthanides and actinides have strong internal magnetic fields ($\sim 500T$) due

to unpaired electrons. By implanting probe nuclei into certain materials, the requirement for expensive external magnets can be eliminated.

3.1.2 Laser induced orientation.

The nuclear spins can also be polarized through the interactions with electronic spins. This method is mostly used in Laser spectroscopy and is called optical pumping [38]. For example, consider free atoms that have electronic spins I=$\frac{1}{2}$ and I=$\frac{3}{2}$ at ground and first excited states, respectively. A circularly polarized beam with m=+1 is used to induce transitions from the ground state (I,m)=$(\frac{1}{2},\frac{1}{2})$ and $(\frac{1}{2},-\frac{1}{2})$ to the excited states with (I,m)=$(\frac{3}{2},\frac{3}{2})$ and $(\frac{3}{2},\frac{1}{2})$. Since there is no restriction on the magnetic quantum number other than Δm=0,$\pm$1 in the de-excitation process, the ground states will be no longer equally populated:

$$\begin{aligned}
(\tfrac{3}{2},\tfrac{3}{2}) &\longrightarrow (\tfrac{1}{2},\tfrac{1}{2}) \qquad \text{with} \quad \Delta m = -1 \\
(\tfrac{3}{2},\tfrac{1}{2}) &\longrightarrow (\tfrac{1}{2},\tfrac{1}{2}) \qquad \text{with} \quad \Delta m = 0 \\
(\tfrac{3}{2},\tfrac{1}{2}) &\longrightarrow (\tfrac{1}{2},-\tfrac{1}{2}) \qquad \text{with} \quad \Delta m = -1
\end{aligned}$$

The population of the m=$\frac{1}{2}$ substate in the ground state thus increases with respect to that in the m=$-\frac{1}{2}$ substate. By repeating the process many times and using a laser beam with specific polarization (m=+1 or −1) one can make the ensemble polarized completely. The nuclear spins will then follow the orientation of the electronic spins, i.e. being polarized at room temperature.

3.1.3 Alignment by radiation correlations.

In 1940 Hamilton [39] proposed the use of γ-γ cascades to select an aligned sub-ensemble from a randomly oriented sample. The method is called directional correlation

since only the directions of the emitted γ-rays are considered; the polarizations of the γ-rays are not measured. Consider a sample with randomly oriented nuclei that decay via an intermediate state with the emission of two consecutive γ-rays, $(I_o, m_o) \xrightarrow{\gamma_1} (I_i, m_i) \xrightarrow{\gamma_2} (I_f, m_f)$. As described in Chapter 2, if the first γ-ray is detected in an arbitrary direction $\vec{k}_1$, then the second γ-ray from the cascade will in general have an anisotropic distribution relative to $\vec{k}_1$. The detection of γ_1 has acted as a quantum mechanical state selector for the intermediate state by allowing only certain m-states to be populated. As discussed in the previous chapter, this forms the basis of the TDPAC technique.

3.1.4 Alignment following nuclear reactions: TDPAD.

Nuclear alignment can be achieved through the mechanism of nuclear reactions [2,3]. In the TDPAD measurements performed in this work the reaction $^{19}F(p,p')^{19}F^*$ was used to implant recoiling $^{19}F^*$ nuclei into various samples. The incident proton energy was chosen so as to excite a resonance close to 2 MeV for production of the 197 keV isomeric state with spin I=$5/2^+$, $T_{1/2}$=85.5 ns and quadrupole moment Q=0.072(4) b [40]. A consideration of the energetics and angular momentum transfer involved in the reaction leads to the conclusion that the reaction mechanism is predominantly by Coulomb excitation. For the p–^{19}F system the Coulomb barrier is 2.94 MeV and the distance of closest approach of a 2 MeV proton is 6.47 fm, more than twice the nuclear radius of ^{19}F (R=$R_0A^{1/3}$=3.2 fm with R_0=1.2 fm), and thus outside the nucleon-nucleon force range. Moreover, the angular momentum transfer in the reaction, from the ground state I=1/2 to I=5/2, requires a classical impact parameter b=7.8 fm for an l=2 partial plane wave. A semiclassical Born approximation calculation [41] shows that 90% of the inelastically scattered protons should be emitted within a forward cone with half-angle less than 10°. The large transfer in angular momentum to the isomeric state, coupled with the fact that a large fraction of the inelastic protons are emitted close to zero degrees, thus placing

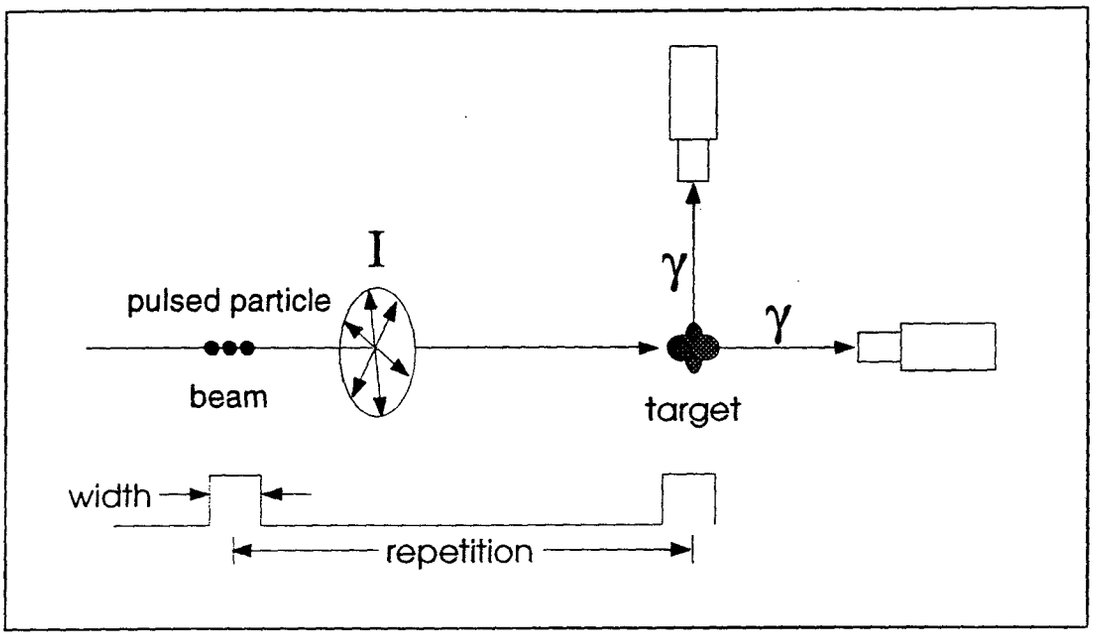

Figure 3.1: Schematic illustration of the TDPAD technique.

restrictions on the populations of the magnetic substates [42], results in an alignment of the nuclear spins preferentially perpendicular to the beam axis (fig. 3.1).

Details of the electronics and detectors are given in section 3.3. Following each accelerator pulse the delayed time spectra $W(\Theta, t)$ from the decaying $^{19}F^*$ nuclei were recorded simultaneously by a time-to-amplitude converter for detectors at 0° and 90° to the beam. The yields at these angles were combined to form the experimental ratio

$$R(t) = \frac{N(0°, t) - N(90°, t)}{0.5N(0°, t) + N(90°, t)} \tag{3.1}$$

where

$$N(\Theta, t) = N_0 e^{-t/\tau} W(\Theta, t) \tag{3.2}$$

is the normalized yield of the 197 keV γ-rays detected at angle Θ after background subtraction. The background level was determined by averaging the time-uncorrelated

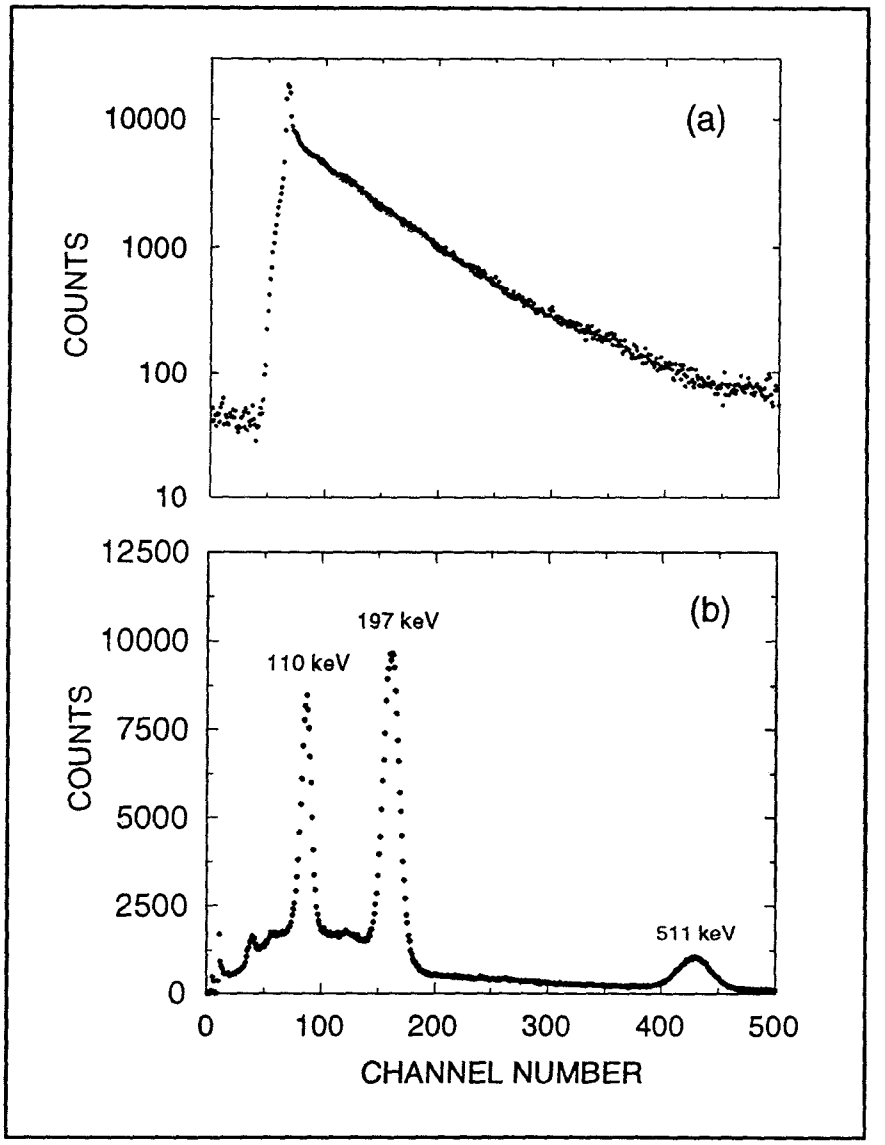

Figure 3.2: (a) A typical time spectrum from TDPAD measurements.
(b) The γ-ray energy spectrum from the $^{19}F(p,p')^{19}F^*$ reaction.

events in the region of the time spectrum preceding the prompt peak at t=0. These spectral features are illustrated in fig. 3.2a. The corresponding energy spectrum shown in fig. 3.2b indicates the presence also of a γ-ray transition with energy 110 keV. Since this prompt γ-ray proceeds through a level with spin 1/2 in ^{19}F, its angular distribution is isotropic, thereby providing an internal monitor for normalization purposes which automatically includes any correction for detector efficiencies.

The particular form of $R(t)$ is chosen for several reasons: since higher order terms $k_i >$ 2 in the expansion (2.15) are small, the denominator in (3.1) is approximately constant; furthermore the exponential decay factor in the yields $N(\Theta, t)$ (eq. 3.2) is eliminated, consequently enhancing the perturbation signal that can be seen superimposed upon the exponential decay in fig. 3.2a. Examples of reduced $R(t)$ spectra are shown in Chapters 4–6.

An excitation function for the ^{19}F$(p,p')^{19}$F* reaction leading to production of the second excited state of ^{19}F at 197 keV is shown in fig. 3.3. The resonance at 2.02 MeV is well pronounced, with a width of approximately 80 keV.

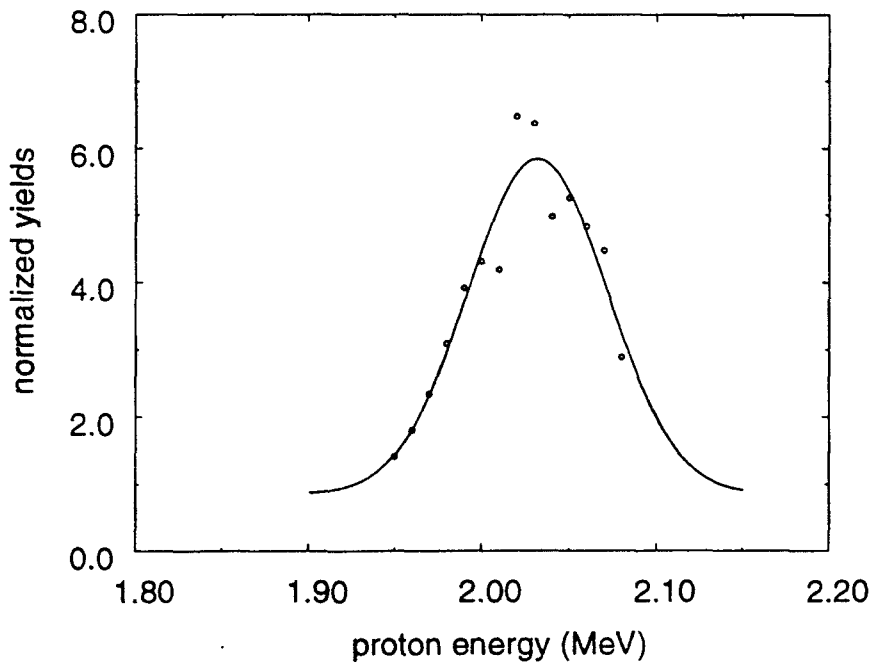

Figure 3.3: Excitation function for the ^{19}F(p,p′)^{19}F* reaction.

The TDPAD technique confers several advantages over its TDPAC predecessor. Since the first γ-transition has been replaced by an accelerator timing pulse, effectively the intensity of a single γ-radiation is measured, rather than a coincidence rate. Furthermore, owing to the large number of isomeric nuclei accessible through nuclear reactions involving protons, deuterons, ^{3}He, ^{4}He and even heavy ions, a wide variety of probes becomes available over lifetimes ranging from a few ns to several μs.

The main advantage of TDPAD is the selective sensitivity to the local structure, regardless of bulk distortions of the host. In the case of ^{19}F* and ^{22}Na*, the isomeric nuclei used as probes in these investigations, it is not possible to perform nuclear quadrupole resonance, nuclear orientation or Mössbauer measurements, so that TDPAD offers a unique way in which to investigate quadrupole interactions. A further advantage is that the measurements are performed within a relatively short time ($< 1\mu$s) after implantation, thus avoiding problems with subsequent migration of the implanted species.

A potential disadvantage, however, devolves on the radiation damage that can occur in the target sample. This will be discussed in section 3.5.

3.2 The Accelerator

A single stage vertical Van de Graaff accelerator (CN-7.0MV) was used to produce ion beams for the TDPAD measurements. The system consists of three main components: a voltage generator, acceleration tube, and transport system. The first two components are contained in a pressure vessel (see fig. 3.4).

The voltage generator basically consists of a belt made of flexible insulating material running between two rotating pulleys and a charge collector in the upper part of the machine (upper electrode). A set of needles having positive potential relative to the belt is pointed close to the lower pulley such that electric discharges from the needles create

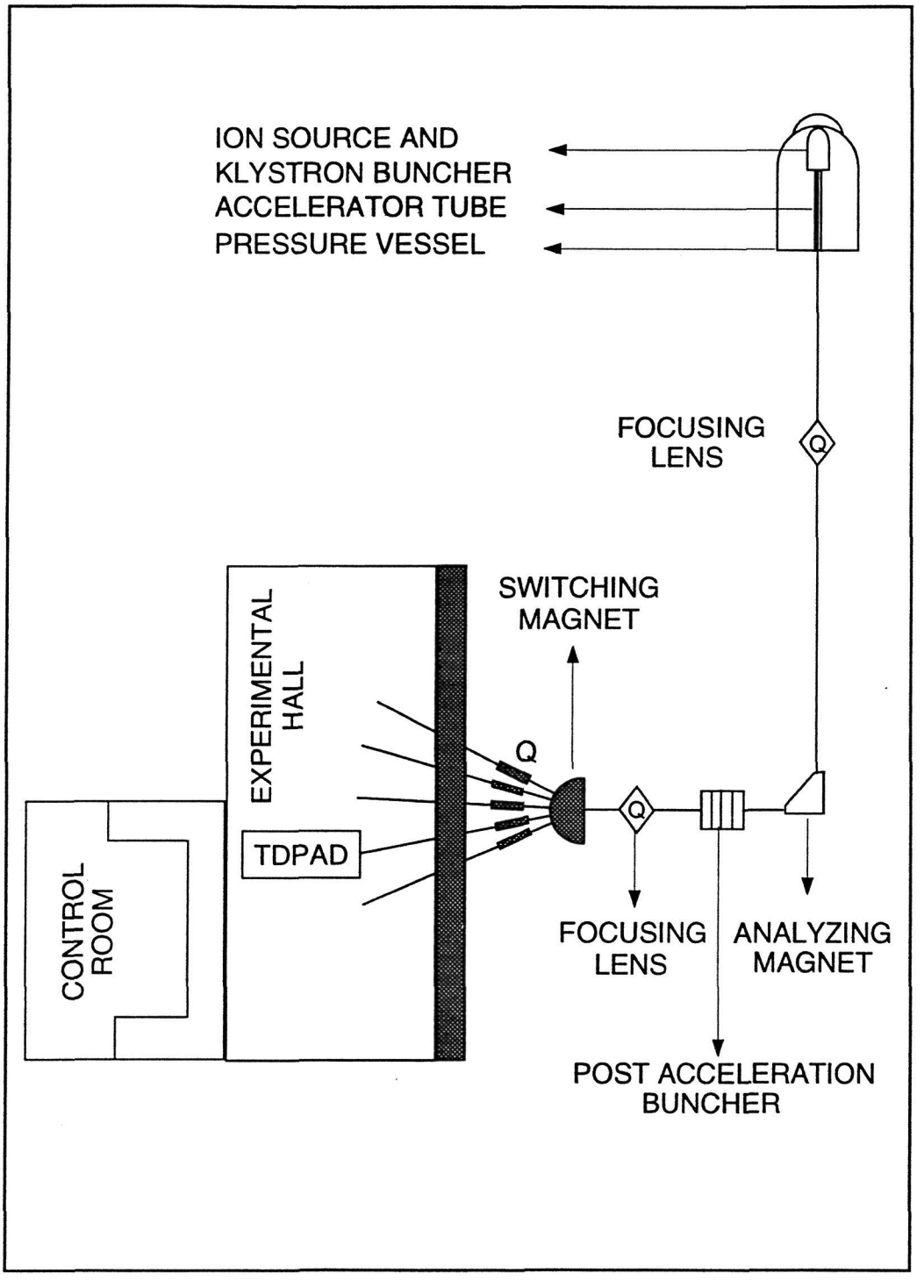

Figure 3.4: Schematic diagram of the 7 MV Van de Graaff accelerator and the experimental facilities.

positive ions on the belt. The belt transports the charge to the upper pulley where another set of needles strips off the charges. The upper electrode accumulates the charge until maximum voltage is achieved. The upper electrode must be insulated from the surroundings to avoid discharge to surrounding objects. The maximum voltage is limited by charge loss via sparking and the rate of charge supplied by the running belt. The generator in IRMM has a maximum voltage of 7 megavolts.

The acceleration tube consists of 140 stainless steel electrodes. These electrodes divide evenly the high voltage from the upper electrode so that each electrode may support voltages up to 50 kV. A 2.5 cm glass insulator separates one electrode from the other. The total length of the tube is about 4 m. Charged particles crossing along the inner part of the tube will experience a uniform potential gradient and gain energy $E = Ze \times V$, where V is the total potential. Singly charged particles (e.g. protons) may gain kinetic energy up to 7 MeV, doubly charged particles twice that amount.

The ion beam is first produced by a radio frequency ion source. A gas (H_2 or He) is released from a container into an ionization chamber, where an alternating electric field strips off the electrons. A static electric field repels the ions to a focusing lens. A 30° analyzing magnet then selects ions with the right mass, rejecting other contaminants. At this stage the ion source produces a continuous low energy ion beam.

Since TDPAD experiments require short bursts of particles, in the pulsed mode of operation an aperture placed after the ion source chops the continuous beam into pulses of duration 15–20 ns with a repetition period of 1600 ns. To get better resolution in timing, the length of the pulses is shortened further by a buncher. This device modulates the speed of ions as a function of their relative position. Relative to the speed of ions in the mean position of a pulse, those in the leading edge are slowed down and those in the trailing edge are accelerated. As a result the length of the pulses is compressed. Pulse widths of 1.5 ns FWHM can be obtained with this system [43].

The whole assembly comprising the upper electrode, ion source, buncher and acceleration tube are placed in a pressure vessel (see fig. 3.4). To avoid charge loss due to corona discharge and thus increasing the upper voltage limit, the vessel is filled with dielectric gases containing a mixture of carbon dioxide, nitrogen and sulfur hexafluoride. In contrast, to avoid collisions between the energetic particles and the surrounding gas, the inner parts of the ion source and acceleration tube are kept under vacuum. All of the beam tubes for transporting the beam are also kept under high vacuum.

Following a quadrupole lens placed after the acceleration tube to focus the vertical beam from the accelerator, an analyzing magnet deflects the beam into the horizontal plane. To achieve even shorter pulses, another buncher may be placed after the analyzing magnet. This post-acceleration buncher can compress the pulses down to 0.3 ns without losing total charge per pulse [44]. Another quadrupole lens is placed after the post-acceleration buncher before the beam is directed by a switching magnet to the target sample in the experimental hall. Before the beam is allowed to impinge on the target, a timing signal is derived from a capacitative pick-off system situated just before the sample chamber. This signal, suitably delayed, provides the stop pulse for the time-to-amplitude converter which records the delayed time spectrum.

3.3 Detectors and Electronics.

A block diagram of the system of detectors and electronics is shown in fig. 3.5. The principal detectors, situated at 0° and 90° to the beam direction, were 5.08 cm × 5.08 cm diameter NaI(Tl) crystals, coupled to RCA8850 photomultipliers. In order to minimize systematic errors, these detectors were frequently interchanged. A third 12.70 cm × 12.70 cm diameter NaI(Tl) detector, placed at 55° to the beam axis, served as an independent normalization monitor so that $R(t)$ could also be determined from separate

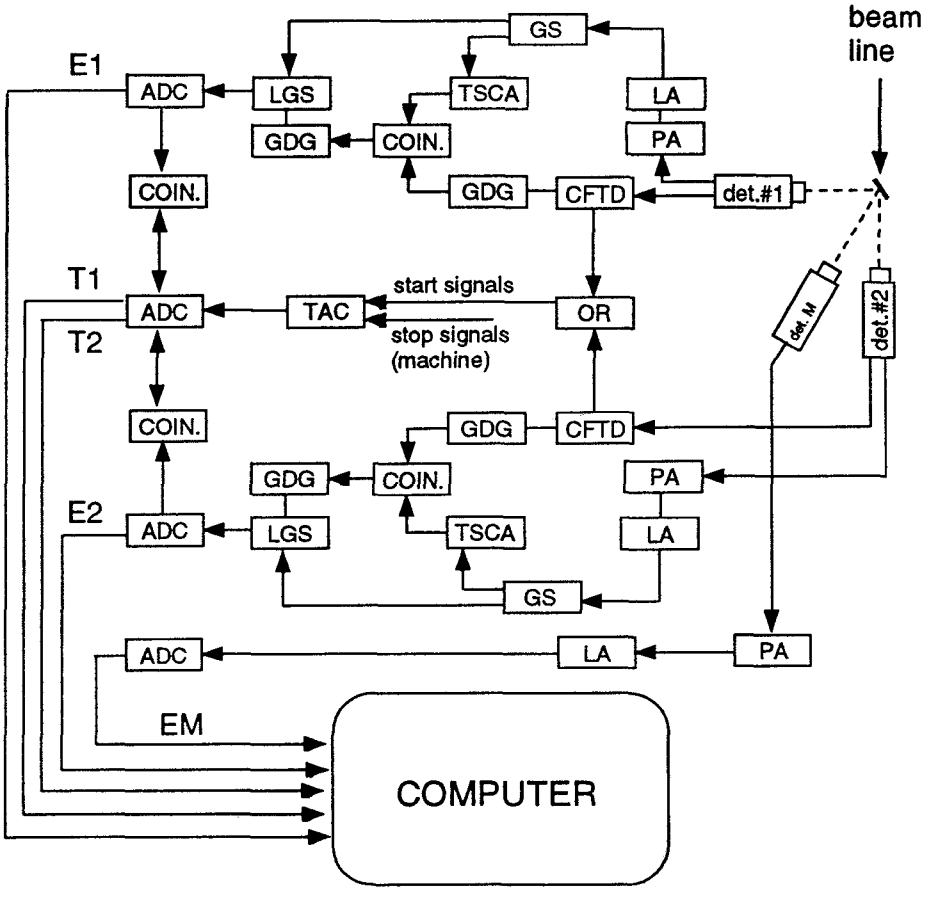

det.#1	NaI-Tl detector	LGS	Linear Gate and Strecher
PA	Pre Amplifier	ADC	Analog to Digutal Converter
LA	Linear Amplifier	TAC	Time to Amplitudee Converter
CFTD	Constant Fraction Time Discriminator	GS	Gain Stabilizer
		E1/E2	Energy Spectrum from det. #1 or #2
OR	OR circuit	T1/T2	Time Spectrum from det. # 1 or #2
TSCA	Time Single Channel Analyser	EM	Energy Spectrum from det. M (monitor)
GDG	Gate and Delay Generator		
COIN.	Coincidence circuit		

Figure 3.5: The schematic diagram of the electronics.

runs with the same detector at different angles.

A single time-to-amplitude converter (TAC) was used to record simultaneously the delayed time spectrum from each detector, thus ensuring that both time scales were commensurate. The fast timing outputs from the detectors were routed via constant fraction timing discriminators (CFTD) into a fast OR circuit, whose output served as a start signal for the TAC. The accelerator timing signal, appropriately delayed, provided the stop pulse for the TAC. With this arrangement the TAC was activated only when an event was detected in either detector. Both timing and linear energy signals were processed by the ADCs, thus allowing each two-dimensional (E_i,T_i) event to be stored in a (512, 1024) array of computer memory. Internal logic circuits controlling the computer-ADC interface routed events to the appropriate sector of memory assigned to each detector.

The repetition period of the beam signal was set to 1600 ns. Since the isomeric state half-life was only 85.5 ns, this effectively eliminated the possibility of detecting γ-rays from a preceding beam pulse. The time spectrum was calibrated regularly using an ORTEC 418 Time Calibrator module. The prompt peak resolution time was typically 2.3 ns FWHM. By choosing appropriate digital windows on the energy axis, the corresponding time spectrum could be projected accordingly onto the time-axis.

3.4 The sample.

The target samples were supported on an aluminum sample holder as shown in fig. 3.6. Aluminum was chosen as the material for the sample holder for several reasons. First, it is a relatively soft metal, thus easy to fabricate. During the bombardment of the sample by energetic particles, heat is produced and must be removed as fast as possible to keep the temperature of the sample constant. Since aluminum has good conductivity, extra heat produced in the sample can quickly be removed to a cooling system. Aluminum also

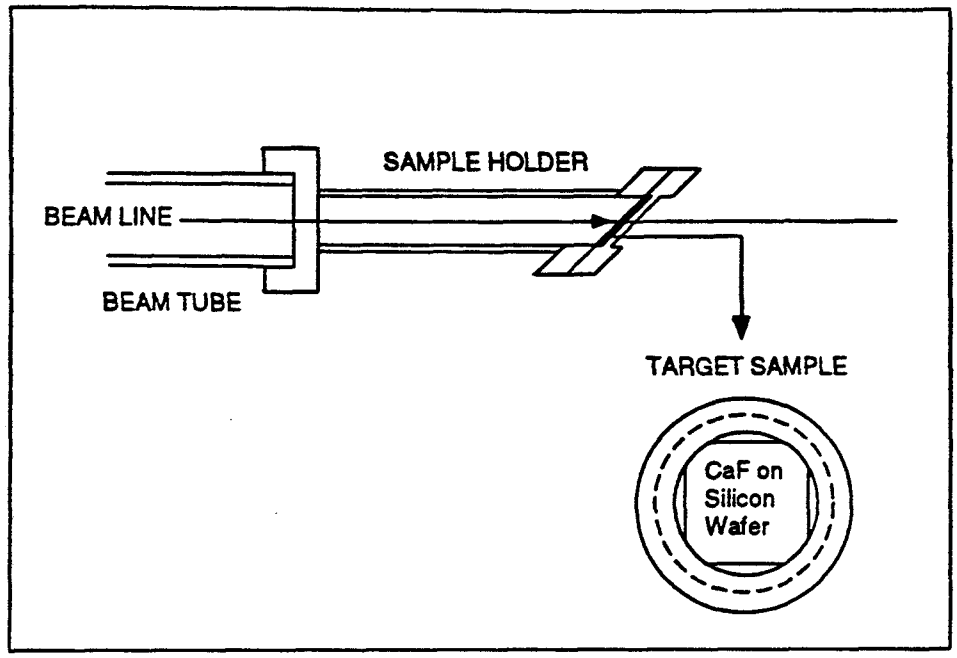

Figure 3.6: The schematic diagram of the sample holder.

has low a attenuation factor for γ-rays. The γ-rays produced by the nuclear reaction have to penetrate not only the sample material itself but also the target holder before reaching the detectors. A material of low atomic number such as aluminum is thus preferred.

The samples investigated in this work were graphite [vitreous carbon (VC) and highly oriented pyrolytic graphite (HOPG)] and the semiconductor materials Si, Ge, and GaAs. All of the samples were in the form of 1 cm $\times$ 1 cm wafers, with thicknesses 0.3–1 mm. Once the wafers had been properly cleansed, a 30 μg/cm^2 CaF_2 film was evaporated on to the substrates to provide fluorine as a target for the $^{19}F(p,p')^{19}F^*$ and $^{19}F(\alpha,n)^{22}Na^*$ reactions used in the measurements. Recoiling $^{19}F^*$ nuclei were thereby implanted into the host materials HOPG, VC, Si, Ge and GaAs. An additional reason for choosing CaF_2 as the primary target was the fact that it possesses cubic symmetry and consequently would produce zero efg (hence no quadrupolar interaction) at the site of any $^{19}F^*$ recoils which fail to enter the host material.

3.5 Possible implantation damage.

Energetic ions traversing solid material may cause damage to the host crystalline structure. The ions lose their kinetic energy through various interactions with electrons and core nuclei of the target material. Collisions with electrons may cause excitation or ionization. In the excitation process the atomic electrons gain energy and move to higher energy states, while ionization happens if the energy transfer to the electrons is larger than the chemical bond energies between the electrons and their parent atoms. These two processes are called electronic stopping. The recoil electrons act as new energetic charged particles and will lose their kinetic energy through the same scenario.

It is also possible that the incoming particles come close to the core and interact with the target nuclei. This process is called nuclear stopping [45–46]. The kinetic energy transferred in the nuclear process is much larger than that produced in electronic processes, since both projectile and target particles have comparable mass. The target nuclei may be excited into isomeric states and recoiled into deeper regions of the medium. Using this technique one can implant heavy ions using light particle beams, such as protons. This is the method used in the TDPAD measurements described here.

While a collision of an energetic ion with electrons will not result in much energy transfer owing to the small mass of the electron compared to that of the incoming ion, nevertheless, since electrons outnumber nuclei electronic stopping processes contribute a large fraction ($\sim$ 80%) to the total stopping power of a material [47]. In contrast, although collisions with core nuclei result in a large energy transfer, the probability of events is low owing to the small size of the nucleus. Because of the wide application to materials science, in recent years recoil implantation methods have been investigated extensively [47–55] and a great deal of information, both theoretical and experimental, is now known about the range-energy loss of ions in matter.

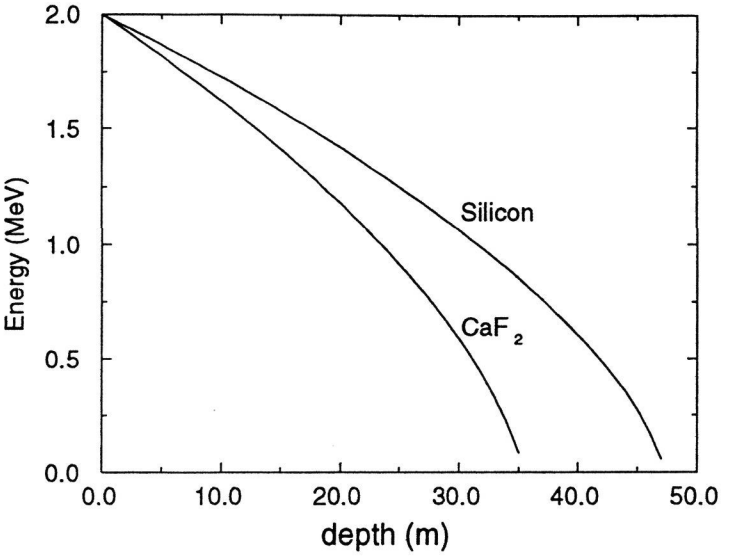

Figure 3.7: Energy of the primary proton beam vs. depth in calcium fluoride and silicon.

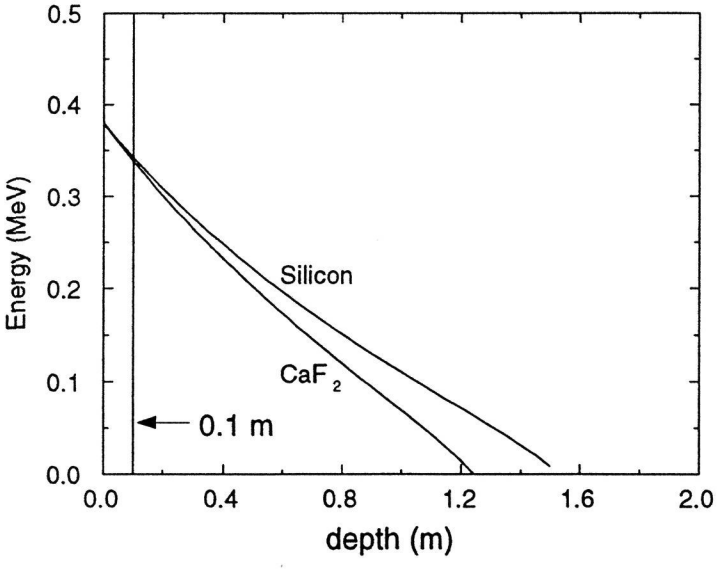

Figure 3.8: Energy of ^{19}F nuclei vs. depth in calcium fluoride and silicon.

It is clear that in the nuclear stopping process an atom may be displaced from its crystalline site. Also secondary effects may occur as the incident ion generates collision cascades along its track, producing damage in the target material. The damage production depends on the energy deposited in the target material and on the fluence of the incoming ions. The threshold energy for displacement is about 25 eV [50]. Such studies of radiation damage due to proton bombardment on semiconductor material have been the subject of several investigations [51–54]. Kreische et al. [56] have pointed out that after slowing down in the lattice the excited probe nuclei come to rest in less than 0.1 ps. At room temperature the defects in the surroundings of the probe nuclei anneal within less than 1 ns by migration and recombination, and the nuclear state 'feels' only the influence of the unperturbed crystal lattice during its lifetime, if it is longer than about 10 ns.

In this work a 2 MeV proton beam was used to recoil $^{19}F^*$ into materials under study. Typical currents were in the range 0.2–0.7 μA. Based on the kinematic calculations of energy loss versus depth (fig. 3.7), the incoming protons lose all their kinetic energy at about 35 μm depth in CaF_2 and 47 μm in silicon. Since the CaF_2 layer has a thickness of 30 $\mu g/cm^2$ ($\approx$ 0.1 μm) only about 0.2% of the incoming kinetic energy is lost in this layer. Thus most protons pass easily through this layer to reside in the bulk of the sample, which has a thickness of the order of mm.

The energy deposited in the sample material is not uniformly distributed, the maximum concentration being located just before the maximum range [53]. This range can be extended if the implanted ions are channeled along certain directions in the crystalline lattice of the target samples [57]. From fig. 3.7, it can be expected that damage caused by implantation of 2 MeV protons in silicon will have a maximum concentration in the region of 25–50 μm below the surface, or deeper if channeling occurs.

In contrast, the recoil-implanted fluorine atoms have a much smaller range than that

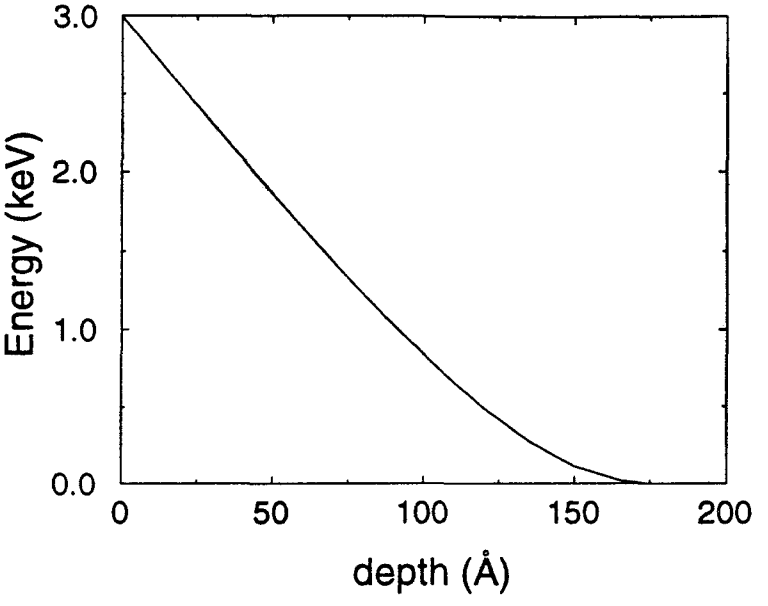

Figure 3.9: Energy of $^{19}F^*$ nuclei vs. depth in silicon.

of the protons. For an elastically scattered 2 MeV incident proton the maximum recoil energy of ^{19}F is 380 keV. These recoils of course produce no de-excitation γ-rays, but will produce maximum radiation damage at about 1.5 μm depth in Si (fig. 3.7). In a head-on collision the maximum recoil energy for $^{19}F^*$ (E=197 keV) is 360 keV. However, as discussed in 3.1.4, the reaction is expected to proceed predominantly by Coulomb excitation, involving sizeable impact parameters for the partial l-waves and an angular distribution for the inelastically scattered protons which is strongly peaked within a cone of half angle 10°. The recoil energy of $^{19}F^*$ corresponding to a 10° scattered proton is just 3 keV, with a range of about 170 Å in Si, as shown in fig. 3.8. Thus the recoils of interest should stop in locations well removed from the damage regions resulting from the elastic recoils or the primary proton beam.

Certainly the TDPAD signal is so sensitive to local defects that any radiation damage

would be revealed in the quadrupole signal as a considerable broadening. In such regions defects are known to produce a wide distribution of field gradients [56], resulting in a large value for the parameter δ, which would be reflected strongly in the Fourrier transform of $R(t)$. In all the cases studied the broadening effect typically involved spreads of less than 5%, indicating well defined efgs exposed to an environment with minimal damage.

Chapter 4

Quadrupole Interactions of ^{19}F and ^{22}Na implanted in HOPG

4.1 Introduction

Highly oriented pyrolytic graphite (HOPG) is a synthetic form of graphite produced under conditions of high temperature and pressure such that the spread in the *c*-axes of the microcrystallites is typically less than 1°, while the *a*- and *b*- axes are randomly oriented. Each microcrystal consists of carbon atoms arranged in an A–B–A layered structure (see fig. 4.1a) [58]. A unit cell contains two carbon atoms in which each layer contributes one atom (fig. 4.1b).

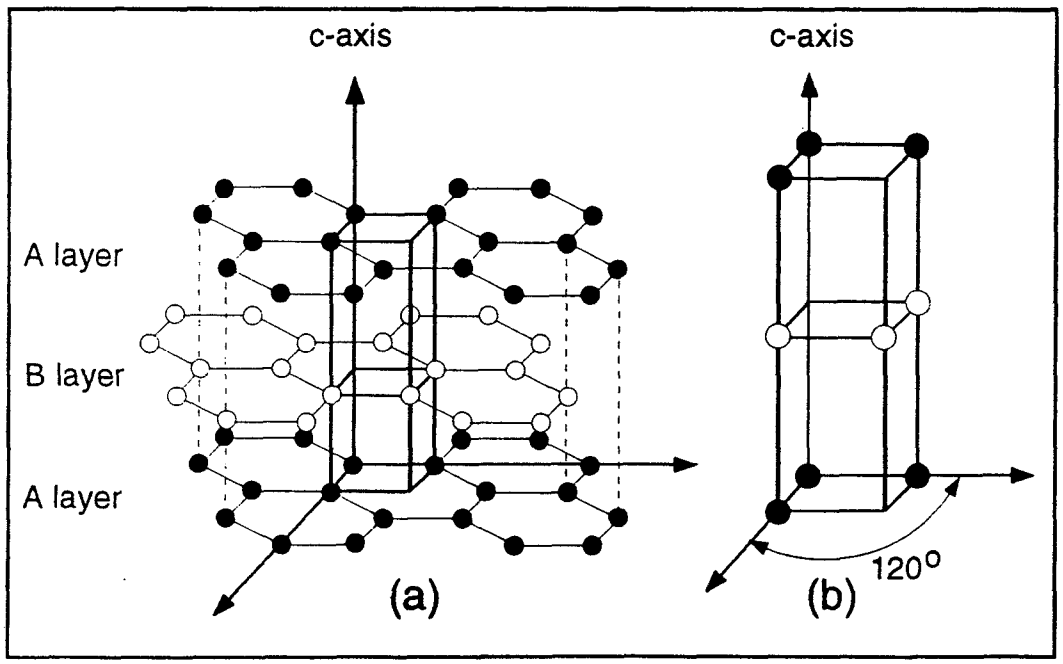

Figure 4.1: (a) An A–B–A layered structure and (b) a unit cell.

Our TDPAD studies of quadrupole interactions of ^{19}F implanted in HOPG were motivated by the following considerations:

(a) The material can be regarded as a pseudo-single crystal, conferring certain advantages for the study of quadrupole interactions, such as narrow linewidths.

(b) As a system with a high degree of order it is ideally suited as a testing ground for theoretical formalisms designed for the calculation of efgs in matter. Specifically, great interest devolved on the predictions of Hartree-Fock (HF) and Density Functional Theory (DFT) methods outlined in Chapter 2.

(c) The low temperature nuclear orientation experiments of Kastelein et. al. [59] in their studies of heavy ions (^{203}Hg and ^{69}Zn) implanted into HOPG revealed the presence of extremely large ($\sim 10^{22}$ V/m^2) field gradients. Since the quadrupole coupling constant contains the product QV_{zz}, this discovery suggested that HOPG might be a suitable host for the detection of very small quadrupole moments. In this respect the first excited state of ^{22}Na at an excitation energy of 583 keV is of particular interest. On a pure shell model basis, a half-filled shell of protons and neutrons should have a quadrupole moment Q=0 [60]. On the other hand, rotational models or shell models with mixed configurations predict values of Q which should be a few times a typical single-particle value [61–64]. In their early paper Sunyar and Thieberger pointed out that an experimental determination of the quadrupole moments of the ground and first excited states of ^{22}Na could provide a basis for differentiating between the deformed or shell model descriptions [60]. In an attempt to gain information on the magnitude of Q for the first excited state of ^{22}Na, we implanted ^{22}Na into HOPG using the ^{19}F$(\alpha, n)^{22}$Na* reaction.

(d) From a practical standpoint, a TDPAD measurement on a relatively 'clean' system such as HOPG would provide a convenient test run to check the system of electronics and detectors, together with the software routines required for data reduction and analysis.

4.2 Experimental.

Details of the system of detector and electronics have been described in Chapter 3. The 7MV Van de Graaff accelerator at IRMM was used in pulsed mode to provide a 2.02 MeV proton beam. At this energy a resonance in the $^{19}F(p,p')^{19}F^*$ reaction yields a substantial fraction of $^{19}F^*$ nuclei aligned in the isomeric state at 197 keV ($J^\pi=5/2^+$, $T_{1/2}$=88.5 ns). The pulse width was 2 ns, with repetition period 1600 ns ($\sim 18\times T_{1/2}$), thus ensuring negligible interference from events in the preceding pulse. The timing resolution for prompt events was typically 2.3 ns FWHM.

The samples, as described in section 3.4, were made by evaporating a 30 $\mu g/cm^2$ film of CAF_2 on to substrates of HOPG (typically 0.3 mm thick) and 1 mm thick pellets of vitreous carbon (VC).

Calcium fluoride was chosen as it has cubic symmetry and consequently zero efg. As can be seen from fig. 2.2.b in Chapter 2, the sample was oriented at an angle of 45° to the beam, with the *c*-axis of the HOPG perpendicular to the surface of the sample and in the plane of detectors.

For the case of ^{22}Na implantation, α-particles of incident energy 3.42 MeV were used to populate the 583 keV state ($J^\pi=1^+$, $T_{1/2}$=243 ns) of ^{22}Na using the $^{19}F(\alpha,n)^{22}Na^*$ reaction. In this experiment it was also possible to monitor simultaneously the quadrupole signal from the 197 keV state in $^{19}F^*$, populated by the $^{19}F(\alpha,\alpha')^{19}F^*$.

The measurements were performed by observing simultaneously the γ-rays emitted at

0° and 90° to the beam axis (Θ=0° and 90°), respectively, with two 5.08 cm × 5.08 cm diameter sodium iodide scintillation detectors. The data were recorded in two-dimensional mode (γ-ray energy versus time) so that in the analysis digital windows could be set on the γ-rays of interest. As mentioned in Chapter 3 (see the energy spectrum of fig. 3.2b), the isotropic γ-ray originating from the 110 keV spin 1/2 state in ^{19}F served as an internal normalization monitor. In addition a third 12.07 cm × 12.07 cm diameter sodium iodide was positioned at 55° to the beam direction. Since the 0° and 90° detectors were interchanged frequently, the large monitor could provide a normalization for combining if necessary runs at the two angles with the data from the same detector.

The beam current was about 0.6 μA or less. The background from uncorrelated events was calculated by averaging the counts over the region of negative time as mentioned in Chapter 3.1.4 (see fig. 3.2a). Since it was typically about 1–3% of the yield in the first few channels of the time spectrum, at this background level we were able to measure the distribution function $W(\Theta, t)$ out to several hundred ns. In order to obtain good statistics, typically ten such runs were performed for each sample.

4.3 Data analysis and results.

After background subtraction and normalization, the $N(0°, t)$ and $N(90°, t)$ angular distributions were combined using the ratio function of eqn. (3.1), viz.

$$R(t) = \frac{N(0°, t) - N(90°, t)}{0.5N(0°, t) + N(90°, t)}.$$

The advantages of using HOPG as the host material are immediately apparent from the $R(t)$ functions and their Fourier power transforms presented in figs. 4.2–4.4. Periodic oscillations due to the nuclear quadrupole interactions can clearly be seen in the ratio functions. The Fourier power transform of $R(t)$ shows that the corresponding frequency spectrum for HOPG (fig. 4.2b) is considerably more simple than that of VC (fig. 4.4); it

manifests a very strong peak close to 17 MHz, representing the first harmonic (ν_2) of the frequency triplet expected from the I=5/2 quadrupole interaction, while the fundamental frequency $\nu_1 \sim 9$ MHz and the second harmonic ν_3 are almost completely suppressed. It is clear that the ratio function consists of one interaction only and that the implanted ^{19}F atoms reside in a site with a well defined efg. This is a result of the pseudo-single crystal nature of the material. The Fourier spectrum for the case of VC is more complex, with evidence for the presence of two quadrupole interactions.

From the ratios of the frequencies detected in the Fourier spectra (eqn. 2.14), it was possible to determine the quadrupole frequency $\nu_Q=10\omega/3\pi$ and asymmetry parameter η. These provided initial estimates for ω_0 and η to be used in the theoretical fits, which are shown as solid lines in figs. 4.2a–4.4a.

For HOPG the fits to $R(t)$ were based on eqn. (2.22) which includes exponential factors accounting for finite time resolution and spread in the efg interaction with gaussian widths σ and δ, respectively, viz.

$$W(\alpha,\beta,\Theta;t) = \sum_{\substack{k_1,k_2 \\ p,N\geq 0}} A_{k_1k_2} f^{k_1k_2}_{N\Theta} S^{k_1k_2}_{pN} e^{-(1/2)(g_p\omega_0\sigma)^2} \times e^{-(1/2)(g_p\omega_0\delta t)^2} \cos(g_p\omega_0 t), \quad (4.1)$$

where the k_i take on values of 0,2,4, N is an integer, with $-k_i \leq N \leq k_i$, and p=0,1,2,3. The angles α, β and Θ are shown in fig. 2.2. The following parameters were obtained characterizing the quadrupole interaction in HOPG derived from the $^{19}F(p,p')^{19}F^*$ reaction:

$$\nu_Q = 56.0(6) \text{ MHz}, \quad \alpha = 45.0°(1.5),$$
$$\eta = 0.20(4), \quad \beta = 44.9°(1.5),$$
$$\delta = 0.04(1).$$

Taking Q=0.072(4) b as the quadrupole moment of the 197 keV level [40], ν_Q corresponds to $|V_{zz}|=3.21(18)\times10^{22}$ V/m^2.

Figs. 4.3a and 4.3b display $R(t)$ and its Fourier power transform for the $^{19}\mathrm{F}(\alpha,\alpha')^{19}\mathrm{F}^*$ experiment. Again only one interaction is observed, but in this case the Fourier components exhibit different strengths, the fundamental at 9 MHz being strongly enhanced. The parameters obtained here were:

$$\nu_Q = 57.0(8)\ \mathrm{MHz}, \quad \eta = 0.13(3), \qquad \delta = 0.05(1)$$
$$\alpha = 45.0°(1.7), \qquad \beta = 46.0°(1.7),$$

with $|V_{zz}|$=3.27(19)$\times 10^{22}$ MHz.

For comparison with theory we take the average values of $|V_{zz}|$ and η obtained from the $^{19}\mathrm{F}(p,p')^{19}\mathrm{F}^*$ and $^{19}\mathrm{F}(\alpha,\alpha')^{19}\mathrm{F}^*$ reactions for F implanted in HOPG; these give $|V_{zz}|$=3.24(14)$\times 10^{22}$ V/m^2 and η=0.16(3).

Referring to the VC data in fig. 4.4, the fit shown for $R(t)$ is based on the form of $G_{22}(t)$ for an ensemble of randomly oriented microcrystallites, with

$$R(t) = A_{22}^{\mathrm{eff}} \times \sum_i f_i G_{22}^i, \tag{4.2}$$

where f_i is the fraction of the i-th interaction, and G_{22} is given by eqn. (2.18) viz.

$$G_{22}(t) = \sum_{p=0}^{3} s_{2p} \exp\{-(1/2)(\omega_p\sigma)^2\} \exp\{-(1/2)(\omega_p\delta t)^2\} \cos(\omega_p t), \tag{4.3}$$

where ω_p=$g_p(\eta)\omega_0$ and s_{2p} are calculable coefficients.

In this case two static nuclear quadrupole interactions were required to fit the data yielding :

$$\nu_{Q1} = 57.4(7)\ \mathrm{MHz}, \quad \eta = 0.01(3), \quad \delta = 0.05(1)$$
$$\nu_{Q2} = 18.2(2)\ \mathrm{MHz}, \quad \eta = 0.60(5), \quad \delta = 0.03(1).$$

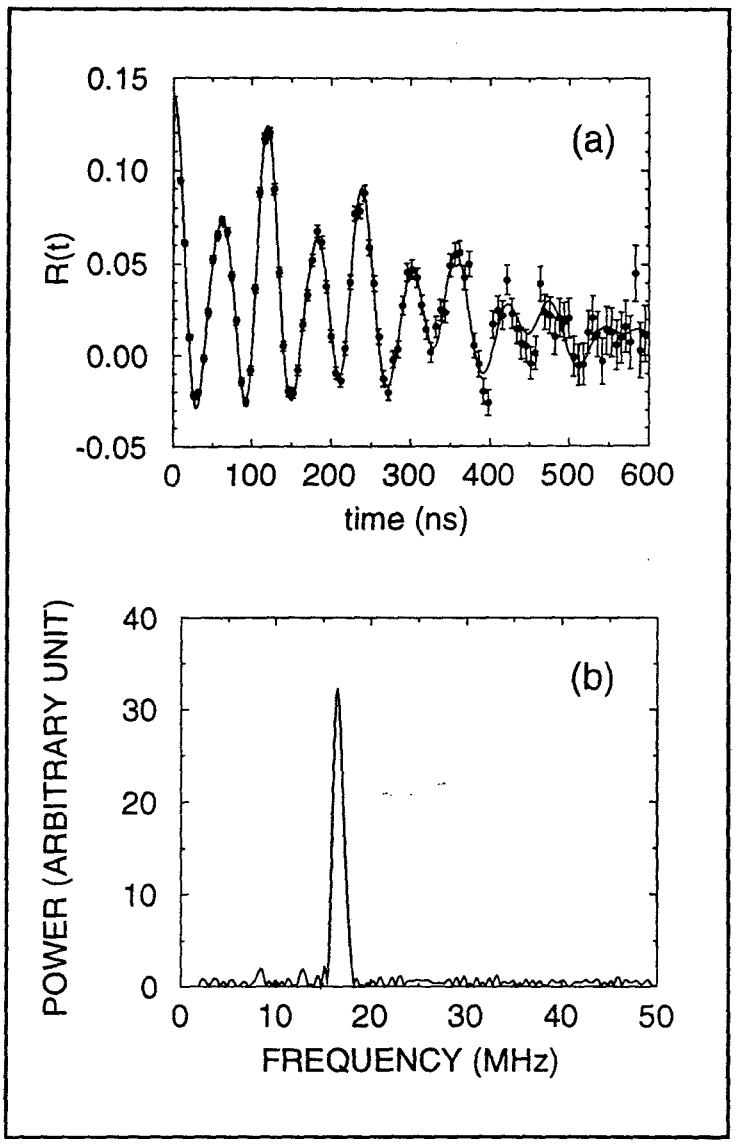

Figure 4.2: (a) The ratio spectrum R(t) of $^{19}F^*$ implanted into HOPG using the $^{19}F(p,p')^{19}F^*$ rreaction and (b) its Fourier power spectrum.

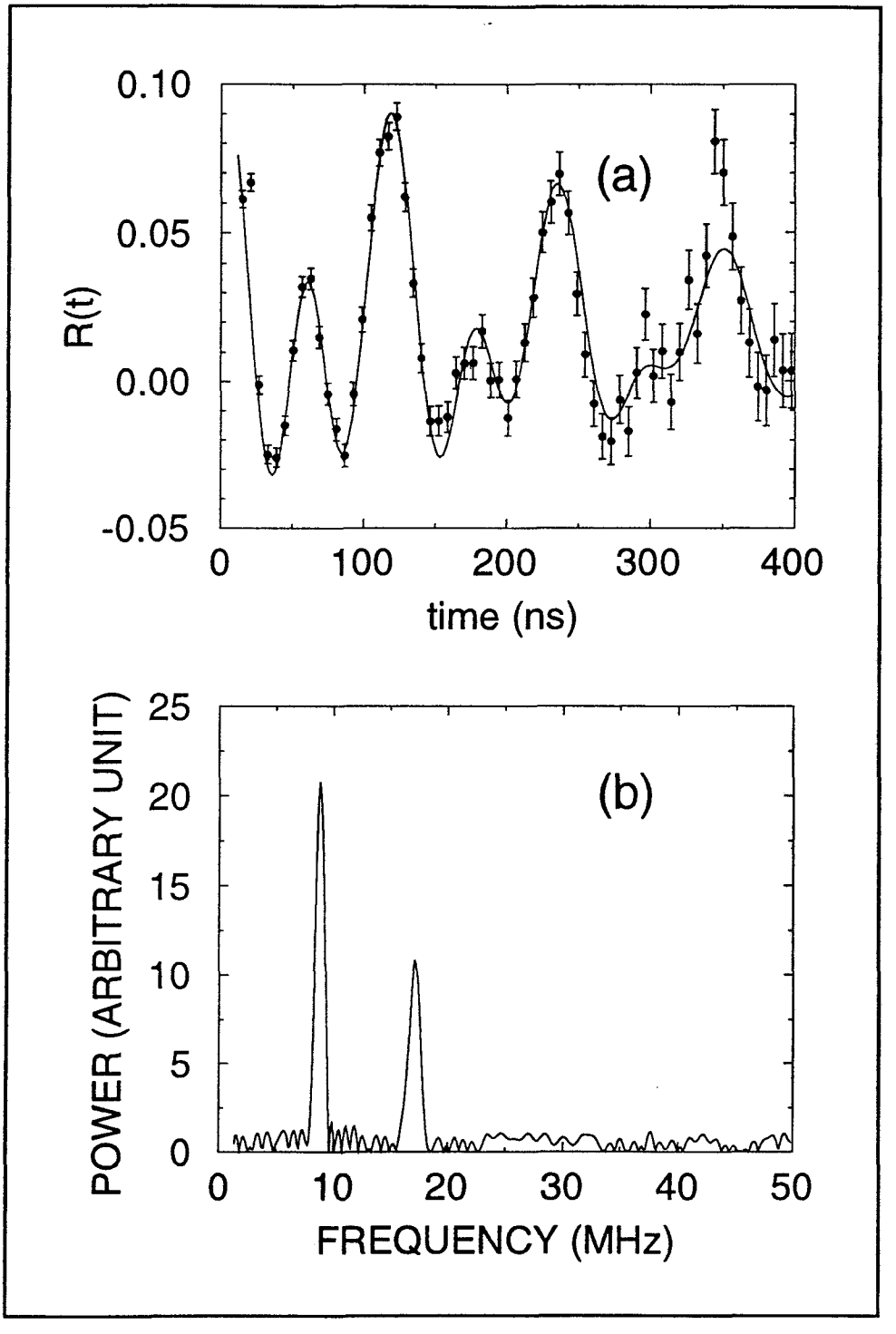

Figure 4.3: (a) The ratio spectrum R(t) of ^{19}F* implanted into HOPG using the ^{19}F(α,α´)^{19}F* reaction and (b) its Fourier power spectrium.

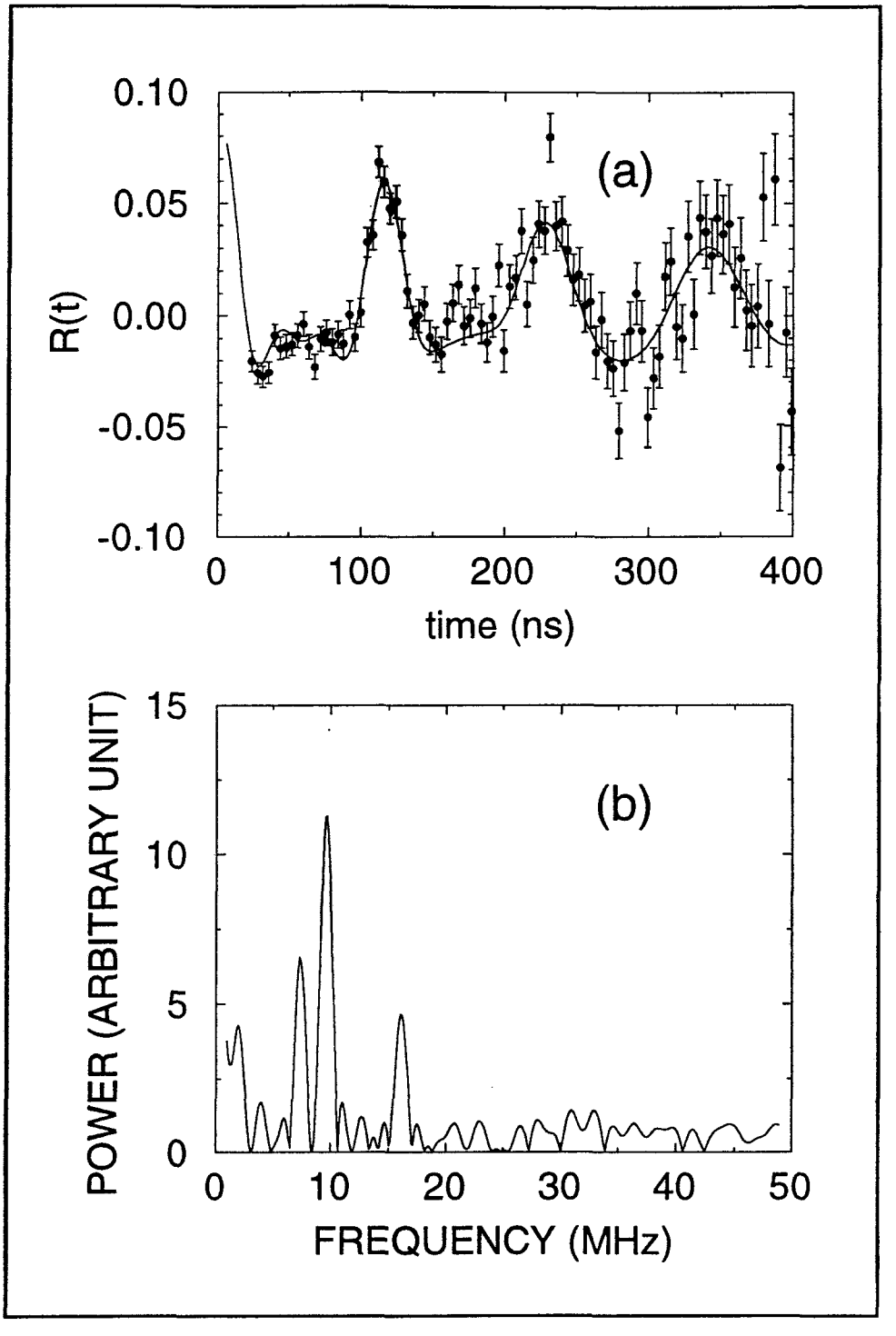

Figure 4.4: (a) The ratio spectrum R(t) of $^{19}F^*$ implanted into VC using the $^{19}F(p,p')^{19}F^*$ reaction and (b) its Fourier power spectrum.

Regarding the results of the $^{19}F(\alpha,n)^{22}Na^*$ experiment, fig. 4.5 shows $R(t)$ for the implantation of $^{22}Na^*$ into HOPG. The flat spectrum indicates no detectable nuclear quadrupole interaction.

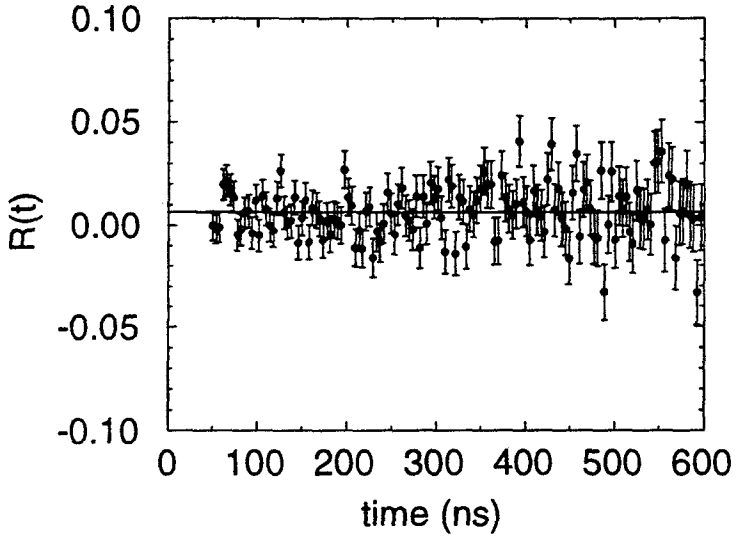

Figure 4.5: The ratio spectrum $R(t)$ of $^{22}Na^*$ implanted into HOPG using the $^{19}F(\alpha,n)^{22}Na^*$ reaction.

4.4 Efg calculations: F in HOPG.

The strategy employed in the efg calculations was to postulate possible sites for the F impurity in HOPG, then compare the measurements with HF and DFT calculations based on a cluster model in which dangling bonds are satisfied with H atoms.

In fig. 4.6 we adopt the same nomenclature as Kastelein et. al. [65] who considered the following configurations for ^{69}Zn and ^{203}Hg impurities *inside* and *between* the layers in HOPG.

(i_1) – a substitutional position inside the layer with point group symmetry D_{3h}; cluster $FC_{12}H_9$.

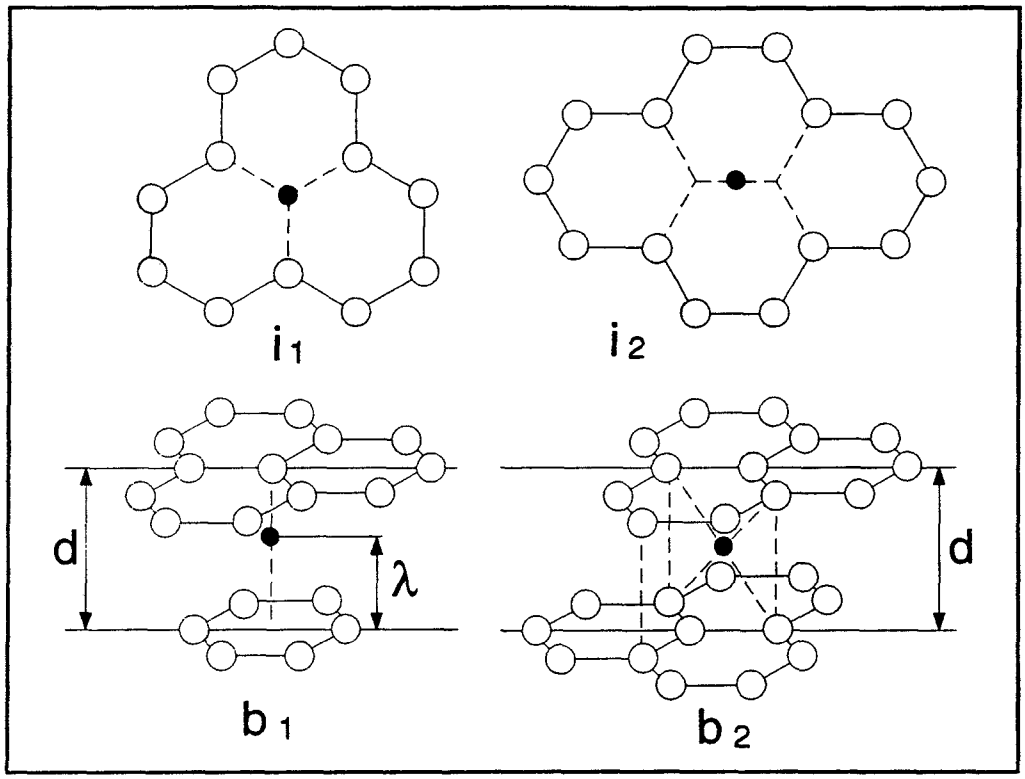

Figure 4.6: Four cluster configurations used in the efg calculations. Hydrogen atoms used to satisfy the dangling bonds are not shown.

(i_2) – an interstitial position inside the layer between two carbon vacancies, with point group D_{2h}; cluster $FC_{14}H_{10}$.

(b_1)– an interstitial position between the layers, with point group D_{2h}; cluster $FC_{19}H_{15}$.

(b_2)– an interstitial position between the layers, with point group C_{2h}; cluster $FC_{26}H_{18}$.

The indicated symmetry groups apply to the local environment of the impurity ions as given in fig. 4.6. Lattice locations b_1 and i_1 have a three-fold symmetry axis parallel to

the c-axis; lattice locations b_2 and i_2 have a two-fold symmetry axis perpendicular to the c-axis. In lattice location b_1 inversion symmetry is absent, because the ion is being held between a single C-atom on one side and a ring of C-atoms on the other side. Therefore, the ion will not be situated exactly midway between the two layers, but will be displaced in the direction of the ring of C-atoms.

Using the Gaussian–92 code both HF and DFT self-consistent methods were employed in the efg calculations. In our DFT calculations we used the local spin density exchange functional of Becke [35], which incorporates corrections involving the gradient of the density, together with the correlation functional of Lee et al. [66], which includes both local and non-local terms.

There are two factors that contribute to the electric field gradient at the F impurity sites in HOPG. The main contributor is the unpaired electrons in the $2p$ orbital. The second factor is the ionic charge distribution from the host crystal. Since the efg is proportional to the inverse cube of the distance, the contribution from the ionic charge distribution surrounding the ^{19}F probe nuclei is small.

In the asymmetric configuration b_1, where the F impurity is held between a single C atom above and a ring of C atoms below, the distance λ shown in fig. 4.6 was varied as a free parameter until the energy was minimized. As pointed out by Kastelein et al. [65], a problem arises in choosing a realistic inter-layer distance d in the presence of an implant. Calculations for d in the range 3.35–4.0 Å showed very little variation (<0.5%) in this minimum energy value. The calculated V_{zz} values indicated in Table 4.2 also show only a slight dependence on the interlayer spacing d. In position b_2 the fluorine is located midway between the layers.

The results of our efg calculations indicate that positions i_1, i_2 and b_1 can be eliminated as possible sites on the basis of values obtained for the asymmetry parameter, η. For example, Table 4.1 shows that for these locations η is either zero (i_1, b_1) or close to

Table 4.1: Results of Unrestricted Hartree-Fock cluster calculations using an STO-3G basis at F impurity sites i_1, i_2 and b_1 in HOPG (see fig. 4.6). The inter-layer spacing is d=3.6 Å and the intra-layer C–C length is 1.42 Å. For site b_1 the parameter λ=2.09 Å.

Position	V_{zz} (10^{22} V/m^{22})	η
i_1	– 2.591	0
i_2	– 2.562	0.88
b_1	– 2.938	0

Table 4.2: The results of cluster model calculations in HOPG for F at position b_2 of fig. 4.6 using Unrestricted Hartree-Fock (UHF) and Density Functional Theory (DFT) methods. The intra-layer C–C length is 1.42 Å.

METHOD	d (Å)	BASIS	V_{zz} (10^{22} V/m^2)	η
UHF	3.35	STO-3G	– 3.740	0.03
UHF	3.60	STO-3G	– 3.805	0.02
UHF	3.80	STO-3G	– 3.854	0.01
UHF	3.70	STO-3G	– 4.217	0.03
DFT	3.35	STO-3G	– 2.942	0.18
DFT	3.60	STO-3G	– 3.051	0.15
DFT	3.70	STO-3G	– 3.086	0.13
EXPERIMENT			$\|V_{zz}\|$=3.24(14)	0.16(3)

unity (i_2), certainly not consistent with the measured value of η=0.16(3). Comparable values of η were also obtained using other basis sets, both in HF and DFT methods.

Table 4.2 indicates results obtained using different basis sets for HF and DFT calculations with fluorine at position b_2. Calculations performed using a basis of STO-3G* gave results which were almost identical to those obtained with the STO-3G basis. It can be seen from Table 4.2 that the DFT method yields lower values of $|V_{zz}|$ and higher asymmetry than the HF predictions, in closer agreement with the parameters derived from the TDPAD measurements. The DFT calculation which gave closest agreement with experiment was obtained for an inter-layer spacing d=3.7 Å, yielding V_{zz}=–3.09×10^{22} V/m^2 and η=0.13 (see Table 4.2). These values compare favourably with the experimentally determined averages $|V_{zz}|$=3.24(14)×10^{22} V/m^2 and η=0.16(3).

4.5 Discussion

4.5.1 Nuclear quadrupole interactions of ^{19}F in graphite materials.

Since there are no results by others for quadrupole interactions studies of F in HOPG, we compare our findings with measurements on other carbon structures. In their investigation of ^{19}F implantation in carbon allotropes, Bharuth-Ram et al. [67] consistently found evidence for two residence sites in all samples studied, including single crystal graphite. In the latter case these authors attributed a well-defined 57 MHz interaction to a tetrahedral interstitial site with 36% occupancy, while a second, low frequency (6 MHz) and heavily broadened (δ=30%) signal, was ascribed to a substitutional site at the 8% occupancy level. The principal interaction, which is of narrow width (δ=3%) and essentially axially symmetric (η=1%), is characteristic of a basically undisturbed C–F bond previously observed in other systems [68–70].

In contrast, our data from both the $^{19}F(p,p')^{19}F^*$ and $^{19}F(\alpha,\alpha')^{19}F^*$ reactions indicate

only one static efg interaction with the quadrupole moment of the 197 keV state. The quadrupole frequencies from both reactions are in good agreement, with an average value of 56.4(5) MHz. Reasonable agreement is also obtained for the angles (α, β)defining the direction of the efg. Allowing for the spread in the c-axes of the crystallites in HOPG, these results are consistent with an efg that is normal to the surface of the sample and in the plane of the detectors. The consistency in the widths ($\sim$ 5%) found for the NQI in both the (p,p') and (α,α') experiments suggest that no appreciable increase in radiation damage occurs at the probe sites when α particles are used as projectiles. This is consistent with the argument outlined in Chapter 2 where we point out that local annealing is expected within a few ns or so.

An interesting feature in the comparison of the (p,p') and (α,α') measurements is the relative strength of the Fourier components manifested in the Fourier power transforms of figs. 4.2.b and 4.3.b. In the former case the first harmonic (ν_2) is enhanced, whereas for the (α,α') data it is the fundamental which dominates. Thus in the $^{19}F(p,p')^{19}F^*$ process the intraband transition m=$\pm$5/2 $\longrightarrow$ m=$\pm$3/2 is dominant. In some situations the ratios of the Fourier components can be related to the orientation of the efg and η in a simple manner [71]. However, it is not possible to determine the 'particle parameters' $A_{k_1k_2}(1)$ of eqn. (2.15), which depend on the dynamics of the reaction mechanism. It should be pointed out that the second harmonic (ν_3) in each case is usually barely detectable because of the exponential damping factors in eqn. (2.25) arising from the finite resolving time and spread in the efg.

Our results for vitreous carbon, on the other hand, indicate the presence of two quadrupole interactions with fractional occupations of 60% and 40% for the 57 MHz and 18 MHz signals, respectively. These are in good agreement with the results of Bharuth-Ram et al. (56 MHz and 17 MHz), but their values of η=0.02 and δ=38% for the low frequency interaction differ significantly from ours (η=0.60, δ=3%).

Regarding the efg calculations for F at sites in HOPG, as mentioned earlier symmetry arguments rule out the possibility of configurations i_1, i_2, and b_1. Both HF and DFT calculations predict axial symmetry for positions i_1 and b_1 to six decimal places, while η=0.88 for i_2 is well outside the experimental limits η=0.16±0.03. Generally speaking calculations of η are considered much more reliable than those of V_{zz}, so we are confident in these conclusions. We conclude therefore that in HOPG fluorine occupies an interstitial site (b_2) midway between the layers with point group symmetry C_{2h}.

The theoretical estimates of V_{zz} and η for position b_2 indicate that the DFT calculations are in better agreement with the experimental results $|V_{zz}|$=3.24(14)×10^{22} V/m^2 and η=0.16(3). The DFT results are in the range $|V_{zz}|$=2.94 to 3.09 ×10^{22} V/m^2 and η correspondingly between 0.18 and 0.13.

The quality of the data and theoretical results vindicate the choice of HOPG as a suitable host for testing current theories.

4.5.2 The quadrupole moment of the first excited state of ^{22}Na.

The ratio function $R(t)$ for implantation of ^{22}Na* (E=583 keV, I$^\pi$=1$^+$1, T$_{1/2}$=243 ns) in HOPG is shown in fig. 4.5. The reaction used in this experiment was ^{19}F$(\alpha, n)^{22}$Na*. The flat spectrum indicates no detectable perturbation of the angular distribution, i.e. $G_{22}(t) \equiv$ constant.

From the standpoint of the nuclear shell model, the presence of six particles in the *sd* shell of ^{22}Na constitutes a complex problem for the calculation of static quadrupole moments. As mentioned earlier, in a pure $d_{5/2}$ configuration, with equal numbers of protons and neutrons, one would expect to find Q=0. In this mass range extensive calculations, incorporating various *sd*-shell configurations have been performed and comparisons made with predictions of the rotational model [61–64]. On the basis of the rotational model, the 1$^+$ level in ^{22}Na at 583 keV excitation energy has been identified as the first member

Table 4.3: Ground state quadrupole moments and deformations in Na isotopes.

Isotopes	J	$T_{1/2}$	Q(exp.)[a] (barns)	Q_0(exp.)[b] (barns)	Q_0(theor.)[c] (barns)	δ[d]
^{20}Na	2^+	0.446 s				
^{21}Na	$3/2^+$	22.47 s	+ 0.050(37)	+ 0.25(19)		+ 0.24(18)
^{22}Na	3^+	2.6 y			+ 0.53	+ 0.46
^{23}Na	$3/2^+$	stable	+ 0.1006(20)	+ 0.503(10)	+ 0.52	+ 0.43(1)
^{24}Na	3^+	15.02 h				
^{25}Na	$5/2^+$	60 s	- 0.095(50)	- 0.27(4)		- 0.28(15)
^{26}Na	3^+	1.07 s	- 0.079(54)	- 0.19(13)		- 0.19(13)
^{27}Na	$5/2^+$	0.30 s	- 0.058(54)	- 0.16(15)		- 0.15(14)
^{28}Na	1^+	30.5 ms	- 0.017(37)	- 0.17(37)		- 0.16(34)
^{29}Na	$3/2^+$	43 ms	+ 0.025(54)	+ 0.13(27)		+ 0.20(22)

[a] Taken from ref. [74].
[b] Calculated from eq. (4.4).
[c] Taken from ref. [61].
[d] Calculated from eq. (4.5) using Q_0(exp.), otherwise from Q_0(theor.) if former not available.

of the K=0, T=0 band [61,72]. From measured B(E2) values Warburton et al. [72] derive an intrinsic quadrupole moment for this band of Q_0=0.6 *b*, which would imply a spectroscopic quadrupole moment Q=0.06 *b* for the 1^+ state.

Carchidi and Wildenthal [61] have performed shell model calculations which use the full set of configurations for nuclei in the A=18–38 mass region. For the 583 keV 1^+ state in ^{22}Na they calculate an intrinsic quadrupole moment $|Q_0|$=0.532 *b*. On the other hand more recent calculations by Kabir and Buck [73], and by Booten [62] report values of Q=–1.25 *b* and –1.78 *b*, respectively.

Table 4.3 summarizes the data available to date on the measured spectroscopic

quadrupole moments (Q) for ground states of the sodium isotopes [74]. The corresponding intrinsic moments Q_0 have been calculated using the relationship [61]

$$Q = Q_0 J(2J-1)/(J+1)(2J+3), \tag{4.4}$$

with K=J. The corresponding deformations δ were derived from eq. (7b) of ref. [61], viz.

$$Q_0 = (4/5)Zer_0^2 A^{2/3}\delta(1+8\delta/21), \tag{4.5}$$

with r_0=1.19 fm and Q_0 in units of e fm^2. The sixth column of table 4.3 indicates, where available, theoretical calculations of Q_0.

It is clear from the table that there are significant deformations, but of different signs and with large uncertainties. Consequently it is difficult to assert a definitive trend in the systematics of deformations in this mass region. Indeed, Vermeer [75] has suggested the possibility of shape isomerism in ^{22}Na. It is possible, for example, that the ground state of ^{22}Na could have a large positive deformation, while the 1^+ state has no deformation, or one of opposite sign. In view of the reasonable agreement with theoretical estimates [61,62], we have assumed here that the quadrupole moment as inferred from the data of Warburton et al. is correct.

From our data we estimate a minimum detectable quadrupole frequency ν_Q=1.25 MHz, based on the criterion that a deviation of $R(t)$ at t=600 ns by more than three standard deviations from $R(0)$ should be detectable. This leads to the conclusion that $|QV_{zz}| < 5.2(5) \times 10^{19}$ bV/m^2, or a quadrupole coupling interaction energy $|e^2qQ| < 5.2(5) \times 10^{-9}$ eV.

It is interesting to compare the situation for sodium with that of another alkali atom, cesium, for which quadrupole constants have been determined in graphite for the ground (J^π=$7/2^+$) and 81 keV first excited state (J^π=$5/2^+$) of ^{133}Cs. The NMR data of Carver [76] yield a value $|e^2qQ|$=4.88(33)$\times 10^{-9}$ eV for the ground state, while from Mössbauer

measurements Campbell et al. [77] report e^2qQ=4.29(5)$\times 10^{-7}$ eV for the 81 keV level. Cambell et al. were also able to determine the sign and magnitude of the quadrupole moment, with Q=–0.22(5) b, resulting in a field gradient at the site of the Cs nucleus of V_{zz}=–1.95(5)$\times 10^{22}$ V/m^2. On the basis of the ratio (24:1) of the Sternheimer (1-γ_∞) shielding factors for Cs and Na [78], one might then expect V_{zz} at the sodium nucleus to be in the region of 8×10^{20} V/m^2. A question also arises as to the nature of the sites occupied by Na in graphite. Kastelein et al. have pointed out that residence sites between the graphite layers should have field gradients an order of magnitude less than those at positions within the layers [65,79].

With the accepted value of Q_0=0.06 b for the K=0, T=0 band as obtained from B(E2) measurements in ^{22}Na [72] and supported by shell model calculations [61,62], then Q=0.06 b for the 583 keV state and consequently we find $|V_{zz}| < 8.7(8) \times 10^{20}$ V/m^2[22]. It appears then that our measurement is just above the detection limit for the quadrupole interaction in this case.

4.6 Conclusions.

Electric field gradients at the site of ^{19}F implanted into HOPG and VC have been measured by using the ^{19}F$(p,p')^{19}$F* and ^{19}F$(\alpha,\alpha')^{19}$F* reactions. Consistent results were obtained from both reactions for the HOPG host, with average values $|V_{zz}|$=3.24(14) b and η=0.16(3). For the VC sample two static efg interactions were found with fractional occupations of 60% and 40%.

The efgs determined from TDPAD measurements have been compared with cluster model calculations using HF and DFT formalisms. The residence site of F in HOPG is consistent with efg calculations at a location (b_2) midway between the graphite layers with point group symmetry C_{2h}. Better agreement was obtained with the experimental

results using DFT calculations.

In view of the simple frequency spectrum obtained in the TDPAD results, HOPG offers the possibility of a relatively clean system in which to investigate quadrupole interactions. The large efgs attainable make it a suitable medium in which to measure small quadrupole moments. However, a measurement of the nuclear quadrupole interaction using the ^{19}F(α,n)^{22}Na* reaction to implant ^{22}Na* into HOPG was not able to detect a quadrupole moment for the 583 keV 1^+ state of ^{22}Na. Accepting the value of Q_0 as inferred from B(E2) measurements, the efg at the site of ^{22}Na in HOPG was found to be less than $8.7(8)\times10^{20}$ V/m^2.

Chapter 5

Residence sites of ^{19}F in silicon.

5.1 Introduction.

The addition of trace quantities of fluorine during semiconductor fabrication has been shown to produce several advantages [80–88]: it can control key parameters, such as doping efficiency; improve photovoltaic characteristics; reduce leakage currents in p–n junctions; enhance the reliability of metal oxide semiconductor (MOS) capacitors and increase the radiation and hot carrier hardness of MOS transistors. The role played by fluorine in producing these effects is still not fully understood. As a step towards an understanding of the processes involved, an identification of the residence sites occupied by F atoms in semiconductors is clearly desirable.

The technique of time-differential perturbed angular distributions (TDPAD) of γ-rays described in Chapter 3 is ideally suited to the study of F residence sites, particularly for the investigation of quadrupole interactions. Such measurements are not possible with the Mössbauer technique on ^{19}F, and since the ground state has spin 1/2, neither are measurements using nuclear quadrupole resonance.

A principal drawback with TDPAD measurements until recently has been the problem of relating the measured quadrupole interaction parameters to the structure of the system under study, a difficulty arising from the complexity in making reliable calculations of the electric field gradient (efg) at the site of the probe. In their comprehensive TDPAD investigation of fluorine implantation in amorphous and crystalline silicon [89],

Bonde Nielsen et al. pointed out that detailed calculations of field gradients were required in order to confirm speculations regarding the nature of the occupied sites. In recent years the rapid expansion of computing power, coupled with the development of new techniques and codes for *ab initio* quantum chemical calculations, has provided the possibility of performing efg calculations which take into account the hybridization of all electronic orbitals, even in fairly complex systems. Using an Unrestricted Hartree-Fock procedure as described in section 2.4, Sulaiman et al. [90] performed such calculations to investigate fluorine sites in silicon. Although their calculated frequencies were in satisfactory agreement with the data of Bonde Nielsen et al., a disagreement was apparent as to the nature of the sites ascribed to the two interactions.

The application of Density Functional Theory (see Chapter 2.4) to problems in solid state physics and chemistry has grown rapidly over the past few years [8]. It has been pointed out, however, that in calculations involving many electron systems the relative success of the HF and DFT approaches may depend upon which property is being measured [8]. A comparison of the efficacy of HF and DFT formalisms in the area of quadrupole interaction studies is therefore of great interest.

Using a cluster model, we have employed both Restricted Hartree-Fock (RHF) and Unrestricted Hartree-Fock (UHF) procedures for comparison with DFT calculations at the site of the fluorine impurity atom in silicon. These calculations have been compared with TDPAD measurements in which ^{19}F was used as the probe.

An additional point of interest devolves on the procedure by which dangling bonds are saturated. Typically H atoms are used to satisfy bonds on peripheral atoms of the cluster [91]. As a means of simplifying the calculations, we have investigated the effect of reducing cluster size by incorporating as saturators neighbouring atoms in the periodic table.

5.2 Experimental Details

Details of the experimental arrangement for the TDPAD measurements have been given in Chapter 3. The 7MV accelerator at IRMM was set in the same mode as described in the previous chapter (see section 4.2). The probe used for the quadrupole interaction studies was ^{19}F, recoil-implanted into the system under study via the $^{19}F(p,p')^{19}F^*$ reaction by allowing a 2 ns wide pulsed beam of 2.02 MeV protons with repetition period of 1600 ns to impinge on a layer (30 $\mu g/cm^2$) of CaF_2 evaporated onto the sample surface. The implanted $^{19}F^*$ nuclei produced in the isomeric state ($I^\pi=5/2^+$, $T_{1/2}$=88.5 ns) at 197 keV excitation energy are strongly aligned, and it is the interaction of the quadrupole moment of this isomeric state with the local efg that gives rise to the perturbed angular distribution for the 197 keV γ-rays. The conventional fast-slow coincidence circuitry, described in Chapter 3, was used to record simultaneously the delayed time spectra at 0° and 90° to the incident beam in order to obtain the ratio function $R(t)$ of eqn. (3.1).

The silicon samples, $\langle 111 \rangle$ crystalline wafers with thickness 0.5 mm, were oriented at 45° to the incident beam direction (see fig. 2.2).

5.3 Analysis

As discussed in Chapter 2, the angular distribution function is given by eqn. (2.15), with perturbation factor (eqn. 2.18)

$$G_{k_1k_2}^{N_1N_2}(t) = \sum_{p=0}^{3} S_{k_1k_2p}^{N_1N_2}(\eta) \exp(-\frac{1}{2}\omega_p^2\sigma^2) \exp(-\frac{1}{2}\omega_p^2\delta^2t^2) \cos(\omega_p t). \qquad (5.1)$$

Here $\eta=(V_{xx} - V_{yy})/V_{zz}$ is the asymmetry parameter, $\omega_p=g_p(\eta)\omega_0$ are the intraband transition frequencies and σ, δ are Gaussian widths accounting for the finite resolving time and width of the efg interaction, respectively.

As before the ratio function

$$R(t) = \frac{N(0°,t) - N(90°,t)}{0.5N(0°,t) + N(90°,t)}$$

was determined experimentally and fitted according to eqn. (2.29).

In the analysis of the experimental data, first the Fourier power transforms of the ratio spectra were taken to determine the number of interactions and the frequencies ω_p associated with each efg. The initial value of the asymmetry parameter η was determined from the ratio of ω_2/ω_1. Although each interaction comprises a triplet of frequencies for spin I=5/2, the highest frequency is not always observable owing to the exponential damping factors in eqn. (5.1). Nevertheless the ratios ω_2/ω_1 are sufficient to determine η (Chapter 2, eqn. 2.14), hence the quadrupole frequency $\nu_Q=eQV_{zz}/h$ and $\omega_0=3\pi\nu_Q/10$. Fits to $R(t)$ were then generated using these values of η and ω_0 as initial estimates. The value of Q=0.072(4) b [40] was used to calculate $|V_{zz}|$, the principal component of the efg.

5.4 The efg calculations in crystalline silicon.

Using the G–92 code the efg at possible F impurity sites in the host matrix of Si was calculated by adopting a cluster model. An attempt was made to reproduce the measured values of $|V_{zz}|$ and η by specifying a relatively small group of atoms surrounding the ^{19}F probe. In some cases dangling bonds were completed with H-atoms, but for comparison other neighbouring atoms in the same row (Na, Mg) in the periodic table were used as a means of reducing cluster size and hence the complexity of the calculations. By using neighbouring atoms of comparable atomic radius to satisfy the dangling bonds, it was hoped that in an attempt to simulate the environment of an infinitely large crystal lattice, the overlap of the $3s$–wave functions on terminating Na and Mg atoms would be more realistic that the $1s$–wave functions of H atoms.

Both the HF and DFT self-consistent methods described in Chapter 2 were employed in the efg calculations [92,93]. Our DFT calculations involved the same procedure as explained in Chapter 4.4, incorporating the exchange functional of Becke and the correlation functional of Lee et al.

The atomic basis sets used were Slater type orbitals (STO) approximated by a sum of several gaussian functions. As mentioned in Chapter 2 these are conventionally designated by labels such as STO-nG*, where n gaussians are used to fit the Slater type orbital and the single asterisk indicates that polarization of the basis set is achieved with the addition of d functions to heavy atoms, while a double asterisk adds also a set of p functions to the hydrogen atoms. Split valence basis sets extended at double zeta level are specified by terms such as STOl-mnG, or simply l-mnG, where l,m,n indicate the number of gaussian functions fitting the core, inner and outer valence orbitals respectively.

5.5 Results and Discussion

In so far as the efg calculations are concerned, the quantities of interest derived from the fits to the $R(t)$ data are the principal component of the efg, $|V_{zz}|$, and the asymmetry parameter, η. The approach then is to postulate possible residence sites for ^{19}F and to compare the results of the HF and DFT calculations with measured $|V_{zz}|$ and η.

Figures 5.1.a and 5.1.b show the $R(t)$ data with the theoretical fit (solid line) and the Fourier power transform, respectively, for ^{19}F* implantation in Si. Readily identifiable components of frequency triplets are indicated in the Fourier spectrum, where ν_{ij} denotes the jth component of interaction i. The results of the fit, including previous measurements of Bonde Nielsen et al. [89], are summarized in table 5.1. While both sets of measurements report within good agreement the existence of two axially symmetric static interactions with quadrupole frequencies close to 23 MHz and 35 MHz, we see also

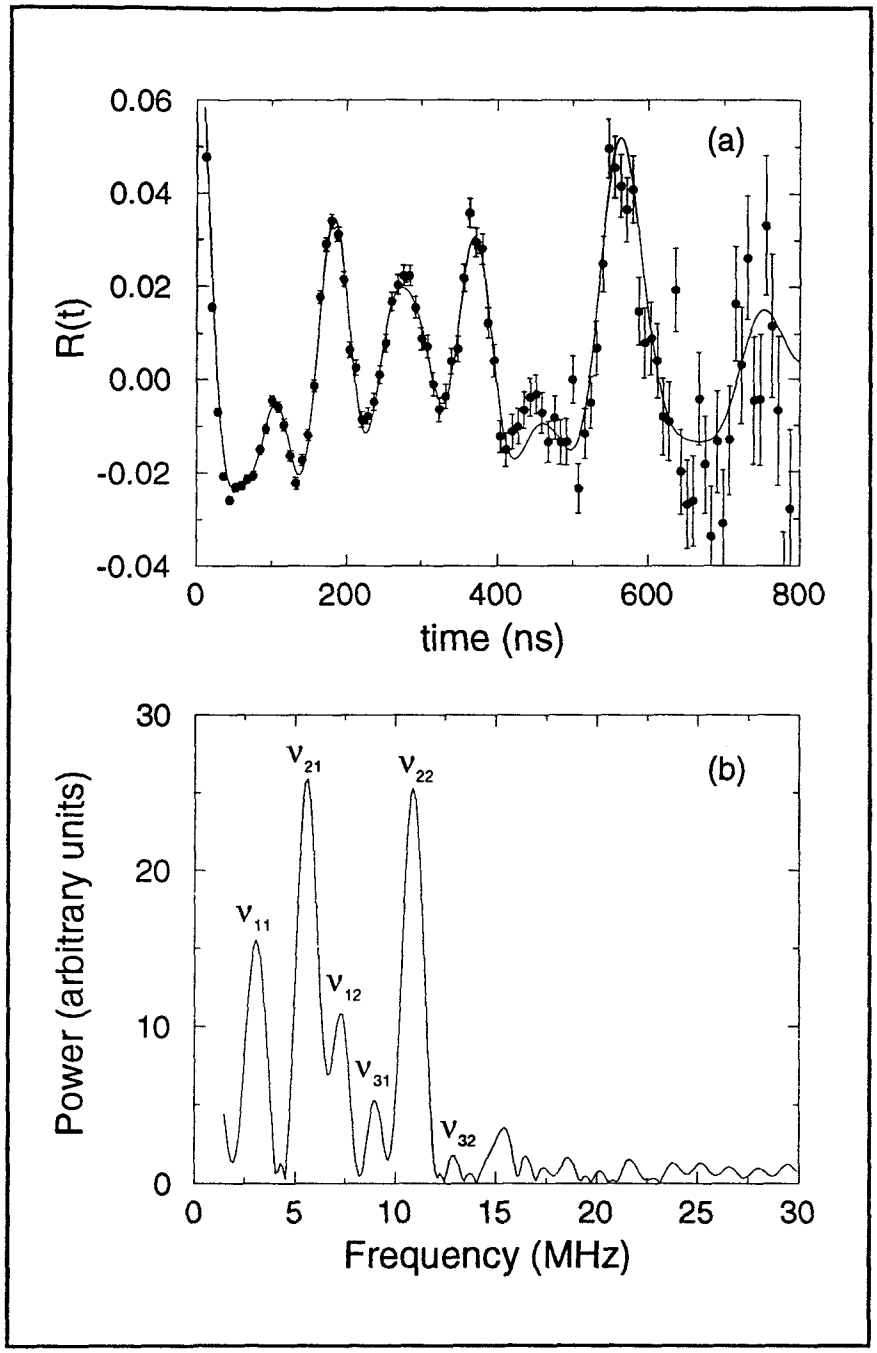

Figure 5.1: (a) The ratio spectrum R(t) of $^{19}F^*$ implanted into silicon and (b) its Fourier power spectrum.

Table 5.1: Best fit parameters to $R(t)$ (solid line in fig. 5.1a) for implantation of $^{19}F^*$ in crystalline Si.

Interaction		Fraction (%)	ν_Q (MHz)	$\lvert V_{zz}\rvert$ (10^{22} V/m^2)	η	δ (%)
#1	(a)	31(2)	23.2(3)	1.33(8)	0.05(5)	5(1)
	(b)	18(3)	23.0(3)		0	0
#2	(a)	60(3)	35.2(3)	2.02(11)	0.00(5)	4(1)
	(b)	40(5)	34.7(3)		0	0
#3	(a)	9(3)	37.1(5)	2.13(13)	0.80(7)	5(1)

(a) This work; (b) Reference [89].

evidence for a third static interaction close to 37 MHz.

On the basis of the ⟨111⟩ axial symmetry of the 35 MHz interaction, Bonde Nielsen et al. postulated that in this site the fluorine must occupy a position in either bond or antibond direction of the Si lattice; further considerations, including channeling studies of deuterium impurities in silicon [94], caused them to favour the antibond direction. It was suggested that the 23 MHz interaction, which they observed in both amorphous and crystalline silicon, might be associated with a defect that involves substitutional fluorine in a distorted site. In their calculations Sulaiman et al. [90] considered clusters of $FSi_{11}H_{18}$ and FSi_8H_{18} for F at antibonding (AB) and intrabond (IB) sites, respectively. The resulting quadrupole frequencies were calculated to be ν_Q^{AB}=25.25 MHz and ν_Q^{IB}=35.7 MHz, the latter assignment thus in disagreement with the conclusion of Bonde Nielsen et al.

In our approach the cluster configurations considered for implanted fluorine are illustrated in figs. 5.2 and 5.3 for an interstitial bond-centre site (BC) and antibonding

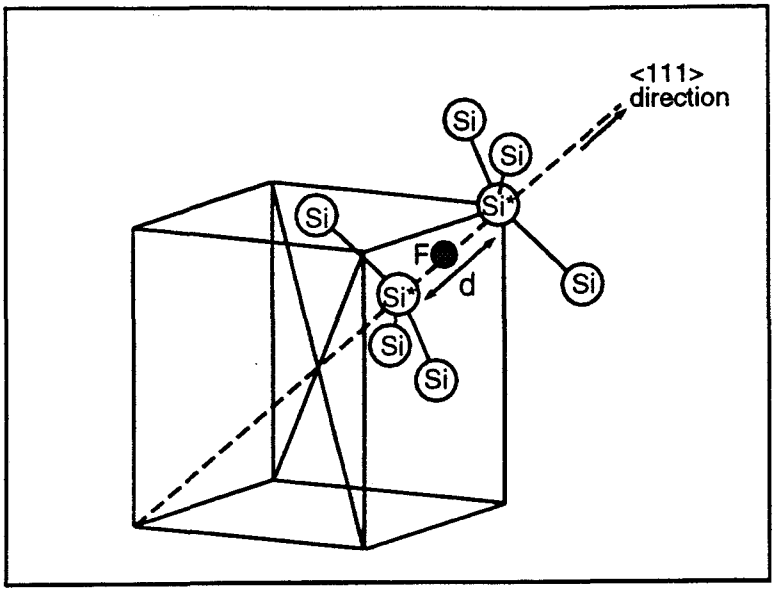

Figure 5.2: The FSi_8H_{18} cluster geometry for the interstitial bond-centre site. The hydrogen atoms are not shown.

Table 5.2 Results of efg calculations at an interstitial F bond-centre (BC) site in the cluster FSi_8H_{18} (see fig. 5.2 above) using Unrestricted Hartree-Fock (UHF) and Density Functional Theory (DFT) methods.

METHOD	BASIS	V_{zz}^{BC} (10^{22} V/m^{22})	η
UHF	STO-3G*	- 2.341	0
UHF	3-21G	- 2.002	0
UHF	6-31G	- 2.007	0
DFT	STO-3G*	-2.231	0
This measurement (Table 5.1, interaction #2)		$\|V_{zz}\| = 2.02(11)$ ν_Q=35.2(3) MHz	0

(AB) site, respectively. Figure 5.4 shows a schematic representation of these sites in the {110} plane of the Si diamond lattice structure. The cross-hatched circles correspond to Si atoms in the {110} plane and the open circles to Si atoms in planes directly above or below the plane of the paper. All the calculations were performed for clusters with neutral charge.

In the symmetric FSi_8H_{18} cluster of fig. 5.2 the fluorine atom is located centrally between two silicon atoms (labelled Si* in the figure). The Si*–Si* bond length was allowed to relax while the total energy was minimized, resulting in an expansion of the bond length from the Si lattice value of 2.3513 Å to 3.3758 Å, i.e. an F–Si* distance of 1.688 Å. The dangling bonds on the remaining six Si atoms are satisfied by H atoms. The calculations depend on the basis set used and are shown in Table 5.2 for both HF and DFT methods. The results of the bond-centre calculations listed in Table 5.2 yield an average value $\left\langle V_{zz}^{BC} \right\rangle = -2.15 \times 10^{22}$ V/m^2 for the efg at the bond-centre site, corresponding to ν_Q^{BC}=37.5 MHz, thus supporting the choice for this site as the origin of the 35.2 MHz interaction in Table 5.1. Closest agreement with experiment was obtained using the split valence basis sets 3-21G and 6-31G with the HF formalism, which yielded quadrupole frequencies of 34.9 MHz and 35.0 MHz, respectively. Intrabond and bond-centre sites have been proposed by other authors for a variety of impurities in diamond structures. Using extended Hückel theory, Singh et al. [95] have predicted an intrabond site for H impurities in silicon in the absence of defects. Calculations by Verwoerd [96] indicate that the bond-centre site is the most energetically favoured for F implantation in diamond.

In the antibonding configuration for the cluster $FSi_{10}H_{15}$ shown in fig. 5.3, the fluorine is situated along the ⟨111⟩ antibonding direction from a silicon atom, while all dangling bonds are terminated with H atoms. In order to investigate the effects of dangling bonds, we also performed calculations for the smaller 14–atom cluster $FSi_4Mg_6Na_3$, where in fig.

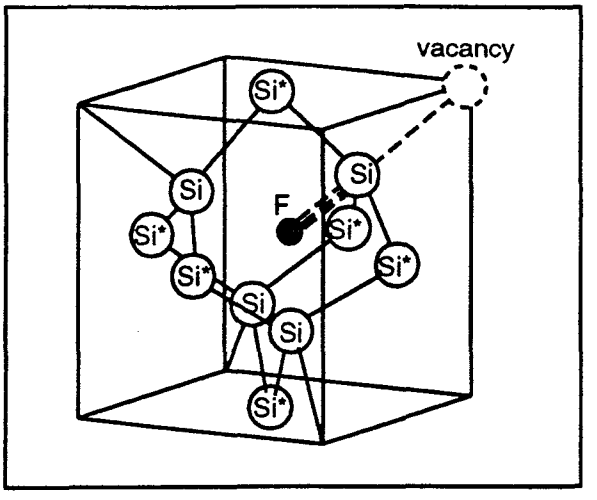

Figure 5.3: The $FSi_{10}H_{15}$ cluster geometry for the interstitial antibonding site; all dangling bonds are satisfied with H atoms (not shown in the figure). For the $FSi_4Mg_6Na_3$ cluster the Si* atoms are replaced by Mg and remaining dangling single bonds terminated with Na atoms.

Table 5.3: Results of efg calculations at an interstitial F antibonding (AB) site in the clusters $FSi_{10}H_{15}$(I) and $FSi_4Mg_6Na_3$ (II) using Restricted Hartree-Fock (RHF) and Density Functional Theory (DFT) methods.

METHOD	BASIS	V_{zz} (10^{22} V/m^2)		η
		I	II	
RHF	STO-3G*	- 1.737	- 1.366	0
RHF	3-21G	- 1.492	- 1.513	0
RHF	6-31G	- 1.344	- 1.382	0
DFT	STO-3G*	- 1.458	- 1.195	0
DFT	3-21G	- 1.231	- 1.016	0
This measurement (Table 5.1, interaction #1)		$\lvert V_{zz}\rvert = 1.33(8)$ $\nu_Q = 23.2(3)$ MHz		0

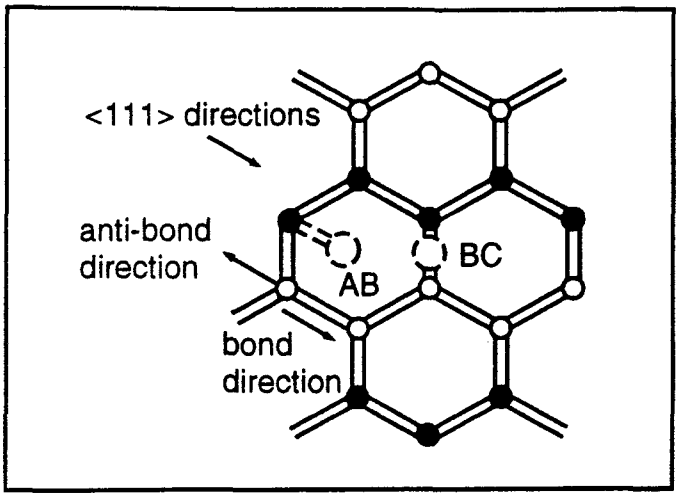

Figure 5.4: View of the {110} plane of silicon showing tetrahedral bonds of the typical diamond structure. The cross-hatched circles correspond to Si atoms in a {110} plane and the open circles to Si atoms above or below the plane of the paper. The labels AB and BC refer to interstitial antibonding and bond-centre sites, respectively.

5.3 the peripheral face-centred atoms (Si*) are replaced by Mg atoms to satisfy double bonds and remaining single bonds are completed with Na atoms. The calculations in this case yield average values $\left\langle V_{zz}^{AB} \right\rangle = -1.45 \times 10^{22}$ V/m^2 (ν_Q^{AB}=25.3 MHz) and -1.29×10^{22} V/m^2 (ν_Q^{AB}=22.5 MHz) for the $FSi_{10}H_{15}$ and $FSi_4Mg_6Na_3$ clusters shown in columns I and II of Table 5.3 respectively, in reasonable agreement with the measured value $|V_{zz}|$=1.33(10)$\times 10^{22}$ V/m^2 (ν_Q=23.2 MHz) obtained for the lowest frequency interaction in Table 3. In this case the HF 6-31G basis set gave closest agreement with experiment, yielding $V_{zz}^{AB} = -1.344 \times 10^{22}$ V/m^2 (ν_Q^{AB}=23.4 MHz).

Column II of Table 5.3 indicates that the efg calculations are still in reasonable agreement when dangling bonds are completed with Na and Mg atoms. This is probably an indication that the efg is dominated by contributions from the internal electronic system of fluorine and its bonding to nearest neighbours. The highly localized nature

of the efg may also explain why this interaction is also observed in amorphous silicon, where amorphisation can be viewed as a structure of overlapping distorted micro-regions, as suggested by Bonde Nielsen et al. [89].

The F position along the ⟨111⟩ antibonding direction was again determined by minimizing the total energy. For the $FSi_{10}H_{15}$ cluster it was situated at 1.81 Å from the Si atom; for the case of the $FSi_4Mg_6Na_3$ cluster this distance was 1.71 Å. Similar antibonding sites in silicon have been ascribed to deuterium [94] and boron [97] impurities, as well as carbon [98] and aluminum [96] pair structures.

Regarding interaction #3 in Table 5.1, the evidence for its presence is not strong. However, it appears in the Fourier power transform, and the fit is improved with its addition. Although $|V_{zz}|$ is comparable in magnitude with interaction #2, the third interaction is characterized by a large asymmetry (η=0.80). The bonding (Table 5.2) and antibonding (Table 5.3) cases both predict a vanishing η, so we speculate that this interaction may arise from a site, or group of sites, associated with a defect, or some other impurity centre such as hydrogen.

5.6 Conclusions

The efgs determined from TDPAD measurements following implantation of ^{19}F in crystalline silicon have been compared with cluster model calculations using HF and DFT formalisms. Three quadrupole interactions were detected. One of these (ν_Q=35.2 MHz) is in agreement with the predicted efg for an interstitial bond-centre site, while the second (ν_Q=23.2 MHz) corresponds to the predictions for an antibonding site located at 1.81 Å along a ⟨111⟩ direction from a silicon atom.

Theoretical calculations of efgs using both HF and DFT methods yield comparable

results. The completion of dangling bonds with atoms other than hydrogen was investigated. For the case studied relatively good agreement was obtained using Na and Mg as saturating atoms. Such an approach may prove useful in minimizing the complexity of cluster model calculations.

Chapter 6

NQI of ^{19}F implanted in germanium and gallium arsenide.

6.1 Introduction.

In recent years the study of semiconductor materials using nuclear techniques has witnessed a rapid growth [100]. In particular, the techniques of time-differential perturbed angular correlations (TDPAC) or distributions (TDPAD) of γ-rays have been extensively employed.

As mentioned in the previous chapter, the improvement of device characteristics obtained by the addition of fluorine in the semiconductor fabrication process has stimulated many investigations into the role played by fluorine in device operation. Nevertheless, detailed information regarding the residence sites of F in semiconductors is still lacking.

In Chapter 5 we reported the results of TDPAD investigations following the implantation of ^{19}F at silicon and the possible residence sites of the fluorine atoms based on the theoretical calculation of efgs at various sites in the crystalline matrix. Here we continue the work using other semiconductor materials, i.e. germanium and gallium arsenide. Since these elements are heavier and have more electrons than silicon one may expect more complicated efg calculations than those for the case of silicon.

In a previous study of ^{19}F in Ge [101], Bonde Nielsen et al. emphasized the need for quantitative calculations in order to establish the nature of the sites occupied by fluorine. We have performed such calculations here, using both Hartree-Fock (HF) and Density Functional Theory (DFT) formalisms. To our knowledge, no quadrupole interaction

studies have previously been reported for ^{19}F implantation in GaAs using the TDPAD technique.

6.2 Experimental details.

The 7 MeV Van de Graaff at IRMM was operated in the same mode as the previous measurements, i.e. beam energy E=2.02 MeV, width of the pulse ΔT=2 ns and repetition period T=1600 ns. The proton beam was directed to impinge at 45° on to targets of $\langle 111 \rangle$ germanium and gallium arsenide coated with a 30 μg/cm^2 layer of CaF_2. Recoiling ^{19}F nuclei in the isomeric state ($I^\pi=5/2^+$, $T_{1/2}$=88.5 ns) at 197 keV excitation energy were produced via the $^{19}F(p,p')^{19}F^*$ reaction and implanted into the samples.

Details of the apparatus and TDPAD measurements have been reported in previous chapters. Detectors at 0° and 90° to the beam direction recorded the delayed time spectra of the γ–rays to give the experimental ratio of eqn. (3.1). In order to minimize systematic errors the 0° and 90° detectors were frequently interchanged. To check reproducibility several runs, each typically 2-3 hours in length, were recorded for inter-comparison. In the final $R(t)$ spectrum presented here 8 such individual runs were combined to obtain reasonable statistics.

6.3 Analysis of the data.

6.3.1 Analysis of the experimental ratio functions.

The methodology described in Chapter 5 was applied in similar manner to the analysis of the Ge and GaAs data. The $R(t)$ data and associated Fourier power transform for the Ge sample are shown in fig. 6.1. For the GaAs sample the signal of interest is superimposed upon an exponential background (fig. 6.2). The solid line in fig. 6.2 was

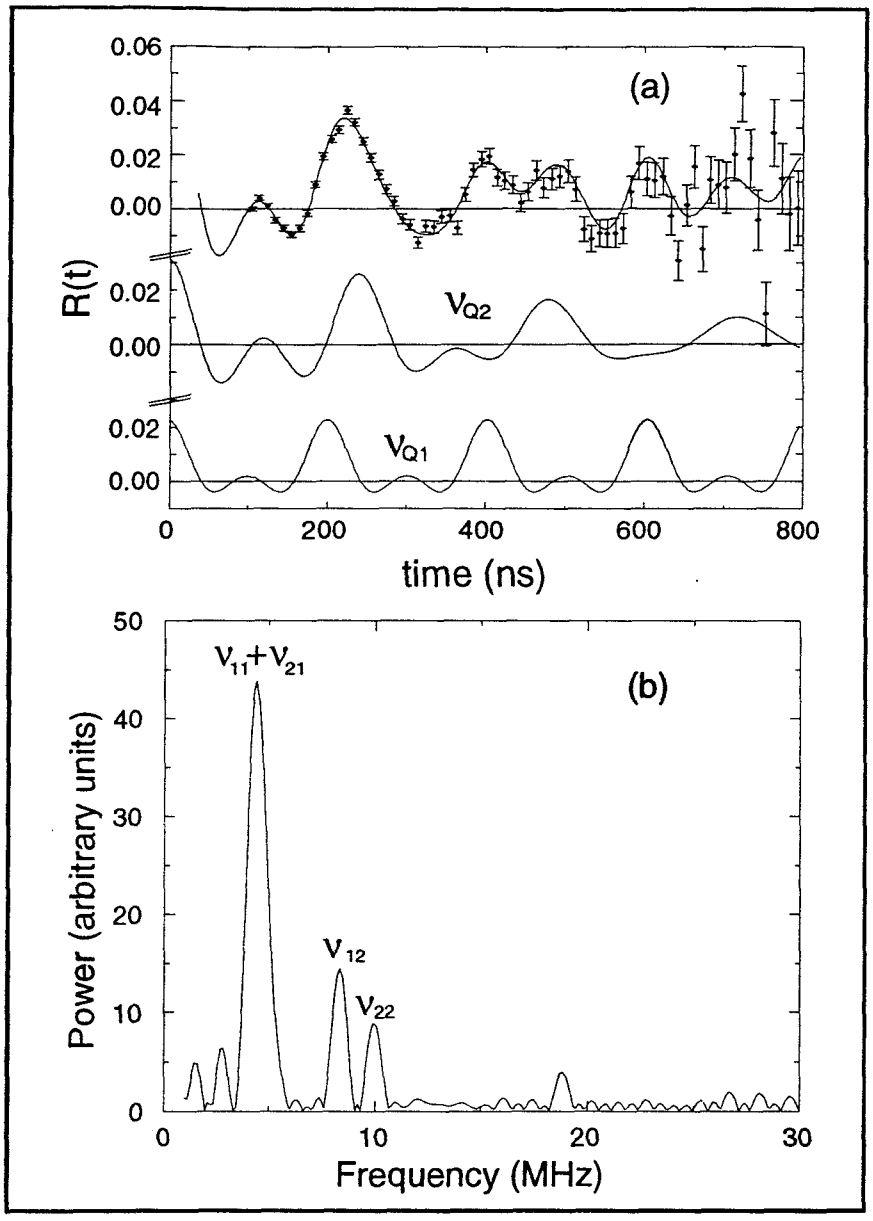

Figure 6.1: (a) The ratio spectrum R(t) for $^{19}F^*$ implantation in Ge. The solid line (upper part) is a theoretical fit using two interactions with quadrupole frequencies ν_{Q2} and ν_{Q1} shown in the figure. (b) The corresponding Fourier power transform of the experimental R(t).

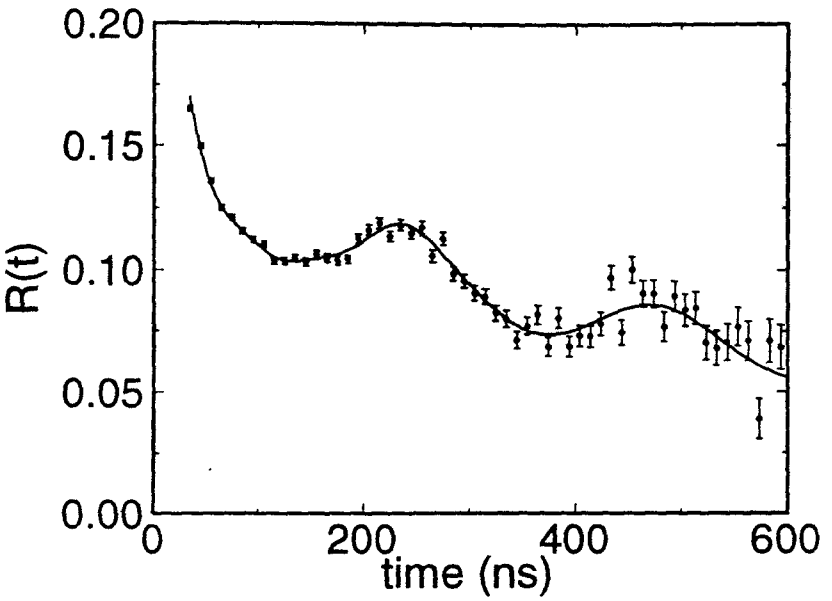

Figure 6.2: The ratio function $R(t)$ for $^{19}F^{*}$ implantation in GaAs. The solid line is the theoretical fit using eqn. (6.1).

obtained from a fit to the function

$$R'(t) = f_e e^{-\alpha t} + f_r R_{\text{theor}}(t), \tag{6.1}$$

where α is treated as a free parameter, $f_e+f_r=1$ and $R_{\text{theor}}(t)$ is the ratio function of eqn. (2.27).

Possible static quadrupole interactions were identified once more from the frequencies ν_{ij} observed in the Fourier power spectra, where j designates one of the three components of interaction i. The same procedure, using frequency ratios obtained from the Fourier spectra, was used to derive initial estimates of η and ω_0, following which fits to $R(t)$ were generated yielding values of $|V_{zz}|$ and η for comparison with the theoretical calculations.

6.3.2 Strategy for the efg calculations.

A cluster model was used to calculate the efg at the site of ^{19}F in host matrices of Ge and GaAs. Using the G–92 computer code, both HF and DFT formalisms were again employed to calculate V_{zz} and η for the ^{19}F probe in specific configurations, with dangling bonds terminated by H-atoms [91]. The atomic basis sets used were STO-3G*, i.e. Slater type orbitals approximated by a sum of 3 gaussians, where the asterisk indicates that *d* functions have been added to the the heavy atoms. Double zeta basis sets in G–92 are not available beyond Z=17 (Cl).

As in the calculations for Si the DFT calculations incorporated the local spin density exchange functional of Becke, together with the correlation functional of Lee et al.

6.4 Results and Discussion.

6.4.1 Implantation of ^{19}F in Ge.

Table 6.1 summarizes the results of the fit to $R(t)$ for ^{19}F implantation in Ge. Two static quadrupole interactions with η equal to or close to zero were observed with frequencies ν_{Q1}=27.5(3) MHz and ν_{Q2}=33.0(4) MHz, in good agreement with the values of 27.3(4) MHz and 33.4(4) MHz reported by Bonde Nielsen et al. [101]. The latter, however, report population fractions which differ significantly from ours, and for the 33 MHz interaction they refer the symmetry to a major principal axis with high index, or associate it possibly with a polycrystalline region of low symmetry. Our quadrupole frequencies ν_{Q1} and ν_{Q2} correspond to field gradients $|V_{zz}|$=1.58(6) $\times 10^{22}$ V/m^2 and 1.90(7)$\times 10^{22}$ V/m^2, respectively. The contributions from each interaction are shown in fig. 6.1.

Following the good agreement obtained with experiment for the cluster model calculations at ^{19}F in silicon (see Chapter 5), and based on the strong similarity of the data from Si and Ge structures [10,90,101], the efg calculations were performed for F situated

Table 6.1: Results of the fit to $R(t)$ for $^{19}F^*$ implantation in Ge.

Interaction		Fraction (%)	ν_Q (MHz)	η	δ (%)
#1	(a)	58	27.5(3)	0.09(8)	6(1)
	(b)	21	27.3(4)	–	–
#2	(a)	42	33.0(4)	0.00(8)	0(1)
	(b)	26	33.4(4)	–	–

(a) This experiment.
(b) Reference [101]. Note that the fractional populations are based on fig. 2, where T=293°. The residual population (53%) is presumably taken up by F recoils that remain in the surface layers, although the authors do not make this clear.

at sites along ⟨111⟩ directions in the Ge lattice. Figure 6.3 illustrates the cluster configurations for ^{19}F at a bond-centre (BC) and antibonding (AB) site. All the calculations were made for clusters with neutral charge. The results of the calculations for both BC and AB sites are shown in table 6.2, together with the charge q_F on the fluorine atom obtained from the Mulliken charge distribution.

Dangling bonds on the peripheral Ge atoms of Fig. 6.3a were completed with H-atoms, resulting in a 27–atom cluster, FGe_8H_{18}. With F centrally located between two Ge atoms, the bond length d was allowed to vary until the total energy was minimized, resulting in an expansion from the lattice value of 2.4465 Å to 3.4305 Å.

In the antibonding case the cluster considered was $FGe_{10}H_{15}$ (fig. 6.3b), with the fluorine atom situated along the ⟨111⟩ antibonding direction at a distance λ from a germanium atom. The length λ was treated as a free parameter in the energy minimization, resulting in a best fit value for λ of 1.8796 Å.

As can be seen from table 6.2, both HF and DFT formalisms generate $|V_{zz}|$ values that

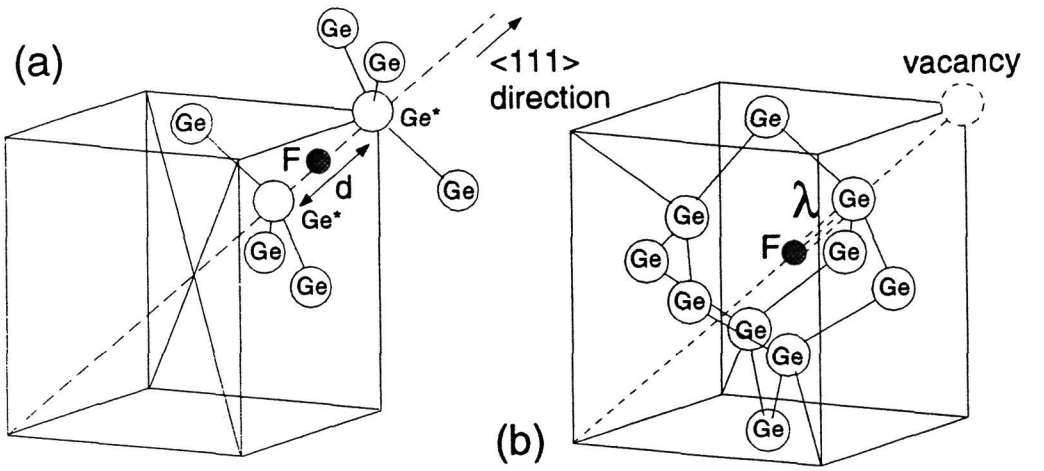

Figure 6.3: (a) The bond-centre cluster of FGe_8H_{18}. The ^{19}F atom is situated at the bond-centre site of Ge*–Ge* atoms in the ⟨111⟩ direction. (b) The antibonding cluster of $FGe_{10}H_{15}$. The ^{19}F atom is situated along the ⟨111⟩ antibonding direction at a distance λ=1.8796 Å from a Ge atom. Only heavy atoms are shown in the figure.

Table 6.2: Results of Unrestricted Hartree-Fock (UHF), Restricted Hartree-Fock (RHF) and Density Functional Theory (DFT) calculations using STO-3G* basis functions at bond-centre (Fig. 6.3a) and antibonding (Fig. 6.3b) sites in Ge. For all cases η=0. The charge q_F on the fluorine atom obtained from the Mulliken process is given in units of e.

SITE	CLUSTER	METHOD	q_F	V_{zz} (10^{22} V/m^2)
BOND-CENTRE	FGe_8H_{18}	UHF	− 0.114	− 2.832
		DFT	+ 0.019	− 2.638
ANTIBONDING	$FGe_{10}H_{15}$	RHF	− 0.204	− 2.650
		DFT	+ 0.010	− 1.996
		UHF	− 0.204	− 2.727
THIS EXPERIMENT :		$\nu_{Q1} = 27.5(3)$;	$\lvert V_{zz}\rvert = 1.58(9)$	
		$\nu_{Q2} = 33.0(4)$;	$\lvert V_{zz}\rvert = 1.90(11)$	

are systematically higher than those obtained from experiment. It may be unrealistic to expect closer agreement with the measured values since only the minimal basis set STO-3G is available for fourth period elements in G–92. While the DFT values $|V_{zz}^{AB}|$=1.996 $\times 10^{22}$ V/m^2 and $|V_{zz}^{BC}|$=2.638 $\times 10^{22}$ V/m^2 are closer to the experimental results, both formalisms show a systematic trend, predicting $|V_{zz}|$ to be lower at the antibonding site. Referring to the DFT predictions, the calculations indicate that the efg at the antibonding site is of the order of 20% lower than that at the bond-centre position, reflecting the same trend in the experimental data. Given the comparable difference in the measured values for ν_{Q1} and ν_{Q2}, and following the results of similar calculations for ^{19}F in silicon with higher level basis sets [10], it is therefore tempting to ascribe the 33.0 MHz and 27.5 MHz interactions to the bond-centre and antibonding sites, respectively. However, it is clear that more refined calculations are needed before such a conclusion can be definite.

In a comprehensive treatment of HF theory, Sahoo et al. [102] have considered such $\langle 111 \rangle$ sites in Ge for muonium at vacancy-associated and bond-centre locations. Similar impurity sites for fluorine have been postulated in silicon [90,102,103], as well as for other impurities such as hydrogen [104], deuterium [94] and boron [97].

6.4.2 Implantation of ^{19}F in GaAs.

Figure 6.2, which shows the $R(t)$ spectrum obtained for ^{19}F implantation in GaAs, indicates a small quadrupole signal superimposed upon an exponential background, the latter possibly a result of randomly fluctuating time-dependent interactions [16]. The single quadrupole interaction, evident in the Fourier power transform of Fig. 6.3b, is better featured in fig. 6.3a, where the exponential signal has been subtracted. The quadrupole interaction frequency was found to be axially symmetric (η=0) with ν_Q=27.7(5) MHz, corresponding to $|V_{zz}|$=1.59(9)$\times 10^{22}$ V/m^2.

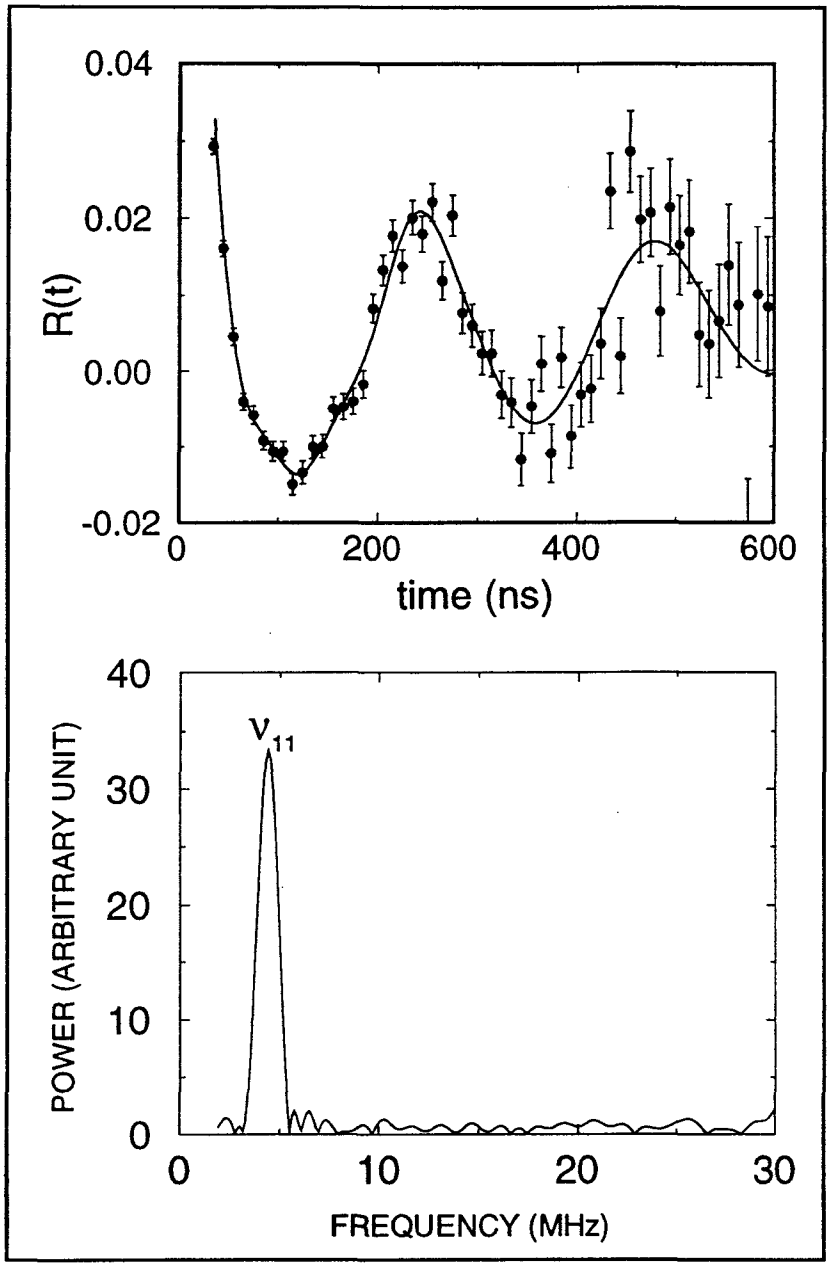

Figure 6.4: (a) The ratio spectrum R(t) for $^{19}F^*$ implantation in GaAs after subtraction of the exponential background and (b) its Fourier power spectrum.

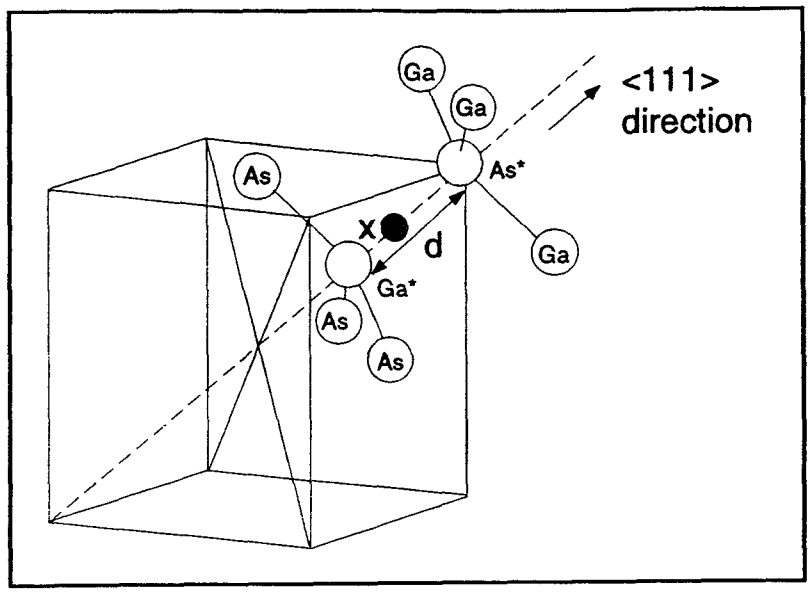

Figure 6.5: The intrabond site in the cluster $FGa_4As_4H_{18}$. The ^{19}F atom is slightly displaced towards the Ga atom. The distances of Ga*–F and F–As* are 1.3656 Å and 1.4057 Å, respectively.

Table 6.3: Results of Restricted Open Shell Hartree-Fock (ROHF) and Density Functional Theory (DFT) calculations using STO-3G* basis functions at an intrabond site in the cluster $FGa_4As_4H_{18}$ (Fig. 6.5 with d=2.771 Å and x=1.366 Å). The charge q_F on the fluorine atom obtained from the Mulliken process is given in units of e.

METHOD	q_F	V_{zz} (10^{22} V/m^2)	η
ROHF	- 0.236	- 4.449	0
DFT	- 0.019	- 1.612	0
THIS EXPERIMENT		$\lvert V_{zz}\rvert = 1.59(9)$ $\nu_Q = 27.7(5)$ MHz	0.00(7)

Since ^{19}F situated at antibonding sites with respect to Ga or As atoms would be expected to produce two distinct quadrupole interactions, we consider only the intrabond site (IB) shown in the $FGa_4As_4H_{18}$ cluster of fig. 6.5, where dangling bonds have been saturated with H-atoms. In this case the lowest energy of the system was obtained when the Ga–As bond length was increased from its lattice value of 2.4465 Å to 2.7713 Å, with the fluorine slightly displaced towards the Ga atom (x=1.3656 Å in fig. 6.5).

The results of the calculations and corresponding Mulliken charge q_F are shown in Table 6.3. They indicate a marked difference in the predictions of the HF and DFT methods, with the latter showing considerably closer agreement with experiment. The DFT calculation, yielding $|V_{zz}|=1.61\times10^{22}$ V/m^2, or ν_Q=28.0 MHz, and η=0, compares favourably with the measured values of ν_Q=27.7(5) MHz and η=0.00(7).

6.5 Conclusions.

TDPAD measurements of quadrupole interactions involving the 197 keV isomeric state of ^{19}F confirm the presence of two quadrupole frequencies in Ge and indicate only a single frequency in GaAs. The axial symmetry of the interactions points to possible residence sites for F along ⟨111⟩ bonding and antibonding directions.

In the case of GaAs, DFT calculations at an intrabond site give ν_Q=28.0 MHz and η=0, in good agreement with the measured efg corresponding to an axially symmetric interaction with quadrupole frequency ν_Q=27.7(5) MHz. From energy considerations the F atom is predicted to be at distances of 1.37 Å and 1.41 Å from the Ga and As atoms, respectively.

For the Ge host poorer agreement with theory is obtained. The DFT calculations, however, yield efg values closer to experiment than the HF results. Based on the strong similarity with F sites in Si, and on the systematic trend of both DFT and HF predictions,

it is suggested that the frequencies ν_{Q1}=27.5(3) MHz and ν_{Q2}=33.0(4) MHz correspond to F at an antibonding site 1.88 Å from a Ge atom and to a bond-centre site, respectively. More calculations with higher level basis sets are required, however, before a definite assignment can be made. With the rapid expansion in computing power and the ability to achieve complete hybridization of all electronic orbitals, the feasibility of realistic efg calculations in many electron system looks highly promising.

Chapter 7

General conclusions.

At the outset of this thesis we stated that our objectives were twofold: (i) to establish the nature of F residence sites in semiconductors; (ii) to provide an evaluation of the HF and DFT formalisms for the calculations of efgs in matter. Here we summarize our results and general conclusions.

Table 7.1 contains a summary of results for ^{19}F implantation in the hosts HOPG, silicon, germanium and gallium arsenide. The measured values of $|V_{zz}|$ and η are compared with the best predictions of HF and DFT theoretical calculations. The tabulations indicate that overall superior agreement is obtained with experiment for the DFT calculations.

For the case of HOPG a residence site (b_2) for F midway between the layers is indicated, with point group symmetry C_{2h}. The experimental values $|V_{zz}|$=3.24(14)$\times 10^{22}$ V/m^2 and η=0.16(3) are in the good agreement with the DFT results $|V_{zz}|$=3.09$\times 10^{22}$ V/m^2 and η=0.13. The HOPG material proved to be an excellent test case, both from experimental and theoretical standpoints. Although a search using the ^{19}F$(\alpha, n)^{22}$Na* reaction for the quadrupole moment of the 583 keV level in ^{22}Na produced a null result, indications are that HOPG should prove a fruitful medium for other such measurements with different isomers.

Both HF and DFT procedures provide convincing evidence for two axially symmetric F residence sites in Si at antibonding and bond-centre positions in the crystal lattice. The measured values $|V_{zz}|$=3.24(14) and 2.02(11) $\times 10^{22}$ V/m^2 compare favourably with

Table 7.1: Summary of the TDPAD measurements and the theoretical predictions using HF and DFT formalisms. The HF calculations include restricted (RHF), unrestricted (UHF) and restricted open shell (ROHF) versions.

HOST	$\lvert V_{zz}\rvert(10^{22}$ V/m$^2)$		asymmetry (η)		COMMENTS
	EXP.	THEORY	EXP.	THEORY	
HOPG	3.24(14)	3.09 (DFT) 4.27 (UHF)	0.16(3)	0.13 0.03	Site between the layers; layer spacing 3.7 Å (DFT), point group symmetry C_{2h}
Si	1.33(8)	1.23 (DFT) 1.34 (RHF)	0.05(5)	0 0	F at antibonding site, 1.81 Å from a Si Atom.
	2.02(11)	2.23 (DFT) 2.01 (UHF)	0.00(5)	0 0	Bond-centre site; 1.02 Å expansion in Si–Si bond length.
	2.13(13)	–	0.80(7)	–	Associated with defect or impurity.
Ge	1.58(9)	2.00 (DFT) 2.65 (UHF)	0.09(8)	0 0	Antibonding site; F at 1.02 Å from a Ge atom.
	1.90(11)	2.64 (DFT) 2.83 (ROHF)	0.00(8)	0 0	Bond-centre site; expansion of 1 Å in Ge–Ge bond length.
GaAs	1.59(9)	1.61 (DFT) 4.45 (ROHF)	0.00(7)	0 0	Intrabond site; F at 1.37 Å from Ga, 2.40 Å from As.

both HF and DFT predictions, the former in this case yielding $|V_{zz}|$=1.34 and 2.01 $\times 10^{22}$ V/m^2, respectively. In the antibonding site the F atom is situated 1.81 Å from a silicon atom; in the bond-centre case the Si–Si bond is increased by 1.02 Å.

A third interaction with $|V_{zz}|$=2.13(13) $\times 10^{22}$ V/m^2 and a large asymmetry parameter (η=0.80) was also identified, but only at the 10% level. This may be associated with a defect or impurity.

Our calculations for Si using Na and Mg to terminate dangling bonds showed comparable agreement with those obtained using larger clusters saturated with H-atoms. Such a stratagem may prove useful in future applications as a means of reducing cluster size.

The poorest agreement with experiment occurred for ^{19}F in Ge, where the theoretical results for $|V_{zz}|$ are consistently high. Based on the ⟨111⟩ symmetry and the systematic trend in the theoretical predictions, we ascribed the higher experimental value to the bond-centre site, the lower to the antibonding site. In the former case the Ge–Ge bond is found to expand by about 1 Å to accommodate the fluorine; in the latter F is located 1.02 Å along a ⟨111⟩ direction from a Ge atom. A need clearly exists in this case for more refined calculations extended to higher basis level sets.

The final system investigated, ^{19}F in GaAs, revealed only one static, axially symmetric efg interaction with $|V_{zz}|$=1.59(9)$\times 10^{22}$ V/m^2. In this case the DFT result, $|V_{zz}|$=1.61$\times 10^{22}$ V/m^2 and η=0, is consistent with F at an intrabond site 1.37 Å from Ga and 2.40 Å from As.

We feel that the information obtained from these experiments will prove invaluable in establishing the connection from the microscopic structure of F in semiconductors to the macroscopic behaviour exhibited in device operation. The experiments also show that TDPAD has been vindicated as a useful diagnostic tool in the field of materials science.

=====00000=====

Bibliography

[1] M. Forker and R. J. Vianden, Mag. Res. Rev., **7** (1983) 275.

[2] H. H. Rinneberg, Atomic Energy Review, **17** (1979) 477.

[3] Alberto Lopez-Garcia, Mag. Res. Rev., **15**, 119 (1990).

[4] G. R. Satchler, *Introduction to nuclear reactions*, Macmillan Education Ltd., London, 1990.

[5] Anton Lerf and Tilman Butz, Anew. Chem. Int. Ed. Engl. **26**, 110 (1987).

[6] Reiner M. Dreizler and Joao daProviducia (eds.), *Density Functional Methods in Physics*, Plenum Press, New York, 1983.

[7] Jan K. Labanwski and Jan W. Andzeln (Eds.), *Density Functional Methods in Chemistry*, Springer-Verlag, New York, 1991.

[8] Delano P. Chong, Chinese Journal of Physics, **30** (1991) 115.

[9] P. W. Martin, D. Surono, F-J. Hambsch, H. Postma and P. Rietveld, Hyp. Int. **77** (1993) 315.

[10] D. Surono, F -J. Hambsch and P. W. Martin, *Residence sites of fluorine in crystalline silicon and highly oriented pyrolytic graphite*, accepted for publication in Hyperfine Interactions, 1995.

[11] D. Surono, F-J. Hambsch and P.W. Martin, *Quadrupole Interactions of ^{19}F implanted in germanium and gallium arsenide*, submitted to The Journal of Chemical Physics, 1995.

[12] John M. Blatt and Victor F. Weisskopf, *Theoretical Nuclear Physics*, Dover Publications, Inc., New York, 1991.

[13] T. Butz, Hyp. Int. **52** (1989) 189.

[14] L. C. Biedenharn and M. E. Rose, Rev. of Mod. Phys. **25** (1953) 729.

[15] K. Alder, A. Bohr, T. Huus, B. Mottelson and A. Winther, Rev. of Mod. Phys. **28** (1956) 432.

[16] H. Frauenfelder and R. M. Steffen in *Alpha-, Beta- and Gamma-ray Spectroscopy*, Vol. 2, K. Siegbahn (Ed.), North Holland Publishing Co., Amsterdam, 1966, p. 997.

[17] P.W. Martin, J. W. Bichard and C. Budtz-Jϕrgensen, J. Chem. Phys. **93** (1990) 6092.

[18] S. Connell, K. Bharuth-Ram, H. Appel, J. P. F. Sellschop and M. Stemmet, Hyp. Int. **36** (1987) 185.

[19] D. Wegner, Hyp. Int. **23** (1985) 179.

[20] R. M. Steffen and K. Alder, in *The Electromagnetic Interaction in Nuclear Spectroscopy*, W. D. Hamilton (Ed.), North Holland Publishing Co., Amsterdam, 1975, p. 505.

[21] G. K. Semin, T. T. Babuskina and G. G. Yakobson, *Nuclear Quadrupole Resonance in Chemistry*, John Wiley and Sons, New York, 1975.

[22] Neil W. Ashroft and N. David Mermin, *Solid State Physics*, Sounders College, Philadelphia, 1976.

[23] Attila Szabo and Neil S. Ostlund, *Modern Quantum Chemistry*, McGraw Hill Publishing Co., New York, 1989.

[24] C. Pisani, R. Dovesi and C. Roeti, *Hartree-Fock Ab Initio Treatment of Crystalline System*, Springer-Verlag, Berlin, 1988.

[25] Warren J. Hehre, Leo Radon, Paul N. R. Schleyer, John and A. Pople, *Ab Initio Molecular Orbital Theory*, John Willey and Sons, New York, 1986.

[26] S. Huzinaga (ed.), *Gaussian Basis Sets for Molecular Calculations*, Elsevier, Amsterdam, 1984.

[27] S. Huzinaga, *Hand Book of Gaussian Basis Set*, Elsevier, Amsterdam, 1985.

[28] M. J. Frisch, G. W. Trucks, M. Head-Gordon, P. M. W. Gill, M. W. Wong, J. B. Foresman, B. G. Johnson, H. B. Schlegel, M. A. Robb, E. S. Replogle, R. Gomperts, J. L. Andres, K. Raghavachari, J. S. Binkley, C. Gonzales, R. L. Martin, D. J. Fox, D. J. Defrees, J. Baker, J. J. P. Stewart and J. A. Pople, *Gaussian 92, Revision C* (Gaussian Inc., Pittsburgh, PA, 1992).

[29] Robert G. Parr and Weitao Yang, *Density Functional Theories of Atoms and Molecules*, Oxford University Press, New York, 1986.

[30] R. M. Dreizler and E. K. U. Gross, *Density Functional Theory*, Springer-Verlag, Berlin, 1990.

[31] Peter Fulde, *Electron Correlations in Molecules and Solids*, Springer-Verlag, Berlin, 1991.

[32] Axel D. Becke, J. Chem. Phys., **96** (1992) 2155.

[33] Axel D. Becke, J. Chem. Phys., **97** (1992) 9173.

[34] Axel D. Becke, J. Chem. Phys., **98** (1993) 1372.

[35] Axel D. Becke, J. Chem. Phys., **98** (1993) 5648.

[36] H. Postma and N. J. Stone in *Low Temperature Nuclear Orientation*, N. J. Stone and H. Postma (Eds.), North Holland Publishing Co., Amsterdam, 1986, p. 1.

[37] S. R. DeGroot, H. A. Toelhoek and W. J. Huiskamp, in *Alpha-, Beta- and Gamma-ray Spectroscopy*, Vol. 2, K. Siegbahn (Ed.), North Holland Publishing Co., Amsterdam, 1966, p. 1199.

[38] B. Castel and I. S. Towner, *Modern Theories of Nuclear Moments*, Clarendon Press, Oxford University Press, London, 1990.

[39] D. R. Hamilton, Phys. Rev., **58** (1940) 122.

[40] K. C. Mishra, K.J. Duff and T.P. Das, Phys. Rev. **B25** (1982) 3389.

[41] J. W. Bichard, personal communication.

[42] F. K. McGowan and P. H. Stelson in *Nuclear Spectroscopy and Reactions*, part C, ed. Joseph Cerny, Academic Press, New York and London, 1974.

[43] A. Crametz, personal communication.

[44] A. Crametz, Nucl. Int. meth. **A242** (1986) 179.

[45] H. E. Johns and J. R. Cunningham, *The Physics of Radiology*, Fourth Ed., Charles C. Thomas Publissher, Springfield, Illinois, 1983.

[46] E. Segre, *Nuclei and Particles*, Second ed., The Benjamin/Cummings Publishing Co., 1977.

[47] J. F. Ziegler (ed), *Ion Implantation Science and Technology*, Academic Press, Orlando, 1984.

[48] H. H. Andersen and J. F. Ziegler. *Hydrogen stopping powers and ranges in all elements*, Pergamon Press, New York, 1977.

[49] J. F. Ziegler, *Helium : stopping powers and ranges in all elemental matter*, Pergamon Press, New York, 1977.

[50] D. Dantreppe in *Hyperfine Interactions in Excited Nuclei*, Gvirol Goldring and Rafael Kalish (Eds.) Vol 1, Gordon and Breach Science Publishers, New York, 1971, p3.

[51] R. L. Kleinhenz, Y. H. Lee, Vijay A. Singh, P. M. Mooney, A. Jaworowski, L. M . Roth, J. C. Correli and J. W. Corbett, in *Defects and Radiation Effects in Semiconductors*, J. H. Albany (Ed.), Institute of Physics, Brisbol, 1978, p. 200.

[52] P. Barker and D. W. Palmer in *Defects and Radiation Effects in Semiconductors*, J. H. Albany (Ed.), Institute of Physics, Brisbol, 1978, p. 230.

[53] James W. Mayer, Lennart Eriksson and John A. Davies, *Ion implantation in semiconductors, silicon and germanium*, Academic Press, New York, 1970.

[54] G. Carter and W. A. Grant, *Ion implantation of semiconductors*, Wiley and Sons, 1976.

[55] David K. Brice, *Ion implantation range and energy deposition distributions*, Plenum Press, 1975.

[56] W. Kreische, H. -U. Maar, H. Neidrig, K. Reuter and K. Roth, Hyp. Int. **4** (1978) 732.

[57] S. T. Picraux and F. L. Vook, Phys. Rev. **B18** (1977) 3851.

[58] B. T. Kelly, *Physics of Graphite*, Applied Science Publications, London, 1981.

[59] B. Kastelein, Ph. D. Thesis, Technical University of Delf, The Netherlands (1992).

[60] A. W. Sunyar and P. Thieberger, Phys. Rev. **151** (1966) 910.

[61] M. Carchidi and B. H. Wildenthal, Phys. Rev. **C37** (1988) 1681.

[62] J. Booten, private communication.

[63] B. H. Wildenthal, Prog. Part. Nucl. Phys. **11** (1986) 5.

[64] E. C. Halbert, J. B. McGrory, B. H. Wildenthal and S. P. Pandya, in *Advances in Nuclear Physics*, Vol. 4, M. Baranger and E. Vogt (Eds.), Plenum Press, New York, 1971, p. 316.

[65] B. Kastelein, M. E. J. Prins, J. Andriessen, H. Postma and L. Klostermann, Phys. Rev. **B46** (1992) 8818.

[66] C. Lee, W. Yang and R.G. Parr, Phys. Rev. **B37**, (1988) 785.

[67] K. Bharuth-Ram, S. Connell, J. P. F. Sellschop, M. Stemmet and H. Appel, Radiation Effects and Defects in Solids **108** (1989) 73.

[68] K. Bonde Nielsen, B. Toft, K. C. Mishra, Santos K. Mishra, K. J. Duff and T. P. Das, J. Am. Chem. Soc. **105** (1983) 1734.

[69] N. Bartlett, B. Mc Guillan and A. S. Robinson, Mater. Res. Bull. **13** (1978) 1259.

[70] S. Connell, K. Bharuth-Ram, K., J. P. F. Sellschop, M.C. Stemmet and H. Appel, Hyp.Int. **39** (1988) 397.

[71] Th. Wichert, M. Deicher, G. Grübel, R.Keller, N. Schulz and H. Skudlik, Appl. Phys. **A 48** (1989) 59.

[72] E. K. Warburton, A. R. Poletti and J. W. Olness, Phys. Rev. **16** (1967) 168.

[73] A. Kabir and B. Buck, Nucl. Phys. **A 556** (1993) 1.

[74] P. Raghavan, At. Data Nucl. Data Tables **42** (1989) 189.

[75] W. J. Vermeer, Phys. Lett. **B 234** (1990) 219.

[76] G. P. Carver, Phys. Rev. **B 2** (1970) 2284.

[77] L. E. Campbell, G. L. Montet and G. J. Perlow, Phys. Rev. **B15** (1976) 3318.

[78] F. D. Feiock and W. R. Johnson, Phys. Rev. **187** (1969) 39.

[79] B. Kastelein, H. Postma and J. Andriessen, Hyp. Int. **75** (1992) 315.

[80] Y. Byoung-gon, N. Konuma and E. Arai, J. App. Phys. **70** (1991) 2408.

[81] Y. Nishioka, K. Ohyu, Y. Ohji, N. Natsuaki, K. Mukai and T. P. Ma, IEEE Electron Device Lett. **EDL–10** (1989) 141.

[82] P.J. Wright and K.C. Saraswat, IEEE Trans. Electron Devices **ED–36** (1989) 879.

[83] Y. Nishioka, K. Ohyu, Y. Ohji, N. Natsuaki and T. P. Ma, J. Appl. Phys. **66** (1989) 3909.

[84] P. J. Wright, N. Kasai, S. Inoue and K.C. Saraswat, IEEE Electron Device Lett. **EDL–10** (1989) 347.

[85] Y. Nishioka, K. Ohyu, Y. Ohji., M. Kato, E.F. da Silva, Jr. and T. P. Ma, IEEE Trans. Nucl. Sci. **NS–36** (1989) 2116.

[86] K. P. MacWilliams, L.F. Halle and T.C. Zietlow, IEEE Electron Device Lett. **EDL–11** (1990) 3.

[87] K. Ohyu, T. Itoga, Y. Nishioka and N. Natsuaki, Jpn. J. Appl. Phys **28** (1989) 1041.

[88] B. Yu, N. Konuma and E. Arai, J. App. Phys. **70** (1991) 2408.

[89] K. Bonde Nielsen, H.K. Schou, T. Lauritsen, G. Weyer, I. Stensgaard, J.W. Petersen and S. Damgaard, J. Phys. C. **17** (1984) 3519.

[90] S. B. Sulaiman, N. Sahoo, K. C. Mishra, T. P. Das and K. Bonde Nielsen, Proc. VIII*th*. Int. Conf. on Hyperfine Interactions, Prague 1989, eds. M. Finger, B. Sediak and K. Zaweta, published in Hyp. Int. **60** (1990) 861.

[91] J. Sauer, Chem. Rev. **89** (1989) 199.

[92] J. B. Collins, P. von R. Schleyer, J. S. Binkley and J. A. Pople, J. Chem. Phys. **64** (1976) 5142.

[93] E. S. Kryachko and E.V. Ludeña, *Density Functional Theory of Many-Electron Systems*, Kluwer, 1989.

[94] S. T. Picraux and F.L. Vook, Phys. Rev. **B18** (1978) 2066.

[95] V. A. Singh, C. Weigel, J. W. Corbett and L. M. Roth, Phys. Status Solidi **81** (1977) 637.

[96] W. S. Verwoerd, Nucl. Instrum. Methods **B35** (1988) 509.

[97] G. D. Watkins, Phys. Rev. **B12** (1975) 5824.

[98] K. L. Brower, Phys. Rev. **B9** (1974) 2607.

[99] G. D. Watkins, IEEE Trans. **NS–16** (1969) 13.

[100] Proceedings of Symposium F of the European Materials Research Society, Nuclear Methods in Semiconductor Physics, Strasbourg, May 1991, published in Nucl. Instrum. Methods **B63** (1992) 1.

[101] K. Bonde Nielsen, T. Lauritsen, G. Weyer, H. K. Schou and P. T. Nielsen, 6th Int. Conf. on Hyperfine Interactions (Groningen) 1983, published in Hyp. Int. **15/16** (1983) 491.

[102] N. Sahoo, S. B. Sulaiman, K. C. Mishra and T. P. Das, Phys. Rev. **B 39** (1989) 13389.

[103] W. S. Verwoerd, Nucl. Instrum. Methods **B35** (1988) 509.

[104] V. A. Singh, C. Weigel, J. W. Corbett and L. M. Roth, Phys. Status Solidi **81** (1977) 637.